JOINT EUROPEAN TORUS JET

JET–P(95)60

Many Authors

JET Papers presented to the 16th Symposium on Fusion Engineering (SOFE) (2-5 October 1995, Champaign, Illinois, USA)

JET Papers presented to the 16th Symposium on Fusion Engineering (SOFE) (2-5 October 1995, Champaign, Illinois, USA)

Many Authors

JET-Joint Undertaking, Culham Science Centre, OX14 3EA, Abingdon, UK

Preprint of a Paper to be submitted for publication in the proceedings of the
16th Symposium on Fusion Engineering
(2-5 October 1995, Champaign, Illinois, USA)

October 1995

JET Papers Presented at the 16th Symposium on Fusion Engineering (Champaign, USA, 2-5 October 1995)

Contents

JET WITH A PUMPED DIVERTOR TECHNICAL ISSUES AND MAIN RESULTS

The JET Team (presented by E. Bertolini)
JET Joint Undertaking, Abingdon, Oxon OX14 3EA, UK

ABSTRACT

The most recent modification to JET has been the installation of a single-null pumped divertor, for active control of plasma impurities. This is to address central physics issues relevant to the design of a 'next step' tokamak. Experiments conducted during the 1994-95 campaign, with plasma currents up to 6MA, have shown that the *Mark I* divertor, which makes use of strike point sweeping across the target plates, is a suitable tool to control the influx of impurities in the plasma core. The operation of a tokamak with a pumped divertor has been characterised in detail. However the divertor configuration must be optimised to better meet ITER requirements. Therefore an improved (more closed) divertor structure, which may not require sweeping, is under assembly at present (*Mark II*). It is designed, in addition, to allow divertor tile structures to be fully replaceable by remote handling techniques, following D-T fusion experiments. New types of events involving electromechanical interactions of plasma with the vessel and in-vessel structural components have been encountered, due to plasma vertical instabilities and disruptions (such as toroidal asymmetries of vacuum vessel forces and side-ways vessel displacements). The physics and engineering experimental work performed in JET is primarily dedicated to the finalisation of the ITER design.

I. INTRODUCTION

The Joint European Torus (JET) has operated since June 1983. The inherent flexibility of the machine original concept [1] has permitted a great variety of plasma and fusion physics issues to be addressed. This has been possible due to engineering modifications and upgradings to improve plasma configurations and machine performance. These changes have followed the evolution in physics understanding and priorities towards the definition of parameters required in a fusion reactor, without major alteration to the basic machine structure [2].

Operation with a wide range of plasma currents and additional heating powers has confirmed the nearly linear scaling of energy confinement time with plasma current and its degradation with input power. Moreover, the H-mode regime was established at plasma currents up to 3MA in a X-point magnetic configuration. This showed a doubling of the energy confinement time compared with the L-mode, and confirmed earlier findings obtained with smaller tokamaks, ASDEX in Europe and PBX in the USA. These JET results, obtained with reactor relevant plasma parameters, led to a major upgrading of JET's electromagnetic system, to increase the plasma current capability from 4.8 to 7MA in limiter configuration and to make X-point magnetic configurations possible in excess of 5MA.

It was clear, however that impurities were playing a key role in hampering further progress in plasma performance. Therefore, a second major upgrading was implemented. This consisted in progressively covering the Inconel vacuum vessel walls with low-Z materials, with graphite tiles and frequent wall carbonisation at first, and with beryllium tiles and Be evaporation later. Dilution factors (deuteron density/electron density, n_D/n_e) exceeding 90% and Z_{eff} less than 2 were achieved. As a consequence of all these improvements a fusion triple product $(n_D\tau_E T_i)$ above 0.9×10^{21}m^{-3} keV s and a D-T equivalent Q_{DT} exceeding unity were achieved.

These parameters were considered suitable to perform the first ever controlled thermonuclear fusion experiment towards the end of 1991. This led to the production of 1.7MW of fusion power using a mixture of D(89%)-T(11%).

All the basic JET features, including D-shaped toroidal coils, vacuum vessel and plasma, single null magnetic configuration, high plasma current and beryllium as a primary choice for first wall material are incorporated in the present ITER design [3].

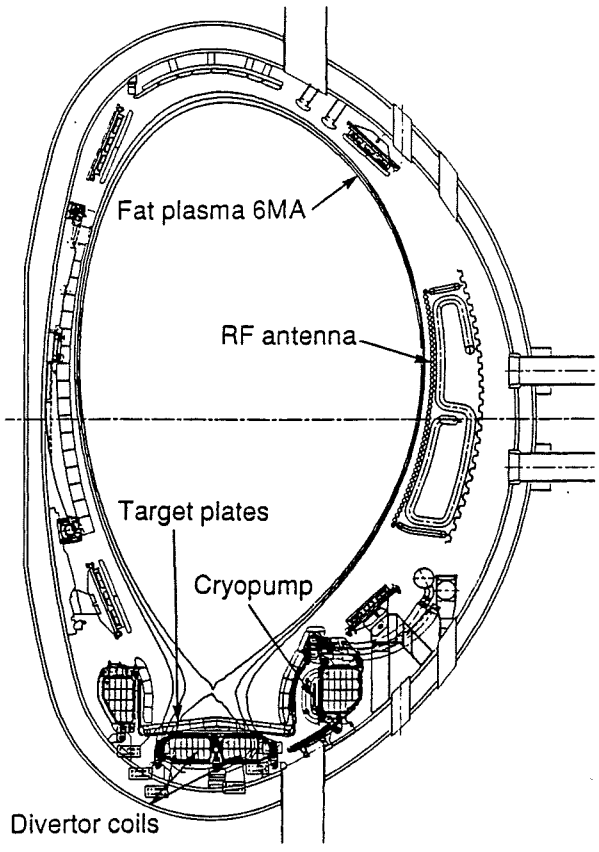

Fig 1: Design features of the Mark I divertor first wall structure, showing poloidal coils, target plates, cryopump and RF antennae

II. The Divertor Programme

The success in achieving short-lived high plasma performance in the 1991-92 experimental campaign, clearly indicated that a passive control of the impurities was not sufficient. Performance decayed abruptly after 1-2 seconds (*carbon bloom*), due to a combination of MHD instabilities and excessive production of impurities in the X-point region, which would be ionised and trapped in the plasma (**Fig.1**).

Active control of particle and power exhaust is required in JET and even more so in a fusion reactor, where long burn is a key requirement. This critical issue has been addressed in JET by installing a pumped divertor (*Mark I*) at the bottom of the vacuum vessel during the 1992-93 shutdown [**4**,**5**,**6**,**7**].

A. The pumped divertor

Main components of the Mark I divertor are:

- *Four Freon cooled copper poloidal coils*, which create an X-point magnetic configuration at sufficient height to allow installation of divertor components and control of the magnetic flux expansion in the divertor chamber. The coils allow for strike-point sweeping to reduce the specific power load to the divertor tiles;
- The target plates, which collect the power released by the plasma, consist of an inertially water cooled Inconel structure, which supports accurately shaped CFC tiles to eliminate exposed edges. These tiles have been replaced by beryllium tiles for comparison of performance;
- The toroidal cryo-pump anchored to the outer divertor coil, consists of a water cooled baffle, a liquid nitrogen copper back panel, an array of liquid helium cooled pipes and a chevron structure. Its function is the control the plasma density in the divertor chamber, in particular when cold gas is injected to minimise ionisation of impurities.

B. Further significant machine modifications

B.1.*First Wall* -The installation of the divertor implied a reduced plasma volume and a new plasma shape: therefore a complete re-design of the vacuum vessel first wall was required [**8**]. The eight *ion cyclotron radio frequency (ICRF)* antennae were replaced, to satisfy the plasma proximity requirement for effective RF power coupling; the *lower hybrid current drive (LHCD) launcher* was re-shaped for the same reason. The old toroidal limiters have been removed and replaced by *12 discrete poloidal limiters* on the outer wall for RF antennae and wall protection, and *16 inner wall guard limiters* were also installed. All limiters carry properly shaped graphite tiles. In addition eight *saddle coils*, four at the top and four at the bottom of the vessel were installed, to be used for control of MHD instabilities (m=2, n=1 modes) and for the study of toroidal Alfven eigenmodes, TAE (of concern for alpha particle confinement). The installation of divertor and of new in-vessel components required modification of existing *diagnostics* and the installation of new ones for measurements in the divertor region [**9**]. The new JET's first wall configuration is shown in **Fig.2**.

B.2.*Control and Protection* - Divertor (elongated) plasmas are more vertically unstable and require plasma-wall gap control, thus a new *plasma position and current control* (PPCC) system had to be installed. The system is designed with 'intelligent' software to control plasma-wall gaps and poloidal coil currents [**10**]. Similar technology has been used for the new *coil protection system* (CPS), necessary to cope with the greatly enhanced electromagnetic equatorial asymmetry of the machine. It comprises a wide range of protections in respect to overcurrents, overvoltages, limits to thermal and mechanical stresses, and model-based fault detection [**11**].

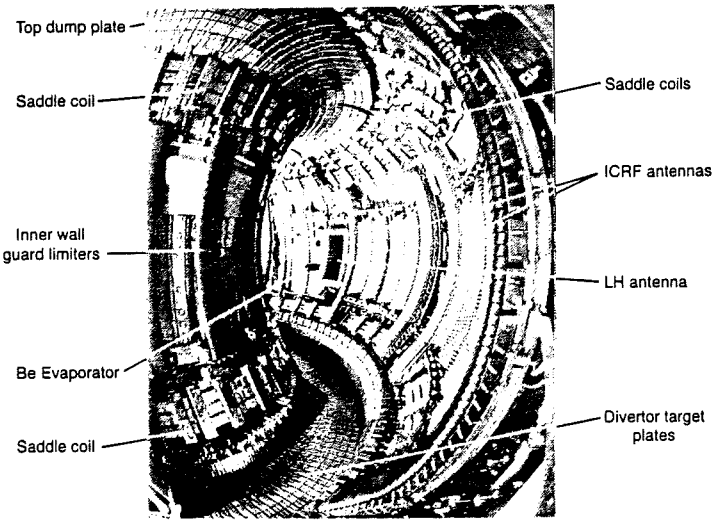

Fig. 2: The new JET first wall configuration, following the installation of Mark I divertor

B.3.*Power Supplies* - Four new 12-pulse thyristor *poloidal divertor field amplifiers (PDFA)*, 500-650V, 40kA d.c. supply the divertor coils with strike-point sweeping capability [**12**] and a new *fast radial field amplifier system (FRFA)*, based on GTO's technologies, 5kV, 5kA (or 10kV, 2.5kA), response time 0.2ms, meets the requirements for plasma vertical position control [**13**]. A system of four 1.5kV, 3kA *disruption feedback amplifiers (DFAS)* supply the saddle coils [**14**]. These power supplies, like most of those already existing at JET, are supplied directly by the 400kV grid. Thus, an additional 50MVAR of *reactive power compensation* was required to limit excessive AC voltage drops at 400kV and 33kV busbars.

The cross-section of JET with the pumped divertor poloidal coils is shown in **Fig 3**, whilst **Table I** compares the evolution of the main JET machine parameters. An important penalty (~20%) in plasma volume, adversely affecting performance, had to be paid to install the divertor within the existing machine structure.

III. Operation with the Mark I Divertor

Extended commissioning, first without and then with plasma, was necessary to become familiar with the 'new' JET, before the start of the experimental programme in May 1994.

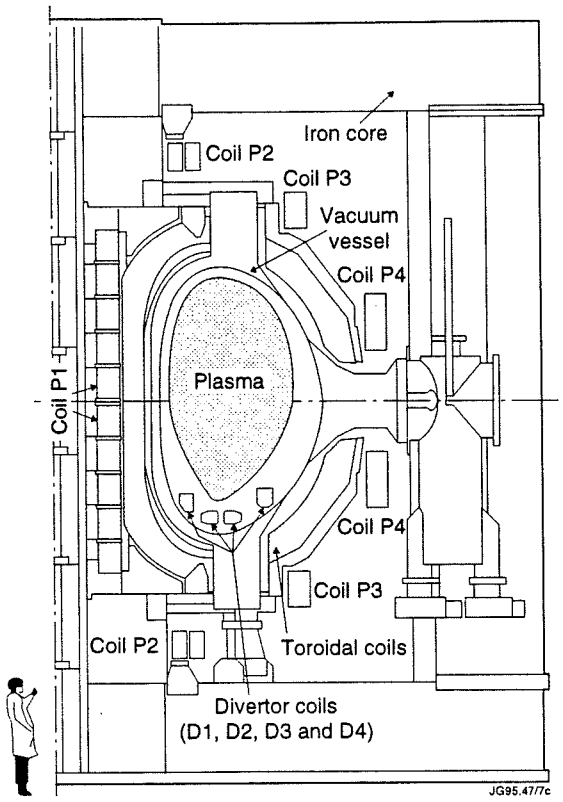

Fig 3: JET cross-section. showing the new divertor magnetic configuration

Table I
Evolution of principal JET parameters with JET upgrading and with divertor

Parameter	Original 1983	Upgraded 1987	Divertor 1994
Plasma minor radius, a (m)	1.25	1.25	0.95
Plasma half height, b (m)	2.10	2.15	1.75
Plasma major radius, geometrical centre RO (m)	2.96	2.96	2.85
Plasma volume (m3)	150(a) –	130(a) 105(b)	– 85(b)
Plasma aspect ratio, RO/a	2.37	2.37	3.0
Plasma elongation, b/a	1.68	1.9	1.85
Toroidal magnetic field (at RO), BTO(T)	3.45	3.45	3.6
Flat top pulse length t (s)	10(a)	10(a)	10(a)
Plasma current, IP(MA)	4.8	7.0(b) 5.0(c)	6.0
Transform flux, f (Wb)	34	42	42
Neutral beam power, (MW)	15	20	22
Ion cyclotron power, (MW)	15	20	2
Lower hybrid power, (MW)	–	5	10

(a) Longer at reduced plasma current
(b) Limiter
(c) X-point

The most important result obtained was the demonstration that the pumped divertor operated successfully. In fact, in the X-point configuration (without divertor) an input of only 15MJ of injected energy would lead to a 'carbon bloom', with sudden termination of the high performance phase. With the divertor instead, up to >180MJ (from 32 MW of combined NB and RF heating) were injected without sign of discharge deterioration. The care taken in the design and in the installation CFC divertor tiles (which eliminated sharp edges), the successful use of the cryopump and X-point sweeping (a suitable technique to reduce target temperature from about 1000°C to 600°C or less) have been instrumental in achieving longer, cleaner and more stationary H-modes. As a result *plasma performance* could be maintained for *long pulses* (~20s, ~40τ_E) with Z_{eff}~*1* (**Fig. 4**).

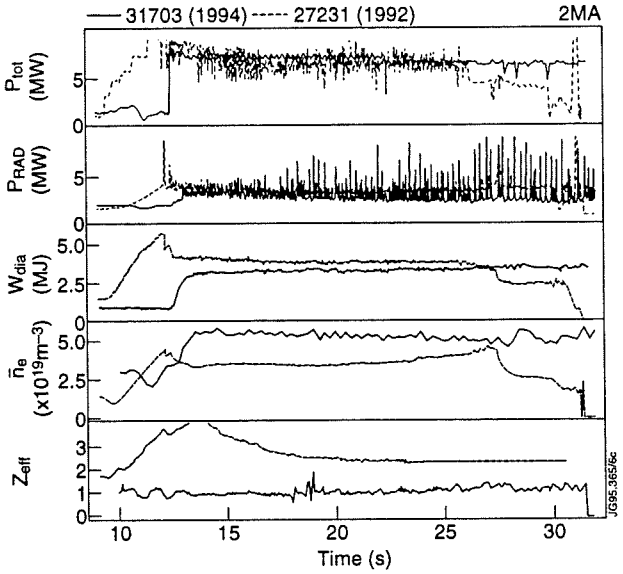

Fig 4: Comparison of similar discharges with pumped divertor (1994) and without divertor (1992), showing significant reduction in Z_{eff}

Electron temperatures of T_e~*15keV* were obtained with both combined heating and RF only. Full *current drive up to 3MA* was demonstrated with 7MW of LHCD power.

Although the plasma volume had to be reduced by about 20%, the best global performance almost identical to that without divertor was achieved. JET record value of the reaction parameter, R_{DD}=*9.4x10^{16} reactions/s*, was obtained. Moreover reliable divertor operation up to plasma currents of 5 and 6MA was established with record plasma stored energy of ~13MJ with 18MW of NB injected power and with combined RF-NB heating (**Fig.5**).

Initially, *ELM-free H-modes* were difficult to establish and to be maintained for several seconds. It should be emphasised, of course, that a reactor (ITER) needs to operate with ELM's to prevent accumulation of impurities (alpha-particles) in the plasma core. The

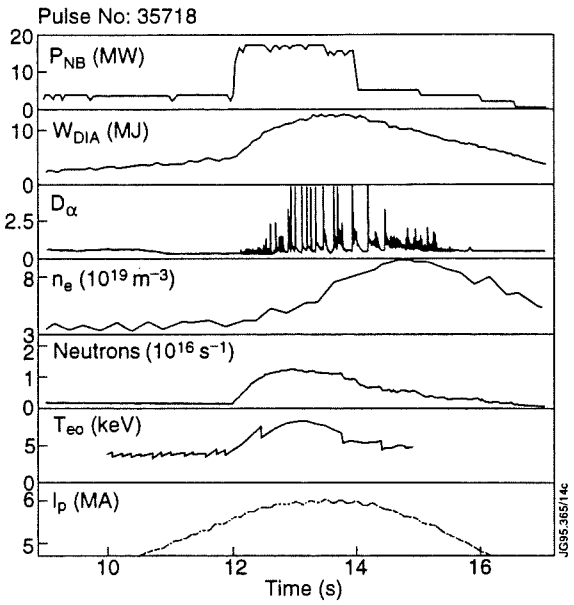

Fig 5: ELMy H-mode discharge with plasma current of 6MA, 18MW of NB power, showing 13MJ of stored energy

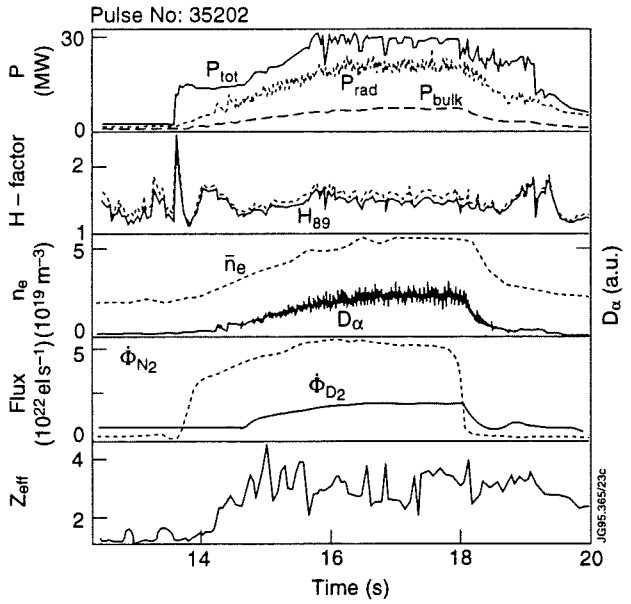

Fig 6: Typical pattern of radiative divertor experiments, with 32MW of combined heating and N_2 seeding, leading to 75% of power exhausted by radiation

appearance of *giant-ELM's* has often led to premature termination of the discharge [**16**]. These are issues deserving further studies, in the future.

A key issue for a reactor divertor is to limit the direct deposition of power on the target plates. This can be achieved by enhancing the *energy spread by radiation* on a larger surface. Preliminary JET experiments conducted by injecting a mixture of deuterium with neon or nitrogen, have shown that radiation may account for up to ~80% of the energy released by the plasma, albeit with some reduction in confinement (**Fig 6**). This subject will be specifically addressed at a later stage of the JET programme when Mark IIGB (gas box) divertor will be installed.

Two specific experiments, requested by the ITER designers were also performed in JET. The first experiment was to investigate the effect of toroidal field ripple. By re-arranging the d.c. power supplies to the toroidal coils in two independent sets, each supplying 16 of the total of 32 toroidal coils, it has been possible to vary the *toroidal magnetic field ripple* in the ITER-relevant range of 0.1% to 2% at the plasma edge. As predicted, losses of thermal and high energy particles (1MeV tritons and 125keV NB ions) were very small, while losses of intermediate energy particles (larger than 10keV) were somewhat higher than predicted. Therefore, ITER ripple (with 20 TF coils) should not have any effect on alpha-particle heating (and thus on the ITER global performance). The only critical ripple issues may be the load on the first wall due to alpha-particle losses and a reduction in plasma rotation [**17**]. The second experiment dealt with the *comparison between CFC and Beryllium.* Since the primary choice for ITER first wall is still beryllium, the CFC divertor tiles have been replaced with castellated beryllium tiles (to reduce thermal stresses). The most significant CFC plasma scenarios have been repeated and, in global sense, similar physics results have been obtained(**Fig.7**), in establishing and maintaining H-modes and in energy confinement times, while Z_{eff} values were slightly lower with Be tiles (oxygen is further reduced). The energy deposition on the beryllium tiles appears to be mainly toroidally symmetric . Since the melting temperature of beryllium is ~1300°C, it is considered impossible to operate a tokamak (and even more so a reactor like ITER) without some localised Be melting, caused by impulse heat loads and plasma disruptions. Therefore, experiments have been conducted causing intentional surface melting of the beryllium tiles, culminating in a *controlled beryllium melt experiment.* The preliminary conclusion is that beryllium

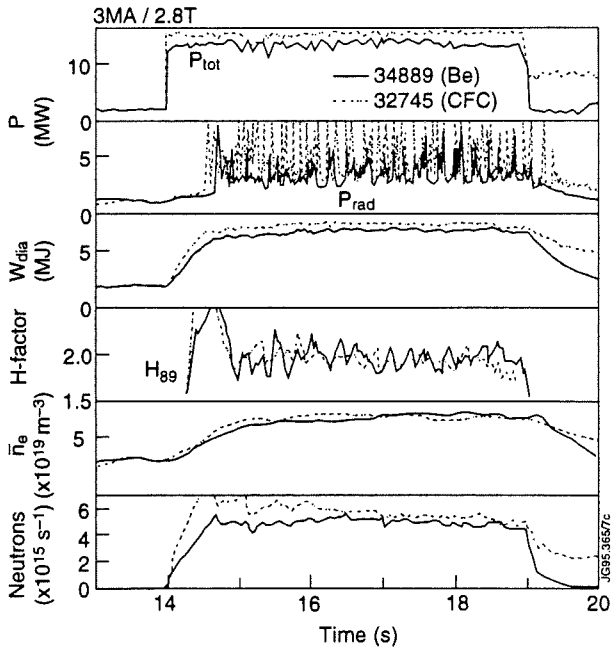

Fig 7: Comparison of two equivalent steady-state H-mode discharges, showing similar behaviour with CFC and Be target tiles

could be used as divertor target plate material for ITER. However, heat fluxes of 25MW/m^2 expected in ITER following disruption events, would not provide a sufficient degree of passive self-protection due to enhanced radiation (vapour shielding). Therefore an active protection device should be considered [**18**]. Many other specific physics issues have been studied in great detail and the results are being progressively published, while the large amount of data collected are still being analysed.

B. Engineering Experience and Prospects

Such a new and extensive experimental campaign has been made possible by the extended commissioning of the 'new' machine and by the reliability of the major machine subsystems. A total of *7389 pulses* were performed, 23% were commissioning (with and without plasma) and 77% were operational pulses. A key role has been played by PPCC system, in successfully handling a great variety of discharge scenarios and by CPS in the effective protection of the machine with its new complexities and new type of faults not experienced before.

B.1. Plasma Position and Current Control (PPCC) System
The flexibility of the new PPCC has greatly simplified JET's operations, since it allowed a fairly accurate control of the plasma boundary. PPCC has proven to have the capability of *controlling the plasma distance* from the outer, inner and top vessel wall, the X-point position and the plasma current simultaneously, and to change control behaviour during the pulse to satisfy the different requirements of the various phases of the pulse. Switching from coil current to gap control does not affect plasma equilibrium (**Fig.8**). As regard *vertical stabilisation*, although the performance is presently limited by the noise introduced in the feedback signals by thyristor switching of the divertor power supplies,

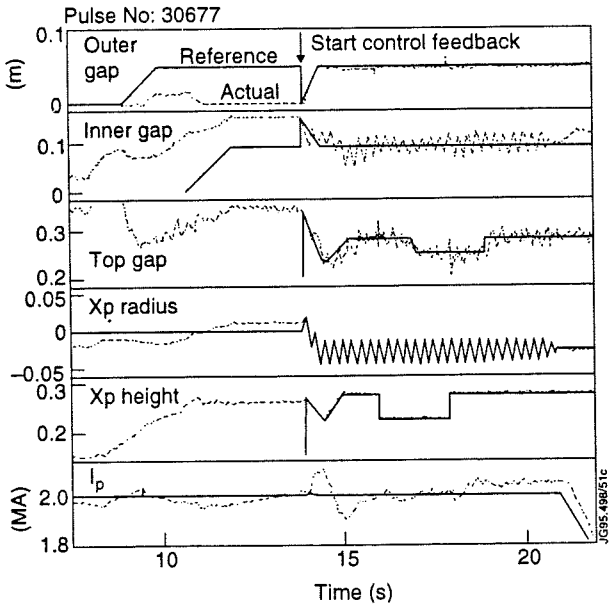

Fig 8: PPCC control of the divertor magnetic configuration with 4Hz X-point sweeping, showing the accuracy of gap controll

the system has demonstrated the ability to cope with plasma with growth rates of $800s^{-1}$. This has allowed the Mark I campaign to be conducted virtually without vertical instabilities not generated by plasma internal events. Improvements are now underway: a tuned power filter will be installed at the PDFA d.c. output leading to ≥32dB attenuation of the 600Hz and 1200Hz ripple noise; the computational power to allow more complex algorithms to be used will be increased, to include Soft X-ray signals for vertical stabilisation purposes; plasma shape control will be upgraded to achieve a more accurate control of the X-point position and the simultaneous control of the two strike-point positions [**19**].

B.2. Coil Protection System (CPS) CPS has extended the JET operating range by allowing the use of dynamic thresholds based upon on-line calculations (e.g. the central P1 coil current threshold which is a function of the toroidal field current). It has introduced a *real-time evaluation of the coil models* that made possible fault detection from un-measured quantities such as short-circuit currents, transducer faults, wrong power supply polarities, etc. A typical example of CPS intervention is given in **Fig.9**. It shows the protective action for excessive P1 average current (the six P1 central coils can carry up to 60kA because of the pre-compression of the toroidal field coils, while the outer coils can carry 40kA only). The algorithm has been optimised to minimise the overshoot of the current in the P1 end coils. TF coil protection includes transverse force protection (due to the tokamak torque), the coil interturn fault detection and the earth leakage protection. CPS has operated with a high degree of reliability [**20**]. CPS will now be progressively upgraded to a *Torus Protection System (TPS)* to include monitoring and analysis of stresses in the vacuum vessel.

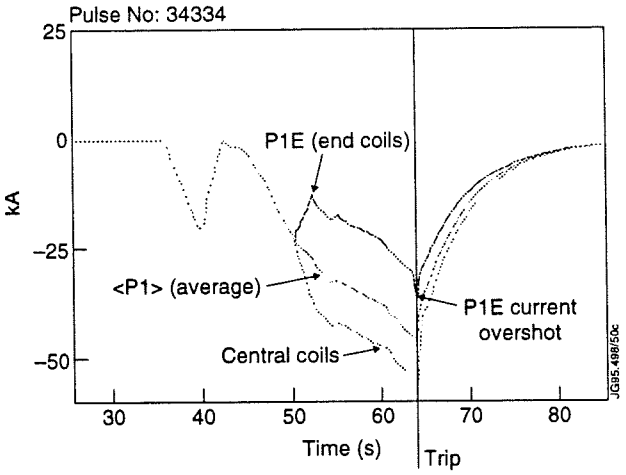

Fig 9 A typical example of CPF protective action against excessive current in the central solenoid end coils (PIE)

C. Plasma-Machine Interactions

The JET vacuum vessel consists of eight double wall octants, each made up of four bellows and five rigid sectors. Each octant carries a main horizontal port and two (top and bottom) main vertical ports for access.

The vessel has two inboard in-vessel and two outer out-vessel reinforcing rings. In vessel components are welded on the inner wall. The vessel support system allows for thermal expansion (the vessel operates at 250-320°C) and contains vessel movements in plasma operation. Plasma displacements and disruptions, in fact, cause impulse vertical and horizontal forces to be applied to the vacuum vessel, in-vessel components and divertor coils, leading to vessel movements and stresses. The plasma displacements *induce currents* in the structural components and *halo currents* flowing from the plasma to the structural components. The forces are generated by the interaction of these currents with the magnetic field.

Two types of vessel movements were considered in the design of the vessel and of supports: rolling and rocking motion, due to the fact that the centroid of the vertical forces applied on each octant is not in line with the reaction forces at the main vertical port restraints, causing a twisting moment around the toroidal axis, and a net inward motion caused by the toroidal current induced by plasma disappearance and by the poloidal current induced by the change in the diamagnetic flux. We became aware of new phenomena during the 1994-95 divertor experimental campaign, namely, vertical *forces* on the vessel are *not toroidally symmetric*, causing overloading and additional shear stresses and *vessel side-ways motion*, caused by non symmetric horizontal forces applied to the vacuum vessel. While the basic structure of the first wall did cope extremely well with these forces and stresses, some auxiliary in-vessel components were damaged (saddle coils, beryllium evaporator head, glow discharge cleaning electrode, reciprocating probe, earthing straps and tile support rail for ICRH antenna), because when they were first designed, the consequences of these phenomena were not yet fully appreciated by tokamak designers [**21**].

While appropriate design modification have made the 'weak' components suitable for JET operation, these phenomena are not fully understood and JET is dedicating a special engineering-physics effort in this area. This implies theoretical work, analysis of data, implementation of new measurements. It is clear however that stresses in the vessel and in other structural components depend now not only on the magnetic field and the plasma current (as assumed by tokamak designers in the past) but also on plasma configuration and disruption scenario. There is no doubt that the finalisation of ITER design would benefit from progress in this work.

IV. Future Development

The JET Council has recently supported the extension of the JET Programme up to the end of 1999 and the Project is proceeding accordingly, while the extension of the JET Joint Undertaking is now being considered by the Council of Ministers of the European Union. Highlights of the extended JET Programme are divertor studies using divertor configurations as close as possible to reactor requirements and fusion experiments with D(50%)-T(50%) mixtures, DTE1 in 1996-97 and DTE2 in 1999 (**Table II**).

A. Divertor Development

It is important to validate the divertor modelling by comparing the most encouraging results obtained with Mark I with the performance of Mark II divertor, which provides a much closer configuration, enhancing neutral particle and impurity retention in the divertor chamber (**Fig.10**). *Mark II* divertor is being installed during the present shutdown (June 1995-March 1996).

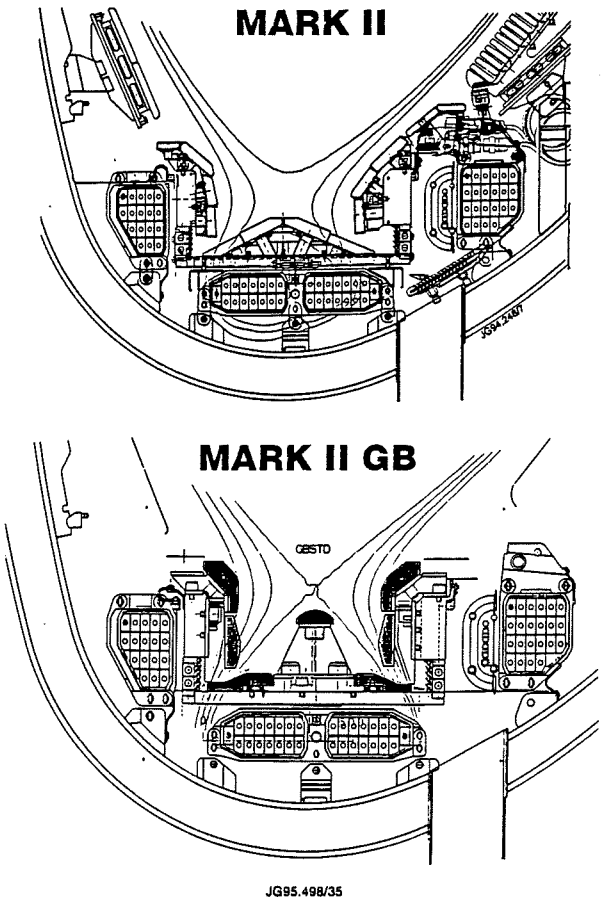

Fig 10: Cross-sections of the Mark II divertor now being installed, and of the future Mark II GB divertor

The support structure consists of a *continuous toroidal tray* (assembled in radial sectors) on top of which the target plates are installed and can be subsequently replaced by different divertor configurations, such as *Mark IIGB*, a configuration closer to ITER needs while maintaining the divertor coils and the toroidal tray in position.

B. Deuterium-Tritium Experiments

Following the preliminary Tritium Experiment in 1991, it was decided to further develop the machine to a more reactor-like configuration by the installation of a pumped divertor, prior to further D-T experiments.

Two periods of D-T operation are currently foreseen: a limited period (DTE1) to start towards the end of 1996 (four months) and a more extended period (DTE2) in 1999, after completion of divertor studies with the Mark IIGB (eight months).

As a result of JET's long pulse capability and its control of impurities, a key objective of *DTE1* would be the production of $\geq 10MW$ of fusion power for several seconds, so that a-particle heating could play a role in the plasma power balance. In addition, a crucial objective would be the study of isotopic effects on confinement scaling and H-mode threshold power. Operation in ELMy-H-mode detached radiative divertor plasmas would also provide valuable information for ITER divertor design. It is expected to carry out the planned programme with a total neutron production of $2x10^{20}$ *neutrons*. DTE2 will have similar physics objectives and it is expected that through the experience gained DTE1 and after a period of plasma optimisation using techniques such as profile control, the fusion performance and the effects of a-particle heating of the plasma would be more significant. A total budget of $5x10^{21}$ *neutrons* is foreseen for *DTE2*.

In performing such an extended D-T operation, full use will be made of the *Active Gas Handling System (AGHS)*, a gas re-processing plant to collect the gases from the torus, neutral beam system, pellet injection and diagnostics, to purify and isotopically separate these gas mixtures and to re-inject pure tritium and deuterium into the torus [**22**]. Therefore, the JET D-T experiments would also provide useful engineering experience on the technology of tritium handling for a tokamak reactor.

C. Remote Handling

Although the neutron budget for DTE1 represents a small fraction of the total neutron fluence foreseen in the life of JET, 12 to 18 months of cool-down would be required to allow a manned in-vessel intervention. Therefore, besides its physics characteristics, the Mark II divertor has an important and novel feature: it has been designed to allow replacement of the divertor target structure by full remote handling techniques. The tile carriers will be handled and positioned by the Mascot IV servomanipulator mounted on the articulated boom transporter, through octant No. 5 port. Navigation and pre-positioning will be carried out automatically using *teach-and-repeat techniques* . A shorter version of the articulated boom (Tile Handling Transfer Facility, THTF) will be used for transfer of the tile carriers between the Torus Hall and the vessel, through octant No. 1 main horizontal port. All R.H. tools exist and have been used in the past, but the THTF, which is now under manufacture. To validate the actual capability of the remote handling approach envisaged, part of the Mark II divertor target plates will be installed by remote handling. A mock-up test bed has been prepared, which makes use of the spare machine octant. Shutdown time for replacing Mark II with Mark IIGB divertor is of the utmost importance to limit machine down-time. Therefore, preparation for remote installation of the Mark II tile carriers have included *1000 hours trial* with the Mascot IV, Articulated Boom, Viewing Cameras and associated control systems performing a typical tile exchange for 24hrs/day, for five days per week. The availability of the boom was 97% and that of Mascot was 99%. Moreover two months of mock-up trials were performed to establish the precise techniques to be used and to create the 'teach-and repeat' files [**23**]. These results give a high degree of confidence on thetime-scale eventually foreseen for the Mark II to Mark IIGB target plate exchange with an active machine following DTE1 (**Fig.11**).

It will be the first time that such a complex remote handling operation has been performed on an active machine, providing most valuable engineering experience for the finalization of ITER design.

Table II
JET Programme to the end of 1999

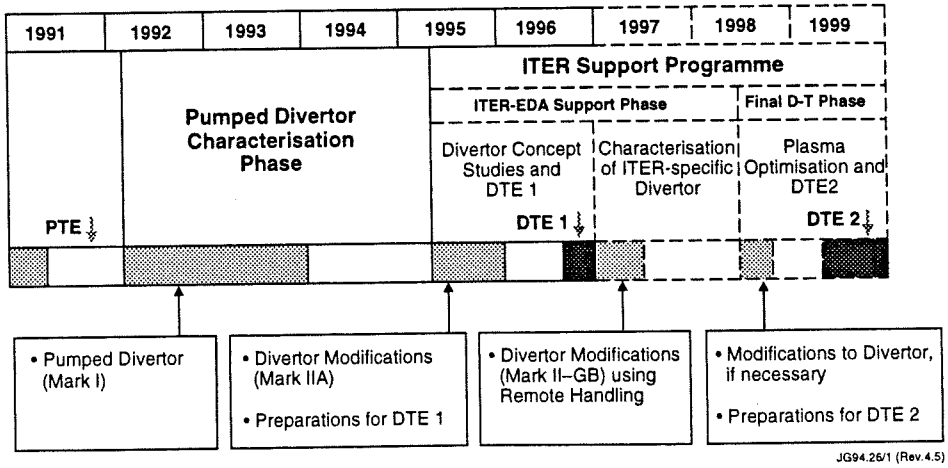

PTE: Preliminary Tritium Experiment
DTE 1: D-T Experiments with 2×10^{20} neutrons
DTE 2: D-T Experiments with 5×10^{21} neutrons

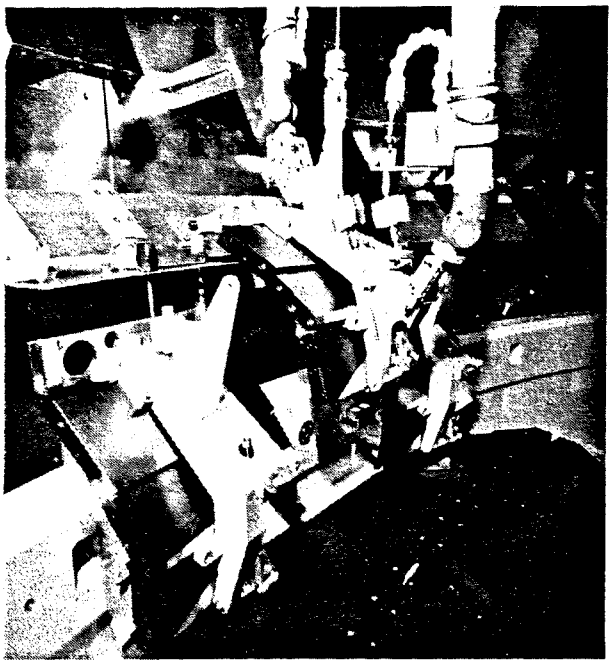

Fig 11: Installation of Mark II divertor side target plates in the JET in-vessel mock-up, using remote handling techniques

D. Machine Enhancements

D-T global fusion performance (fusion triple product $n_D t_E T_i$ an energy gain Q) would benefit tremendously by certain engineering enhancements of the JET machine. Consideration is now being given to the possibility of increasing the toroidal magnetic field from 3.45T to *4.0T for ~10s* flat top, and by an increase of *4 to 6MW* in the injected neutral beam power.
A preliminary assessment of the electromechanical capability of the JET coils and of the mechanical structure indicate that, for the scenarios considered at 6MA plasma current, forces and stresses are still acceptable (shear stress in the central solenoid P1 electrical insulation ≤20MPa and well within the capability of the TF coils and of the mechanical structure). The design for upgrading the current capability of the TF power supplies from 67kA to ~80kA is underway.
The design to upgrade each one of the 16 NB injectors from 80kV, 60A to 120-140kV, 60A is being performed. What is needed is to procure 16, 40-60kV, 60A power supplies to top-up the present ones. These new power supplies are based on thyristor AC/DC rectifier followed by an IGBT high frequency inverter, for limiting the DC output voltage ripple and for NB injector protection. No major modification to the present injectors would be required.

V. Conclusions

The following points summarise the main conclusions that can be drawn:
• Twelve years of JET operation have been essential to define the *plasma volumes* and *plasma currents* required for the design of a reactor-like tokamak;
• The inherent flexibility of the JET design has allowed substantial modifications and *engineering upgradings* of the machine, including an axisymmetric pumped divertor, with the capability to modify its configuration;
• With the *Mark I divertor*, the key problems of power and particle exhaust have been successfully addressed;
• *High fusion performance* has been demonstrated in JET with a divertor, in spite of a 20% reduction of the plasma volume to accommodate the divertor structure;
• The foundations have been laid for further divertor studies with a *Mark II* version and for D-T operation;
• The technologies for *remote handling* of the divertor target replacement under active conditions and for handling tritium have been demonstrated;
• Progress has been made in the analysis and in the understanding of the effect of plasma *vertical instabilities and disruptions* on machine structural components. This allows appropriate measures to be taken for in-vessel component design modification and for more effective machine protection;
• Design work is underway for *enhancing the machine capability* to allow further enhancement of plasma global performance;
• Most of the physics and engineering experience gained during the 1994-95 experimental campaign is relevant to the *finalisation of ITER design.*

Acknowledgements

The content of this paper is the result of extended discussions with many members of the JET Team. The author wishes to acknowledge in particular the contributions of R. Claesen, L. Galbiati, R. Giannella, J. Jacquinot, B. Keen, J. Last, F. Milani, P. Noll, T. Raimondi, G. Sannazzaro and L. Scibile.

References

[1] "The JET Project Design Proposal", Report of the Commission of the European Communities, EUR-5516-e, 1976.

[2] E. Bertolini and the JET Team. "The JET Project: progress towards a Tokamak thermonuclear reactor" Power Engineering Journal June 1993, Vol.7 No.3, p.105.

[3] E. Bertolini and the JET Team, "Impact of JET experimental results and engineering development on the definition of ITER design concept" *Fusion Engineering and Design* 27 (1995), p.27.

[4] M. Keilhacker and the JET Team, "Recent JET results and consequences for future devices", *Proc. 14th International Conference on Plasma Physics and Controlled Thermonuclear Fusion Research*, Würzburg 1992, JET-R(92)84, p.15.

[5] P.H. Rebut, D. Boucher, D. Gambier, B.E. Keen and M.L. Watkins, "The key to ITER: the divertor and the first wall", *Proc. International Conference on New Ideas in Tokamak Confinement*, La Jolla, 1992.

[6] J. Jacquinot and the JET Team, "JET relevance to ITER, new trends and initial results", *Fusion Engineering and Design* 30 (1995), p.67.

[7] E. Bertolini and the JET Team, "JET development towards pumped divertor operations", *Proc. 15th Symposium on Fusion Engineering* , Hyannis, MA, 1993, Supplement, p.5.

[8] M. Pick et al., "The new first wall configuration of JET". *Proc. 15th Symposium on Fusion Engineering*, Hyannis, MA, 1993, Supplement, p.54.

[9] P. Thomas, "Divertor Diagnostics for JET", to be published in *Proc. of the Workshop Diagnostics for ITER*, Villa Monastero, Varenna (Italy), 28 August - 1 September 1995.

[10] M. Garribba et al., "First operational experience with the new plasma position and current control system of JET", *Proc. 15th Symposium on Fusion Engineering*, Hyannis, MA, 1993, Supplement, p.33.
[11] V. Marchese et al., "Detailed design, installation and testing of the new Coil Protection System for JET", *Proc. 15th Symposium on Fusion Engineering*, Hyannis, MA, 1993, Supplement, p.46.
[12] D. Chiron et al., "The poloidal divertor field amplifiers for the JET pumped divertor", *Symposium on Fusion Engineering*, Champaign, Ill, 1995.
[13] T. Bonicelli et al., "Analysis and specification of the performance of the new JET amplifier for the vertical stabilisation". *Proc. 15th Symp. on Fusion Engineering (SOFE)*, Hyannis, MA, *Proc. 15th Symposium on Fusion Engineering*, Hyannis, MA, 1993, Supplement, p.13.
[14] P.L. Mondino et al., "The high power die bandwidth disruption feedback Amplifiers for JET", *Proc. of the 16th Symposium on Fusion Technology*, London, UK, 1990, Vol.2, p.1619.
[15] M. Keilhacker for the JET Team, "JET Results with the New Pumped Divertor and Implications for ITER", *Proc. of the 22nd EPS Conference*, Bournemouth, UK, 1995, Spring Issue of Plasma Physics and Controlled Fusion (1995).
[16] V.V. Parail et al., "Transport Analysis of the Giant ELMs in JET",*Proc. of the 22nd EPS Conference*, Bournemouth, UK, 1995.
[17] A. Sips et al., "Experiments with TF Ripple in JET". *Proc. of the 22nd EPS Conference*, Bournemouth, UK, 1995.
[18] B. Tubbing et al., "The Operational Characteristics of a Molten and Damaged Beryllium Divertor Target in JET", *Proc. of the 22nd EPS Conference*, Bournemouth, UK, 1995.
[19] M. Garribba, R. Litunovsky. S. Puppin, "The Plasma shape and current Control System of JET". *Submitted for publication to Fusion Technology*, 1995.
[20] E. De Marchi, L. Scibile "Operation Experience with the Coil protection System (CPS)" *JET Report*, JDN/G (94)041.
[21] T. Raimondi et al., "Engineering analysis of JET operation", *Symposium on Fusion Engineering*, Champaign, Ill, 1995.
[22] J. Hemmerich et al., "Installation and inactive commissioning of the JET active gas handling system (AGHS), *Proc. of 15th Symposium on Fusion Engineering (SOFE)*, Hyannis, MA, 1993, Supplement p.37.
[23] D. Smith, *Remote Tile Exchange Mock-up Remote Handling Equipment-Reliability Status*, JET Report 1995, (TN/076).

ENGINEERING ANALYSIS OF JET OPERATION

E. Bertolini, M. Buzio, P. Noll, T. Raimondi,
G. Sannazzaro, M. Verrecchia
JET Joint Undertaking, Abingdon, Oxon OX14 3EA, England

ABSTRACT

Since 1994 the JET experiment has been operated with a divertor, with currents up to 6MA. Disruptions are generally accompanied by vertical plasma displacements giving rise to vertical forces at the torus. Vertical force swings up to 5MN were recorded at vessel support. The forces are toroidally non-uniform, with peaking factors up to 1.8. Global sideways displacements of the torus, up to about 5mm, were also recorded in a number of disruptions. They are interpreted as consequence of a large amplitude m=1, n=1 kink mode. Disruptions led to damage of some components inside and also outside the vessel, such as internal saddle coils, and Beryllium evaporator heads.

I. INTRODUCTION

Until 1992 the JET experiment was operated without a divertor. Based on an extensive analysis it was then possible to allow operation at plasma currents up to 7 MA in the limiter mode and up to about 6 MA in the X-point mode operation [1] while the original design value for extended performance was 4.8 MA. The operation limits were to a large extent determined by the forces and stresses arising at the vacuum vessel and the mechanical shell during vertical displacement events (VDEs) and disruptions, as reported previously [2]. Vertical forces up to 3.7 MN acting on the vessel supports were observed. It was concluded that, at the moment of its maximum, the vertical force is primarily caused by halo currents re-circulating in the vessel [3].

For the assessment of operation limits it was originally assumed that the halo currents and the associated forces are approximately uniform along the toroidal direction, as suggested by observations at the DIII-D Tokamak [4]. However, local measurements of intercepted halo currents [5] and measurements of forces at the vessel supports indicated the presence of large fluctuations and toroidal variations of the halo current density and the presence of substantial toroidal non-uniformities of the global vertical forces acting on the JET vessel was highlighted in May 1994. Large asymmetries of halo currents were also reported from JT-60U [6] and Alcator C-mod [7]. These findings indicate that non-uniformity of disruption forces may be an important issue of Tokamak design.

Since 1994 JET has been in operation with a pumped divertor [8]. Many new components had been installed inside the vessel, notably four divertor field coils, divertor target plates, cryo pump, and also eight saddle shaped coils intended for the control of MHD instabilities. The plasma size is reduced so that the plasma current is limited to about 6 MA. Most experiments were carried out at $I_p < 4$ MA.

New problems have been encountered during the divertor operation:

- The vertical position is more difficult to stabilise, mainly due to the smaller plasma size and the resulting reduction of passive stabilisation by wall currents, but also due to the fact that larger equilibrium field gradients are needed for the desired divertor configurations.

- The magnetic configuration with single X-point is strongly up/down asymmetric. As a consequence, rapid disturbances like giant ELMs and giant sawtooth relaxations led often to loss of stabilisation so that the plasma moved vertically by typically 1m before disrupting. This kind of VDE can cause particularly large dynamic vertical forces at the torus. Forces up to about 8 MN had been anticipated during divertor design for an upward VDE of a strongly elongated 6 MA plasma [9]

- Strong asymmetries of disruption forces and resulting vessel displacements have been observed. Various upward VDEs caused significant global sideways displacements of the torus. This phenomenon occurred to a lesser extent also during the previous operation without divertor but its importance was not realised then.

- The new in-vessel components are exposed to eddy and halo current loads, arising from fast plasma current variations during the energy quench and the current quench and from VDEs. In some cases these loads were higher than expected and caused damage to some of these components. The non-uniformity of halo currents may have enhanced local forces.

II. FORCES ON THE VACUUM VESSEL AND DISPLACEMENTS DUE TO DISRUPTIONS

A. Measurements

The vessel movements are caused by vertical and horizontal forces applied to the vacuum vessel walls, in-vessel components and divertor coils. To analyse the effects and nature of disruptions JET has a set of sensors (see Fig. 1)

a) Displacement resistance transducers attached to the main vertical ports (MVP) measure radial displacements and those attached to the intermediate vertical ports (IVP) measure vertical movements.

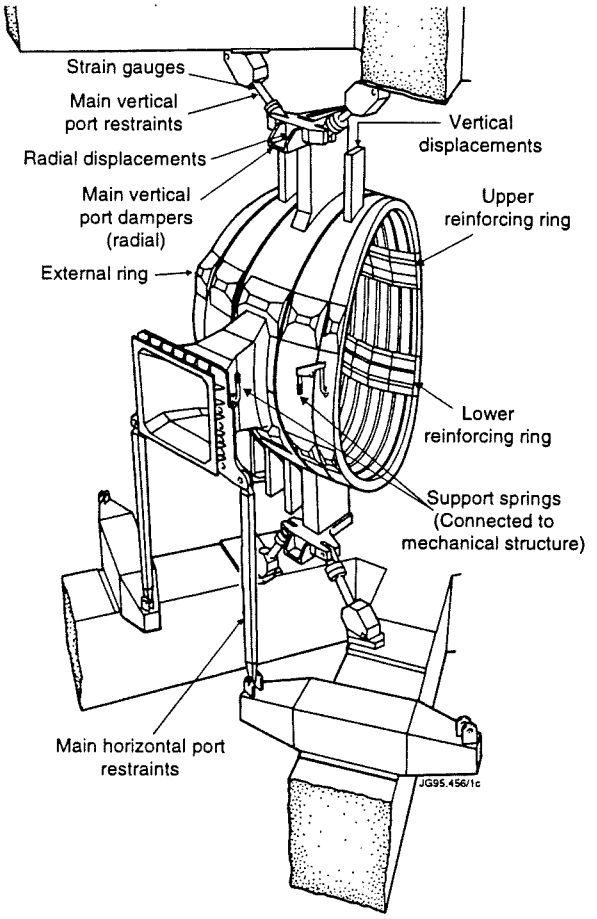

Fig. 1: Vessel Measurements and constraints

b) Strain gauges on the restraining struts at all main vessel ports at the top and bottom of the vessel measure the vertical forces applied by the vessel to the iron magnetic circuit.

c) The value of the plasma current and the displacement of its centroid are detected by measuring the tangential and radial field around the poloidal contour of the plasma. The tangential field is measured by 16 poloidally oriented pickup coils located along the inside wall of the vessel at two opposite octants (3 and 7). The radial field is deduced by "saddle loop" coils applied on the external wall of the vessel. These measurements are corrected for the contribution from divertor coil currents.

d) A number of poloidally and toroidally distributed shunts on the earthing connections of certain in-vessel components, including "mushroom" tiles, measure halo currents collected from the plasma.

Displacements and forces at supports are monitored to establish safe operating regimes.

B. *Axisymmetric effects and trends of global parameters*

All disruptions in JET, and often other types of large amplitude perturbations, produce vertical plasma displacements. In most cases the vertical stabilisation is completely lost due to saturation of a stabilising circuit. This is as would be expected because a rapid plasma current quench, which could typically be in the region of 100 MA/s, induces currents in the components surrounding the plasma (PF coils, divertor coils, vessel) which produce a transient vertical force at the plasma due to the up-down asymmetry of the single divertor configuration. To compensate this effect the radial field amplifier should supply peak voltage far in excess of its design parameters. Similarly it is impossible to maintain the radial plasma position when there is a rapid drop of plasma current. This current quench is in turn enhanced by the loss of position control and by the resulting plasma-wall interaction.

The most severe VDEs are those where the vertical instability arises before the current quench. The current moment $Ip\delta Z_p$ can then reach large values causing large global vertical forces at the torus and large halo currents affecting in-vessel components. The reasons for instability before a current quench are not clear. It is suspected that large amplitude perturbations such as giant ELMs, minor disruptions, L-H mode transitions or disruption precursors cause, in some cases, an inappropriate response of the vertical stabilising circuit. Further investigations are aimed at improving the stabilising circuit and the reliability of the magnetic measurements which are affected by noise and screening effects.

Pulse 34078, which, with plasma current 3.5 MA, resulted in a vertical instability, has been taken as an example because it shows both the trend of the global axisymmetric parameters and also the largest recorded sideways displacement of the vessel. The typical trends of the plasma current I_p, the displacements of its centroid and the total vertical force measured at the vessel supports are shown in figs. 2a, 2b and 2c respectively. This total force does not directly represent the electromagnetic forces acting on the vessel, but indicates the effect of these through the dynamic response of the vessel, ie, the inertial and constraint spring effect.

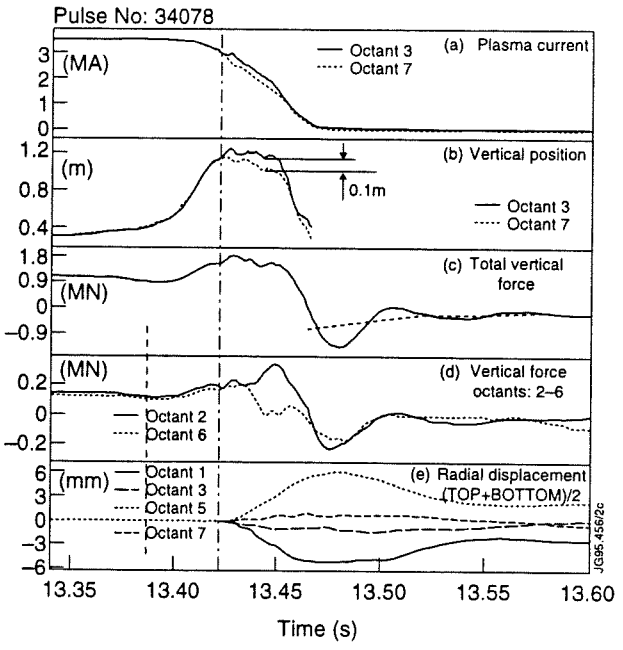

Fig.2 Vertical Displacement Event (VDE) and disruptions of pulse 34078

The vertical force at the torus consists of three contributions:
- forces on the four divertor coils; disruptions generally cause a substantial increase of the divertor currents and force variations. (see Table I)
- forces due to induced toroidal currents in the vessel
- forces due to halo currents intercepted by in-vessel elements, these currents circulate through "earthing" connections in the vessel, and also directly in the divertor target. Induced currents are due to plasma current change and the velocity of displacement whereas halo currents depend on the distance between plasma boundary and wall. Owing to their different origins the two types of forces tend not to peak at the same time. Both induced and halo currents create forces which tend to oppose plasma displacements.

Table I
Computed vertical forces and currents in divertor coils before and after the current quench of a 5 MA "SLIM" plasma

Coil	I(kA)		F_z(MN) (+ upwards)			
	Before	After	Before		After	
D1	15.6	37	-0.1	total	−2.5	total
D2	19.3	29	+0.8	+5.2	+0.8	+5.2
D3	26.7	40	+1.8		+2.1	
D4	28.6	53	+2.7		~0	

Fig.2c shows the evolution of the total vertical force at the vessel supports. In this pulse the vertical stabilisation was lost before the disruption. One recognises the presence of upward forces before the disruption caused by the divertor currents and of an additional transient upward force in the case of an upward VDE. The subsequent evolution of forces at the supports is due to magnetic forces acting on the divertor coils indicated by broken lines superimposed on the pulse dynamic response of the vessel indicated by a fundamental oscillation at ≈15 Hz. This mode is also apparent from the plot of the average difference of radial displacement of the upper and lower MVPs in an axisymmetric instability (fig. 3). It appears as a rolling/rocking motion excited by a twisting moment due to the fact that the resultant of the vertical forces, applied for a duration of the order of 10ms, is not in line with the reaction force at the MVP restraints (fig. 4).

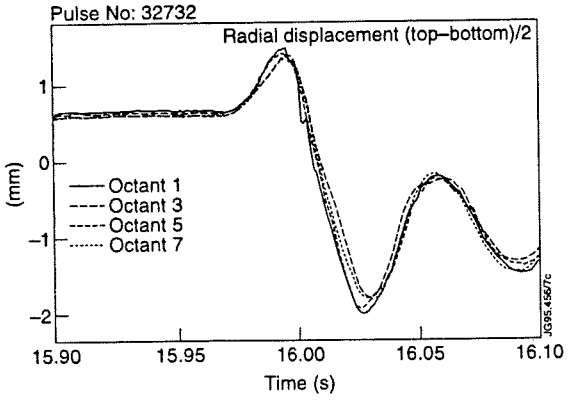

Fig. 3: Radial differential MVP (rolling motion) displacements caused by upward VDE of 3MA plasma

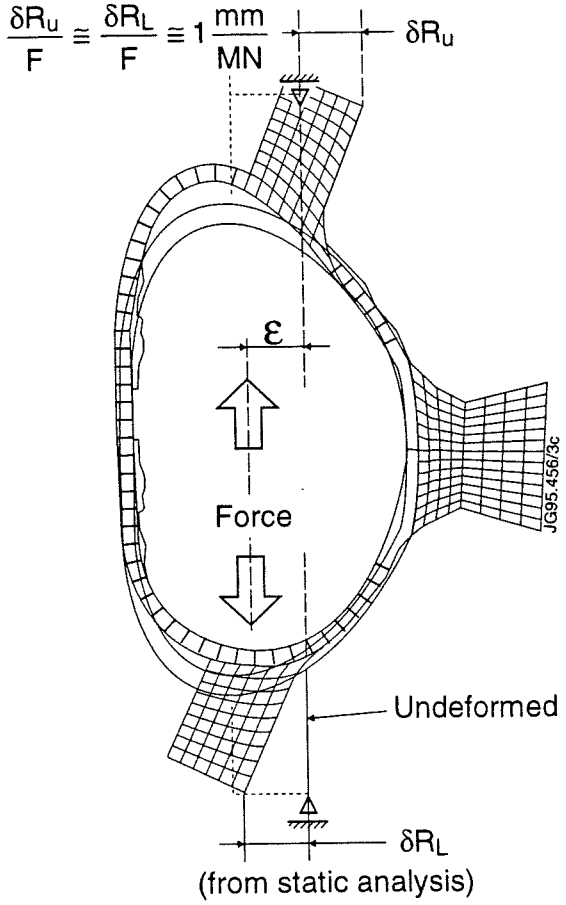

Fig. 4: "Rolling" motion

C. *Non-axisymmetric effects*

Fig. 2d presents the evolution of vertical support forces at opposite octants (2 and 6) for the upward VDE of pulse 34078. There are substantial differences of force amplitudes and of phases. One notes, in particular, that the peak force at octant 2 is accompanied by a minimum at the opposite octant 6. Similar behaviour is shown in other disruptions. Reasons for these asymmetries could be either the asymmetry of the vessel restraints such as the large neutral beam injector boxes at the horizontal ports of octants 4 and 8, or the asymmetry of the electromagnetic forces. However, since in various pulses it has been noticed that the distribution of the asymmetries varies, ie, the max. peak force does not always occur in the same octant as one would expect if the non-axisymmetric distribution of forces depended on mechanical asymmetries, one deduces that it is the distribution of magnetic forces which is non-axisymmetric, presumably because of non-symmetric induced or halo currents.

Fig. 2e shows the average radial movement of the top and bottom MVPs on the instrumented octants. Note that the ports on octant 5 move outwards and those on octant 1 move inwards with respect to the central axis of the machine. The movement of octants 3 and 7 are much smaller. From the vector sums of the average octant displacements it appears the whole vessel moved approx. 5.6mm in the direction between octants 5 and 6.

The MVP restraints have been mainly designed to resist vertical loads and they are free to move radially. They do not allow movement of the extremities of the ports in the toroidal direction; therefore they resist sideways movement of the vessel. The maximum resultant sideways reaction force amounting to 0.55 MN is reached at time 53.46 (corresponding to the time of the maximum sideways movement of the vessel). The natural frequency of the sideways movement appears from fig. 2e in the region of 3 Hz and is in good agreement with the figure that can be derived from the vector resultant of the toroidal stiffness of the MVPs and the global inertia of the vessel (~240t).

Considering this low natural frequency the horizontal electromagnetic force which is applied to the vessel for only 10-20ms must have been much greater than 0.55MN and can be estimated, using the dynamic response of the bulk of the vessel, in the region between 1 and 2MN.

The plasma configuration is an approximate lower current analogue of a prospective 5MA high performance plasma, exhibiting high flux expansion around the target area by using currents in all four divertor coils. The safety factor q95 is about 2.5. It is important to investigate whether large sideways vessel displacements are a feature of this configuration or if they occur also in VDEs of other plasmas.

In pulse 34078 the VDE was most probably caused by a fast rotating n=2 helical plasma mode (~5kHz) with large amplitude, which started 0.6s before the VDE after a giant sawtooth. The feedback signal is not compensated for pick-up of this mode. The mode therefore caused frequent switching of the Fast Radial Field Amplifier to maximum level (~10 kV) and premature disabling of some FRFA units, whereupon the vertical stabilisation deteriorated and was lost around 53.3s.

Fig. 2b shows the movement of the current centroid position derived at octants 3 and 7. Up to a vertical displacement of about 0.8m the agreement of signals from the two octants is very good, but from 53.42s, when the plasma is close to the vessel wall, the central centroid in octant 3 is about 0.1m higher than in octant 7. If we interpret this as a mode m-1, n-1, equivalent to a tilting of the plasma the resulting force acting on the plasma due to the interaction with the toroidal magnetic field would be about 1.1MN in the direction octant $1 \rightarrow 5$. Since each plasma element is in a quasi stationary equilibrium this force would have to be balanced by other toroidally asymmetric forces such as induced or halo current forces generated in the vessel which could explain the observed sideways movement.

It should be noted from fig.2e that the sideways movement of the vessel starts at the same time $t \approx 53.42$s as the departure of the vertical plasma position from toroidal symmetry. A detailed analysis shows that at this moment also the toroidal distribution of the vertical forces measured at opposite vertical ports (fig. 2d) starts to become non-uniform. A correlation between the horizontal force and the asymmetries of the plasma vertical position appears likely from the observation that in two disruptions exhibiting a reversal of the sideways motion $1 \rightarrow 5$ and $5 \rightarrow 1$) the difference between vertical forces at the octants 90° from the direction of motion (octants 3 and 7) is also reversing.

At present there is no direct measurement available of the total poloidal component of the halo current. Some indication of the halo current is obtained from mushroom tile currents (shunt measurements). These intercepted halo currents are generally very erratic and not toroidally uniform in all cases. However a particularly marked departure from axisymmetry is clear when the sideways forces are produced [10].

Sideways movements with significant amplitude (>1mm) have not been observed in downward VDEs up to now. This could be due to noticeably faster disappearance of the current, and hence the force, which might be ascribed to the lower time constant due to a tighter coupling between plasma and divertor coils.

III. STRUCTURAL CONSEQUENCES OF DISRUPTIONS

Disruptions, particularly when the plasma is in proximity of the vessel wall, may cause damage to in-vessel components. Asymmetric VDEs in particular give concern because they can cause higher local stresses due to the peak factor. Sideways movements may endanger the constraints of the vessel, most notably the connections to the Neutral Injectors which, due to their large masses, behave as fixed constraints. Modes higher than the fundamental (~14Hz) can be excited and an analysis is needed to quantify their effect.

A. *Analysis of stresses induced by sideways motions of the vessel*

The vessel is restrained in toroidal direction by the struts connected to the MVPs, and by the Neutral Injectors (NIs), through the rotary valve cases. Its F.E. model has been obtained by mirroring and rotating the existing half-octant model and includes 120,000 d.o.fs.

A load of 0.55MN, measured in pulse 34078 as a resultant of the load differences detected in adjacent legs, was applied to the inboard side of the model. The average static deflections and the natural frequency calculated were in reasonable agreement with the one measured as the resultant of the radial movements of the MVPs. The model, thus validated, indicates max. stresses at the root of the MVPs of approx. 92MPa, to which we have to add stresses due to axsymmetrical displacements.

The stresses at the MHP connections to the NIs are evaluated separately in two cases (fig. 5):
a) sideways motions parallel to the NI front flange
b) sideways motion normal to case a).
In case a) the clamps linking the rotary valve to the NIs and to the vessel behave as two elastic hinges, which give an elastic restoring force on each port of approx.

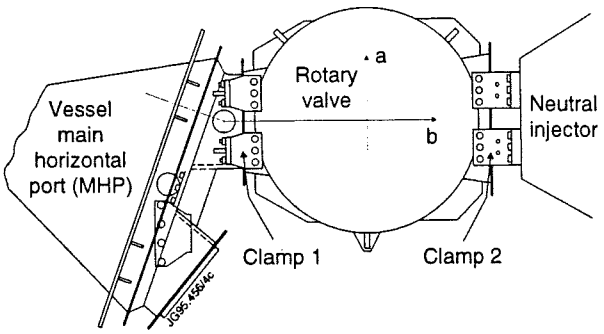

Fig. 5: Connection between MHP and Neutral Injector (plan view)

10kN/mm. This acts in parallel to the reaction from the restraints and gives negligible stress in the vessel structure for low frequencies.
In case b) the clamps are rigid and the forces derive from the inertial loads of the NIs (masses of ~80t free to move radially) and are limited only by the elasticity of the vessel port sector. F.E. analysis shows a max. stress of 140MPa for the max. vessel displacement seen. A full modal analysis is being done and new instrumentation will be installed during the present shutdown to detect radial and tangential motions of the MHPs to reveal any higher vibration modes which are potentially dangerous for peripheral parts such as windows.

B. *Analysis of stresses induced in divertor coils*

In an upward VDE of the worst configuration identified, 5MA SLIM plasma, the current in divertor coil no.4 may reach 53kA, due to the induction effect caused by the plasma current quench. This gives rise to centripetal forces and potential buckling particularly because of the large diameter of the coil. This effect has been studied in detail to establish the safety margin, considering errors of circularity as manufactured, the effect on their stiffness of their composite structure with copper and epoxy layers, and their response to the impulsive electromagnetic forces.

Since the contribution to deflection of the equivalent shear module was found to be negligible, the stiffness product E.I. can be safely assumed as that of the copper only. The coils are considered to have some initial ellipticity, assumed conservatively to be a radial deviation of 6mm. This is amplified by the impulsive load, a function of the dynamic response to this mode, and causes an impact on the tangential restraints which in the worst combination does not exceed 40MPa.

Thermal shear stresses in toroidal direction were evaluated and found to be below 10MPA, with max. differential temperature between adjacent turns of 20°C. They may be combined with a primary vertical shear stress of 10MPa.

C. *Stresses in TF coils*

Following disruptions at 6MA with FAT plasma the stresses in the TF coils have been recalculated with the prospective increase of B_{tor} to 4T at 78kA from the nominal 3.45T at 67kA.

This was done with FE Abaqus code. The stresses are due to "in plane" loads, ie, tension and bending caused by D-shape errors, and "out of plane" loads, ie, torsion and transversal forces. The max. shear stress of 9.5MPa in operation is reduced to 6.7MPa at disruption, by the effect of induced current in the divertor. These occur at the centre of the cross section and are given by the vector sum of the in plane and out of plane shear stresses, in proximity of the inner cylinder grooves.

The side supporting teeth of the ring and collar of the mechanical structure were also a point of concern and have been re-evaluated. The max. side load acting on the teeth was calculated as 750kN, compared to the allowable value of 830kN.

D. *In-vessel components damaged during 1994-5 operations*

D1. *Saddle Coils (fig. 6)*
The saddle coils, installed during 1992-3 shutdown were designed to mitigate disruptions and control non-axisymmetric modes. The coils, when not yet operational, were temporarily short-circuited and grounded outside the vessel so as to limit internal induced voltages and the risk of breakdown. In September 1994 the upper saddle coils were found damaged. In octants 2,4,6 and 8 the L-shaped bars which are the transition between toroidal and poloidal sections had been distorted. Looking from the centre of the machine, the right hand busbars were bent towards the tokamak central axis and the left hand busbars were bent towards the plasma. The terminals of the crossover bars at the inner wall side were also bent and one of the ceramic insulating balls of the end support had been pushed out. From the damage it was assessed that a current of at least 14kA had passed through the conductor while the nominal operating value was 3kA.

Observed measurements of the induced current in the lower saddle coils at the plasma energy quench show large current spikes of 1-2ms duration in a direction consistent with the permanent deformations. Similar spikes are also seen in the induced voltages in the upper saddle coils reconstructed from magnetic measurements. These are however not quite large enough to explain quantitatively the effects seen, considering the dynamic amplification factors, unless they are attenuated for fast events or by electronic saturation. Halo currents and arcing may have contributed.

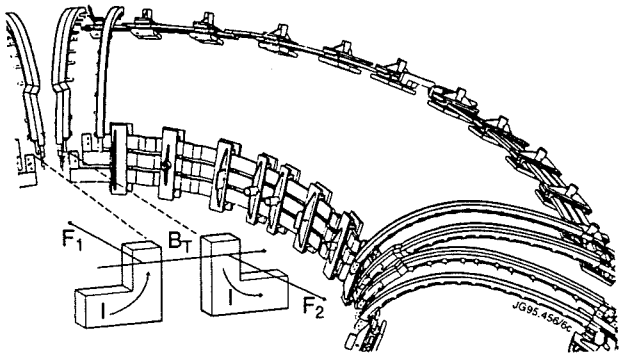

Fig. 6: Upper saddle coils (Partial view)

As a remedial action the upper saddle coils have been disabled and resistors have been placed in the crowbar circuits of the lower saddle coils to limit the induced current. The L-shaped bars in Inconel 600 have been replaced by stronger versions in Inconel 625 and the flexible links between toroidal and poloidal sections have been made stronger.

D2. Beryllium Evaporator Heads (fig. 7)
Four Be evaporator heads are inserted into the vacuum vessel for Be evaporation at the equatorial plane of octants, 1,3,5 and 7, using a pneumatic system and retracted during plasma operation. Previous to the divertor installation the Be heads were parked behind the inner vessel wall. For divertor operation the evaporation position of the Be heads was changed to give better coverage of the divertor. Consequently the retracted position was changed to about 400mm within the vacuum vessel, exposing the head to a larger poloidal field change.

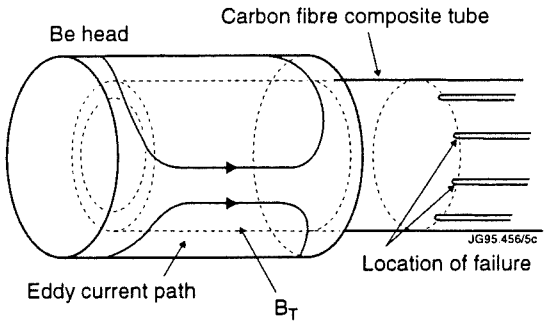

Fig. 7: Beryllium evaporater head

In November 1994 one of the evaporators broke and another was found severely damaged. The fracture location was at the end of some slots in the carbon fibre composite (CFC) tube which supports the Be head. The support cylinders of the damaged heads were made of an inferior grade CFC and had lower mechanical strength than the others. The damage is believed to have been caused during pulse 32275 by induced currents in the Be heads due to a poloidal field change in the region of 50T/s extrapolated from measurements on pickup coils on the vessel wall. The twisting moment caused by the interaction with the toroidal field is estimated at 400Nm, taking into consideration the magnetic damping and dynamic effects. Mechanical tests on the correct grade CFC tubes gave a failure twisting moment of 350Nm.

The weaker CFC tubes have been replaced and the retracted position of the Be heads is now behind the inner vessel wall. A modified version will be installed during the Mk II shutdown incorporating the following improvements: shorter slots, increased thickness of the CFC tube at the position where it failed and slots in the Be heads to reduce the induced current.

IV. CONCLUSIONS

Rather violent vertical disruptions have occurred during the latest series of operating campaigns with consequent damage to structural components. These events are particularly difficult to analyse when the plasma is in close proximity to the vessel wall. Sharp field variations at the boundary are difficult to measure and predict. Disruptive modes are frequently non-axisymmetric and understanding them presents many difficulties. More comprehensive and precise instrumentation with better signal to noise ratio is needed and efforts will be made in this direction during the present shutdown

With the divertor configurations in H-mode experimented in JET during recent operations with I_p ~3MA the peak factor, ie, the ratio between maximum and average vertical force per octant was up to 1.8 and the ratio between the max. horizontal force and max. vertical force attained values of around 0.5. However these data are only indicative and cannot be extrapolated to obtain design specifications at full current or in other configurations. Much more systematic and comprehensive testing and analysis are needed.

During disruptions the stresses in the vessel structure and coils were not particularly severe. A vessel survey showed no permanent deformations. It could be argued that the inherent flexibility of the vessel is not a drawback if it absorbs impulsive forces inertially and oscillations are limited by suitable damping.

The damage to in-vessel components has been analysed and remedial action taken. This consists of redesign of details and reinforcement, or where this is not possible issue of operating instructions which ensure the electromagnetic load is within acceptable limits. Components which protrude from the vessel wall in proximity of the plasma are inevitably at risk and are to be avoided.

Use of a smooth first wall and of a plasma configuration which is easy to stabilise appears a necessary strategy in view of a fusion reactor. The possibility of having non-axisymmetric disruption forces and net sideways forces at the torus of a fusion reactor suggests that a better understanding of such phenomena is needed to find ways of avoidance, or to foresee adequate safety margins for non-axisymmetric forces.

REFERENCES

[1] M. Huguet, E. Bertolini and the JET Team, "JET Progress towards D-T Operation", *Fusion Technology*, vol 15, pt 2A (March 1989) p.245.
[2] P. Noll, L. Sonnerup, C. Froger, M. Huguet and J. Last, "Forces at the JET vacuum vessel during disruptions and consequent operational limits", *Fusion Technology*, vol 15, pt 2A (March 1989) p.259
[3] M.A. Pick et al, "Evidence of Halo Currents in JET", *Proceedings, 14th Symposium on Fusion Engineering, (SOFE) San Diego*, IEEE (1991), p.187
[4] E.J. Strait et al, "Observation of poloidal current flow to the vacuum vessel wall during a Tokamak vertical instability", *Nucl. Fusion*, vol 31, no.3 (1991) p.527

[5] P. Noll et al, "Experience of electromagnetic forces during JET divertor operation", *Proceedings of the 3rd International Workshop on Electromagnetic Forces held in Capri, Italy (*August 1994), p.11
[6] Y. Neyatani, "Recent progress in JT-60U experiments", *Fusion Engineering and Design 30,* (1995), P.25
[7] R. Granetz et al, "Halo current during disruptions in Alcator C-Mod", *present at the ITER Disruption Expert Group Workshop, Garching, Germany,* 13-17 Feb 1995.
[8] E. Bertolini and JET Team, *"JET with a Pumped Divertor. Technical issues and main results"* to be presented at SOFE 95.
[9] P. Noll et al, "Electromagnetic forces during JET divertor operation", *Proceedings of the 2nd International Workshop on Electromagnetic Forces held at Tokai, Ibaraki, Japan,* (Sept 93), P.9
[10] P. Andrew et al "Measured Currents in JET Limiters during Disruptions" to be presented at SOFE 95

MANUFACTURE AND INSTALLATION OF JET MKII DIVERTOR SUPPORT STRUCTURE

G. Celentano, H. Altmann, B. Macklin, P. Miele, L. Moletta[1], M.A. Pick, A. Romagnolo[1], R. Shaw[2], J. Tait,
JET Joint Undertaking, Abingdon, Oxfordshire, OX14 3EA, UK
[1]Sulzer-De Pretto, Schio, Italy
[2]ITER EDA, San Diego, USA

ABSTRACT

The water cooled support structure, comprising twenty-four modules is the main component of the JET MKII divertor system. It is to be installed in the vacuum vessel with high accuracy with respect to the magnetic centre and the other in-vessel components.

The paper describes the design and manufacturing cycle including the required tolerances, the assembly and installation method and the material production process required to ensure the accuracy and reliability of the MKII support structure system. The water cooling holes, machined into the support structure require the procurement of special material to prevent risks of leaks inside the vacuum vessel.

The design of the support system had to be such that minimal modifications to the existing in-vessel structures were required. A detailed tolerance analysis identified the accuracy required at each stage and helped in establishing a suitable manufacturing and assembly process. Major attention was given to the design and manufacturing of the joints between the modules which, due to access restrictions in the vessel, can only be assembled from one side. A tight tolerance of the joint components to ensure mechanical integrity and stiffness of the module joints is opposed by the necessity to have a realistic assembly tolerance.

The pre assembly of the whole ring of modules at the manufacturers' works, which is a rehearsal of the final installation procedure, aims to test the achievement of the design requirements and to ensure the feasibility of the in-vessel installation.

INTRODUCTION

The MK II support structure is a "continuous target" design inertially cooled which provides a closed configuration. This leads to an increased impurity and neutral particle retention, increased power handling capability, reduced power being conducted to the target plate, and reduced heat transfer to the divertor coils, better alignment of the target at the installation and creates a flexible system for studying different divertor configurations and concepts. The structure itself will be a permanent fixture inside the Torus. MKI and MKII divertor design and operational features discussed extensively in other papers [1/2/3/4].

MKII DIVERTOR MECHANICAL DESIGN FEATURES

- The support structure is made up by three concentric rings consisting of a base plate plus inner and outer ring.
- The structure sits on the divertor coil clamps 2 and 3 which are welded directly to the lower vessel wall, and therefore are completely decoupled from the coil casing. The structure is manufactured - as 24 modules (sub-assemblies) which represent the largest size that could fit through the horizontal port of the vacuum vessel. The modules will be assembled together to form a circular structure once inside the JET vacuum vessel by means of fish plate, fasteners and dowels. The structure contains the accurate locations for the installation of tile carriers. The tile carriers are designed as a lightweight and rigid structure, holding tiles and diagnostic and their electrical connections. The tile carriers are fully remote handleable.

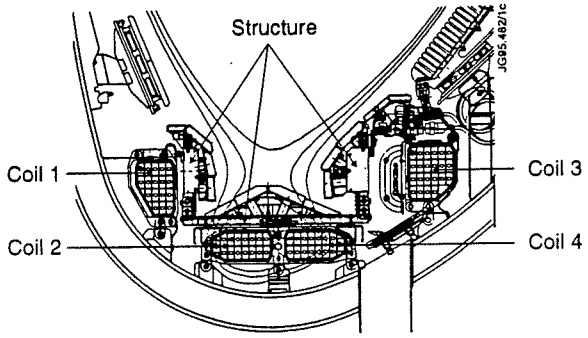

Fig. 1 Cross sections MKII structure

MANUFACTURING OF MKII DIVERTOR STRUCTURE

Some of the critical issues of the design of the MKII divertor structure which affects the manufacturing aspects are presented below:

1) Raw Material

The material selected for the manufacture of MKII support structure is Alloy 600. The base plates and rings are machined out from solid plate (45mm thick) and bars (80-120mm thick) respectively.

The extensive machining of pockets and deep drilling of the water cooling system channels generates a "honey-comb" structure with thin vacuum retaining walls (about 4mm). One of the problems in producing high nickel alloy thick plates or bars is the segregation of chromium and titanium carbides that may precipitate in laminar bands during the rolling process. Although these bands have no apparent effect on mechanical properties they may compromise the vacuum tightness, especially with a thin wall and high

temperature. Therefore a special process had to be developed for this material (thick plates) to fulfill the design requirements in order to:

- minimise laminar segregation of chromium and titanium carbides (vacuum tightness) carbon <0.02% titanium <0.01%.
- achieve uniform metallurgical structure (machinability and dimensional stability).
- control the level of non-metallic inclusion (vacuum tightness and weldability).
- achieve fine grain size (corrosion from demineralised water and mechanical properties).

The melting and production process developed by VDM Germany to meet the above requirements is basically:

- Electric arc melting followed by vacuum oxygen decarbonizing process (VOD).
- Casting of electrodes.
- Remelting by DESR (electro slag) process to produce ingot of ø1000mm size.
- Forging and transverse rolling to slab of 100mm thickness.
- Final hot rolling to 45mm plate.
- Total reduction Y 91%.
  R = 11.2 Reduction rate.

Extensive trials were carried out to achieve the best compromise between the reduction ratio during the hot forming and the temperature and holding time during heat treatments so as to generate a uniform and fine metallurgical structure.

In addition to the mechanical and metallurgical acceptance test each plate or bar has been tested from the vacuum point of view. A slice of material representing the full cross section of the plates or forging was cut and welded to a box to be hot leak tested. The thickness of the material slice is representative to the wall thickness of the divertor structure.

82 tonnes of material were produced by the German company, and 23 tonnes of good material was delivered to JET. After machining, the weight of the structure is approximately 6 tonnes.

2) *Rigidity of the module's structure*

The divertor structure forms an electrically conducting ring inside the torus magnetic field. The high electrical resistivity of the material and the minimal cross section area in the toroidal direction of the structure reduces the induced current.

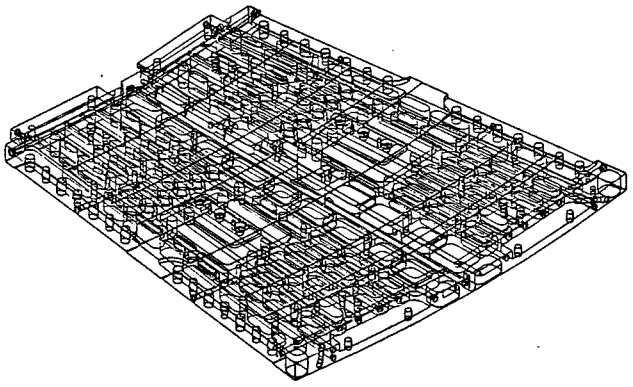

Fig. 2 Machining of base plate

The electro magnetic forces arising from plasma disruption and halo currents, impose the requirement to design a light but rigid structure. A honey-comb structure is generated by machining into solid plates or forged bars a set of pockets and holes. About 65% of the initial weight of the material is removed by machining.

The rigidity of the plates or bars is achieved by making up a sandwich structure after the machining of the pockets.

A brazing method was selected to join the lid to the base plate (brazing alloy Ag Cu Pℓ 10 PALCUSIL 10 from Wesgo) and Electro Beam welding method for the inner and outer rings.

Both systems are NDT tested by ultrasonic scanning.

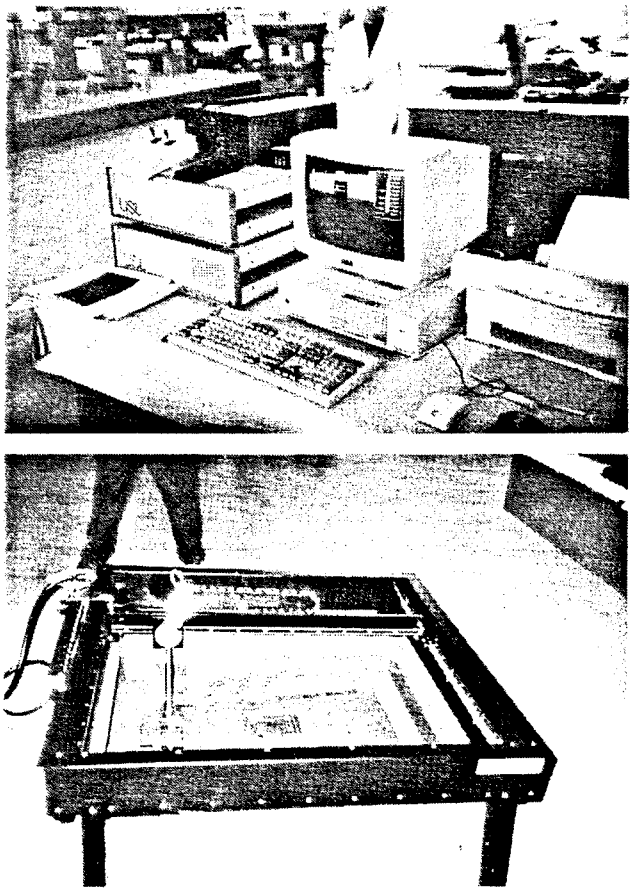

Fig. 3 Ultrasonic equipment for brazing

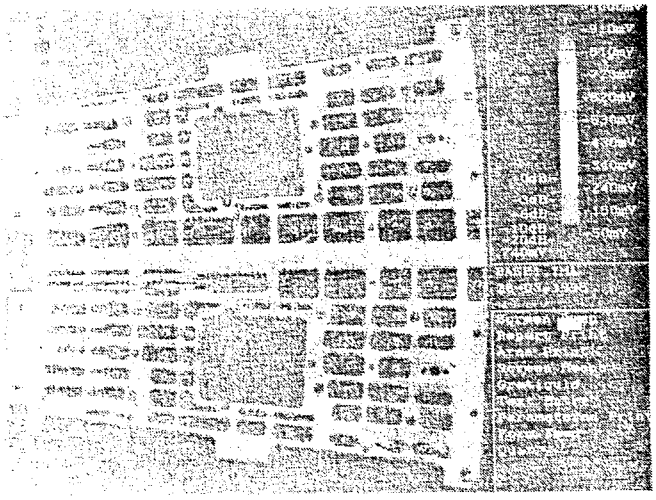

Fig. 4 US print of brazing test

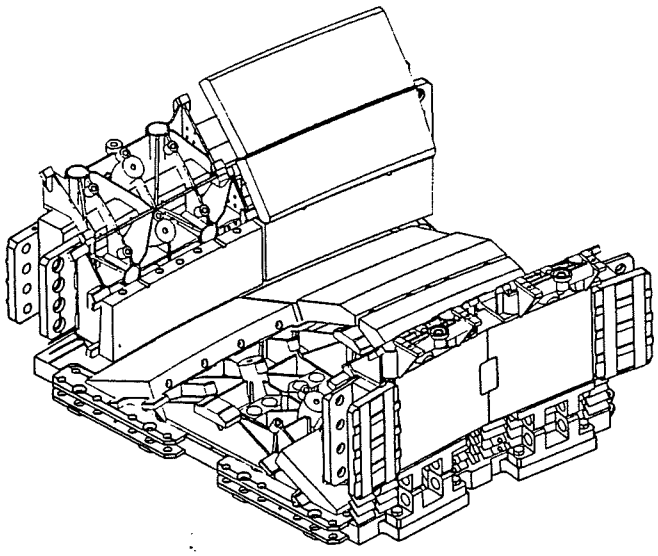

Fig. 5 Module joints

3) Module joints

The joint between the modules is one of the important features of the design and it is the one that predominantly affects the manufacturing cycle.

The joint design has to provide:

- perfect alignment between all modules to minimise steps between tiles.
- stiffness to minimise deflection under loading
- accurate fit of the dowels to evenly distribute the shear load and to prevent any slackening.
- suitable assembly method of the modules inside the Torus without using special fixtures.

The design of the joint envisages a system of fish plate and dowels which has to be co-drilled and machined together with the modules assembled as a closed ring in their final position.

To maintain the design stiffness requirements a tight fit tolerance of the dowel/hole g6/H7 in accordance with ISO standard was considered suitable and was selected (typical ø16mm dowel g6 = $\frac{-6\mu m}{-17\mu m}$ hole H7 + $\frac{-0}{18\ \mu m}$). In order to prevent seizing, during the insertion, all dowels are coated with a silver flash of about 5µm.

The developed machining cycle implied to machine the joint features of the three main components (base plate/inner ring/outer ring) individually assembled to form a closed ring. For this scope a special "plateau" was produced to support and set the rings during the machining and assembly operations. Eventually the three rings were assembled together onto the "plateau" to form the complete circular structure. After this operation the structure was split in 24 individual modules and fitted with all small items such as louvre - hinges - nozzles etc.

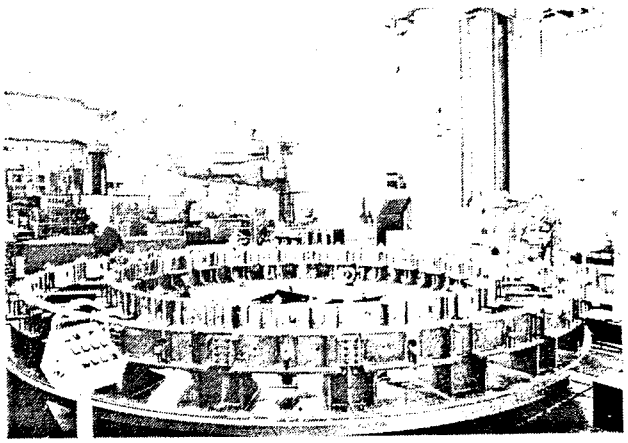

Fig. 6 Machining of the inner and outer rings on the platform

ASSEMBLY PREPARATION AND IN-VESSEL INSTALLATION

The restricted space and hostile environment (radiation and beryllium contamination) defined certain design parameters. These included the size and weight of the structure modules, the type of joint and the support system.

A detailed and extensive tolerance exercise was carried out to ensure adequate clearances between the structure and in-vessel components both during and after installation.

As part of the overall shutdown preparation an accurate full size mock up IVTF (In-vessel Training Facility) was made representing few octants. Three dummy modules were used to prove the handling inside the vessel and the use of the Remote Handling Boom to insert a module into the I.V.T.F. The dummy modules were also used to develop the technique and tools for assembling a joint while wearing full

pressurized suits (each joint had 32 dowels and 24 bolts). This development work had to be carred out in a limited timescale so that the experience gained could be used for the assembly of the modules at the manufacturers.

Extensive survey development work was carried out based on the CAT system (Computer Aided Theodolite) [5].

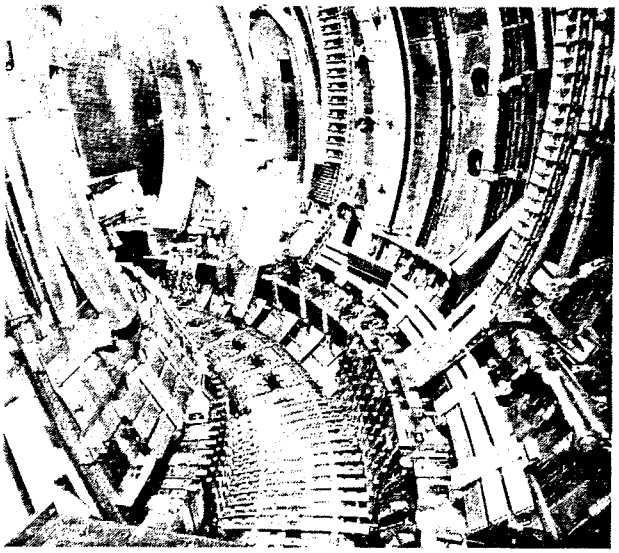

Fig. 7 Vessel training facility during installation of dummy modules

The manufacturing contract envisaged to perform the final assembly at the manufacturer works, following the same procedure as for in-vessel installation and using the tools and methods developed in the I.V.T.F. JET personnel were part of the assembly team to gain the necessary experience to be used later on at JET site for the final installation.

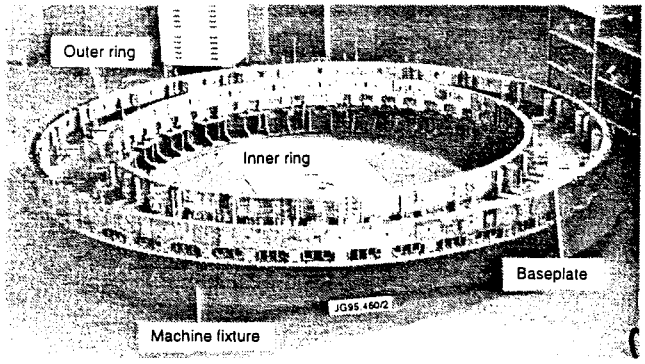

Fig. 8 Final assembly at the manufacturer works

The installation sequence basically envisages the following steps:

Preparation of the modules ex-vessel. This includes: diagnostic - wiring - gas introduction - earth straps etc.

Transfer of the module into the vessel using the articulated boom.

In-vessel handling with a purposebuilt toroidal crane.

Setting of the first module to the magnetic centre radially and toroidally to the microwave system of diagnistic antenna in octant 3.

Installation of the adjacent modules monitoring the position by using the CAT survey system. The modules are joined by using the fish plates and dowels.

Progressive installation of all the modules to build up the complete ring. Position and setting controlled by CAT system.

Closing of the MKII structure by inserting the last module using special jacks and fixtures to achieve the final fit of the dowels.

Final digital photogrammetry survey.

CONCLUSION

The manufacture of MKII support structure and the final assembly at Sulzer/De Pretto works has been successfully accomplished in twelve months.

The accuracy achieved is within ± 0.3mm in the overall structure geometry (steps not detectable) and this has enabled ring assembly to proceed without any problems. The hot leak test carried out at at 400°C confirmed the manufacturing cycle and the material production process to be correct. The modules are now under preparation at JET site to be installed into the JET vacuum vessel in one months time.

ACKNOWLEDGMENT

The authors would like to thank A. Nowak and A. Franklin for their major contribution to the project. The collaboration of the staff of: JET First Wall Division, JET Drawing Office, GEC Main Assembly Contractor, DE Pretto Escher-Wyss Special Construction Department, JET Vacuum Group and JET Quality Assurance Group has been significant for the successful manufacture of the MKII structure.

REFERENCES

[1] M. Pick, "The new First Wall configuration of JET", Proc of the 15th SOFE, Hyannis (Mass, USA): Oct 93 JET-P(93/88)

[2] G. Celentano, "The installation of the JET MKI Divertor features and achievements" 18th SOFT, Karlsruhe, Germany: 1994

[3] A. Tanga, "First results with the modified JET" Proc of the EPS meeting, Montpellier, France: 1994, JET-P(94)35

[4] H. Altmannn, "Design of the MKII Divertor with large carbon-fibre composite tiles", 18th SOFT, Karlsruhe: 1994

[5] B. Macklin, "Application of 'best fit' survey techniques for Design, Manufacturing and Installation of MKII Divertor at JET, 16th SOFE 1995, USA

THE POLOIDAL DIVERTOR FIELD AMPLIFIERS FOR THE JET PUMP DIVERTOR

D. Chiron, N. Dolgetta, M. Garribba, M. Huart, L.v. Lieshout[1], P. Noll, B. Sjouw[1], F. Zannelli
JET Joint Undertaking, Abingdon, Oxon OX14 3EA, UK
[1] Holec Projects bv, Bornsestraat 5, 7556 ba Hengelo, NETHERLANDS

ABSTRACT

Four new amplifiers have been procured to feed the new divertor field coils of JET. They have been operated successfully since the beginning of 94. The paper presents their main characteristics and the operational experience acquired during experimental campaigns.

I. INTRODUCTION

The new JET pump Divertor [1] relies on a poloidal magnetic configuration with open field lines at the edge of the plasma to draw impurities onto target plates. This magnetic configuration is obtained by a magnetic null (X- point) created by circulating a DC current in four new coils installed in the JET vacuum vessel (fig. 1). In order to reduce the localised heat loading on the target plates, the X-point is moved sideways (sweeping) at low frequency (4Hz) by redistribution of the current in the four coils. The divertor coils are connected to four independent power supplies to provide the required DC current "sweeping" and the X-point position control. The main features of the Divertor Field Amplifiers called PDFAx (with x=1 to 4) and the operational experience acquired during experimental campaigns are presented and discussed hereafter.

II. PDFA SYSTEM OVERVIEW

Each PDFAx feeds its own divertor coil Dx. The connection is made by water cooled copper busbars in the JET basement to cope with the limited space available and then by aluminium busbars up to the amplifiers.
In order to get the maximum flexibility, each PDFAx could in principle be connected to any coil Dx by using the changeover link facility which also enables to reverse rapidly the polarity of any coil to meet the operational requirements. Due to the possible occurrence of high induced voltages anticipated from simulations of disruptions with PROTEUS

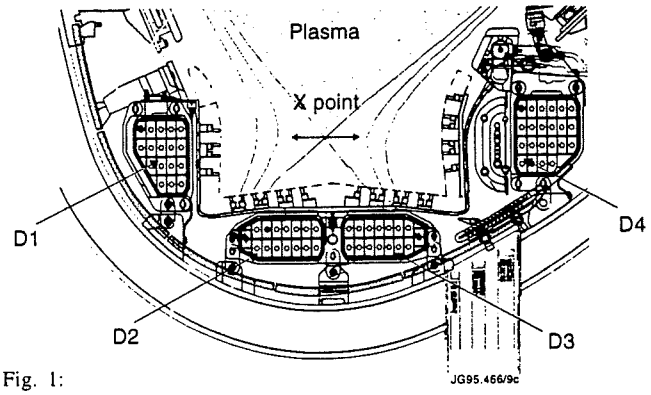

Fig. 1:

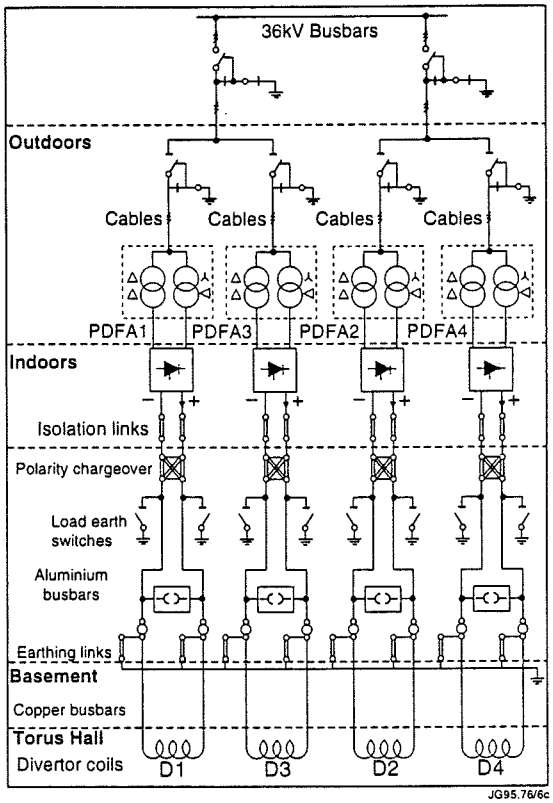

Fig: 2: Configuration of the Poloidal Field Divertor System PDFA

III. POWER SYSTEM DESIGN

(up to 40kV with the coil in open circuit during disruption), Spark Gaps have been fitted along the aluminium busbars in addition to the internal overvoltage protection of the amplifier. Their triggering level has been set to 5kV to be compared to a maximum amplifier protection level of 3.6kV in the Series Configuration (PDFA2,3).

III. POWER SYSTEM DESIGN

Each PDFAx is a "twelve pulse" thyristor rectifier consisting of two identical modules which can be connected either in Parallel or in Series Configuration. The two modules are supplied from the 36kV intermediate voltage by two independent transformers fitted in the same tank (with off-load tap changer for PDFA2,3). The voltage impedance of the transformers (7% at nominal rating, 8kA DC in the Parallel Configuration) has been chosen so that the prospective short circuit current peak in the busbars does not exceed 172kA and the overlap angle μ be less than 60° electrical.

The connection between the 2 transformers and the 2 rectifier modules is achieved by means of 24 cables. This solution produces a good current sharing factor, better than .95. On the DC side, the modules are interconnected by copper bars via air cored chokes (45μH) to limit the ripple current (1.4kA rms in the worst case) in the Parallel Configuration and the asymmetric current peak during a possible short circuit at the output of both configurations.

Each module consists of 2 water cooled copper stacks, each stack holding 3 bridges of 6 thyristors (ITav 2220A, Vdrm 2300V for PDFA1,4 and Vdrm 2800V for PDFA2,3). A safety factor of at least 2.25 has been applied between the AC voltage (peak) and Vdrm. Each thyristor is protected by fuse against overcurrent and by individual snubber to limit the turn-off voltage peaks to a maximum of 70% of Vdrm.

Each module is individually protected against overvoltages from the load by a bipolar thyristor crowbar assembly (Fig.3) consisting of two 80mΩ dump resistors (10 ceramic resistor disks in parallel for each, ϕ=152mm), each connected to a pair of antiparallel thyristors. One is used to provide a freewheeling path to the bridge current (negative crowbar) and the other (positive crowbar) to provide a current path to induced negative currents (opposite to the normal bridge current). Each thyristor crowbar is triggered by its own breakover diode and the crowbars of both modules are intertriggered to guarantee simultaneous triggering, and good current sharing through the freewheeling path.

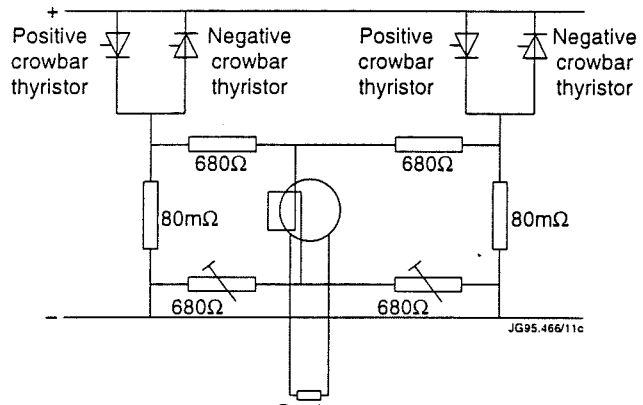

Fig 3:

Each PDFA pole is connected to the JET earth via a midpoint resistor (1kΩ between each pole and earth) . The neutral connection cable (between the midpoint and earth) is fitted with an earth leakage detection system.

IV. OPERATION MODES

The PDFA's are mainly operated in three modes:

- FREEWHEEL MODE is the normal status of the rectifier between JET pulses or after a protective action which does not require the trip of the HVCB. In this mode the freewheel path is made through one of the three branches of each thyristor bridge (chosen as the last one in conduction at the time of the freewheel command).
- BRIDGE MODE is one of the two modes used during JET pulses. The amplifier output voltage is proportional to the reference issued from the computerised Plasma Position and Current Control system (PPCC) [2]. In this mode the blocking capability of the PDFA's is provided by the maximum negative voltage available when the rectifier bridges are in full inversion .
- BLOCK MODE is the other mode used during JET pulses, more exactly during plasma breakdown. The blocking capability of the thyristor bridges is increased up to the triggering levels of the crowbars (table 1). In this mode, the PDFA internal control system first reduces to zero any residual current by forcing the bridges to full inversion and then suppresses the pulses to the thyristor gates. As a result, the complete thyristor bridge behaves as an open switch as long as the voltage induced from the load is smaller than the triggering level of the crowbars.

V. MAIN PROTECTIONS

Fast protection circuits are implemented against:

- AC primary overcurrents , measured by ACCTs in each phase of each transformer primary
- presence of gas and over-pressure in the transformer tanks (Bucchholz)
- AC secondary overcurrents, measured by ACCTs in each phase of the transformer secondary
- fuse blown
- DC overcurrent for each module measured by DCCTs
- Differences between the total DC current measured by the DCCTs and the total DC current calculated from the AC measurements (Differential protection)
- abnormal current sharing between bridges, measured on the AC side for each branch of each thyristor bridge by ACCTs with discrimination of the currents in each thyristor (by splitting the positive part and negative part of the current signals)
- too high thyristor junction temperature (simulated for each module)
- too high temperature of the thyristor stacks measured by thermostat
- too high currents in the crowbar assembly detected by measuring the voltage across the dump resistor
- DC overvoltages (crowbar triggered), detected by the presence of current through the crowbar assembly
- earth leakage current in the neutral connection (mid-point resistor to earth)
- loss of various auxiliary power supplies, cooling water or synchronising voltage
- failure to complete the transition to BLOCK MODE

The protection actions, have been classified in three different levels:

• ACTION LEVEL 3 causing an immediate transition to FREEWHEEL MODE and a tripping of the main High Voltage Circuit Breaker (HVCB) feeding the amplifier as well as a stop of the JET pulse

• ACTION LEVEL 2 causing an immediate transition to FREEWHEEL MODE without tripping the HVCB as well as a stop of the JET pulse

• ACTION LEVEL 1 rising only an INHIBIT action of the next JET pulse until the alarm is cleared.

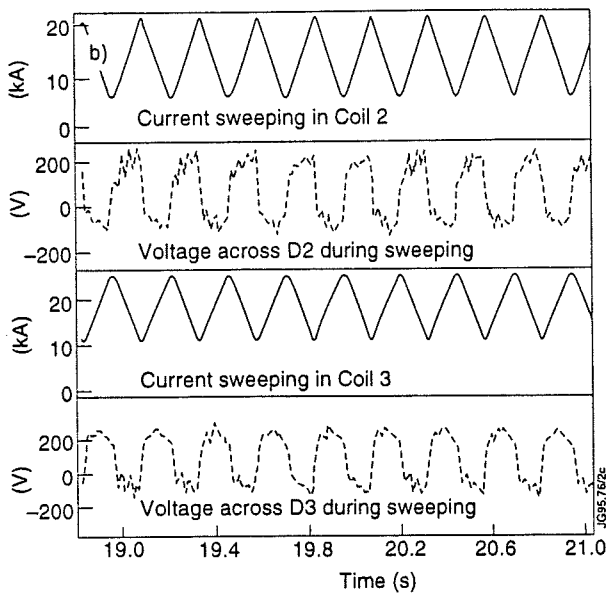

Fig. 6:

XI. CONSEQUENCES OF DISRUPTIONS

Because the Divertor coils are inside the vessel, there is a strong magnetic coupling with the plasma. Vertical instabilities characterised by fast vertical movement and fast current quench produce overvoltages which often reach the triggering level of the PDFA crowbars.

Initially, the PDFAx have been designed to supply currents to the Divertor coils in the same direction as the plasma current. The induced negative currents through the positive crowbar could only be of short duration, around 20ms, since in that case they could only be produced by the plasma fast downward displacements .

In a new experimental scenario, the connection of the coils D1 and D4 has been inverted. Negative induced currents through the positive crowbar are not anymore of short duration but in the worst case (upward vertical instabilities) may decay with the natural time constants of the coils, namely several seconds (fig. 7).

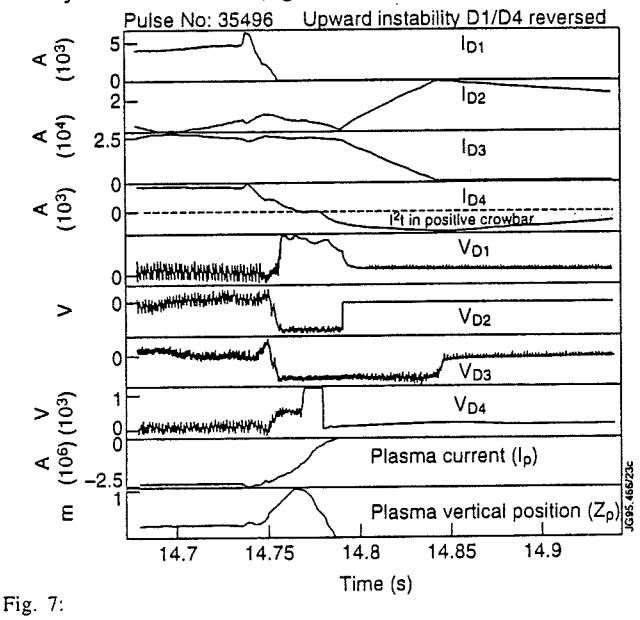

Fig. 7:

In order to assess the risk associated to higher I^2t in the positive crowbar assembly (thyristor and dump resistor) prior to operation campaigns with D1 and D4 inverted, a study based on simulations with MATLAB and ATP has been carried out. In the worst scenario of vertical disruption, defined by a plasma current of 5MA, an upward vertical displacement of 1m and an initial current equal to zero in coils P1 and P4, an energy estimated to 1265kJ is dumped in the crowbar resistor (its maximum energy capability being of 2920kJ).

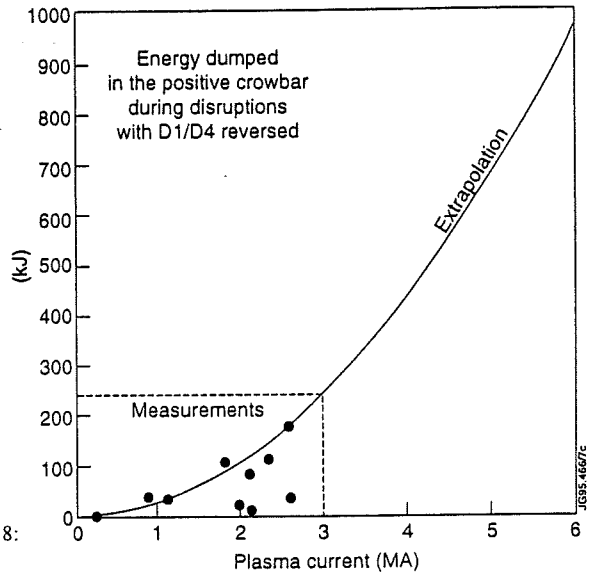

Fig. 8:

The temperatures reached by the crowbar components were respectively estimated to 85°C for the thyristor junctions (absolute maximum limit taken as 200°C when no voltage is reapplied) and 163°C for the dump resistor (absolute limit taken as 250°C for hot spot).

Following these detailed assessments, an experimental campaign with reverse currents in coils D1 and D4 took place in April, May 1995. The actual current peaks and energies (fig 8) dumped in the crowbar resistors have been measured. The results, show that the actual induced currents and energies are, as expected, lower that the ones found in the worst simulated scenario (fig. 8)

XII. CONCLUSION

After a two year period dedicated to the design, manufacturing, and test on dummy load up to the full ratings, PDFAx have been connected to the Divertor coils since the beginning of 1994. Operation of the bipolar crowbar assemblies during plasma instabilities and disruptions have given entire satisfaction. Results recorded so far indicate that the induced currents are within the design values.

REFERENCES

[1] E. Bertolini and the JET Team, "JET with a pump divertor: design, construction, commissioning and first operation" *JET-P(94)56*

[2] M. Garribba, et Al, "The new Control Scheme for the JET Plasma Position and Current control System", SOFE 93

[3] V. Marchese,et Al, "Detailed Design, installation and testing of the new Coil Protection System for JET", SOFT 94.

VI. CONTROL OF THE AMPLIFIER

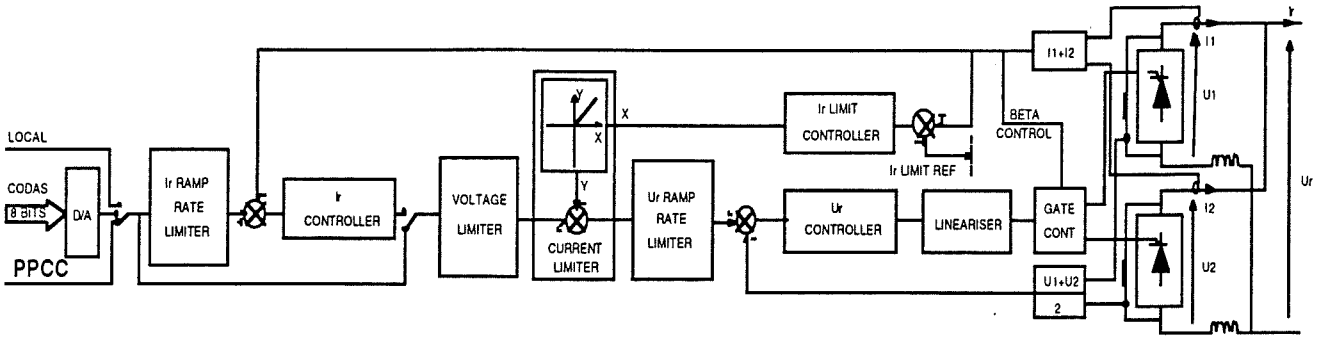

Fig: 4:

The gate pulse phase shift, namely α is varied between the 5° electrical and a avariable (β control) maximum limit depending on the rectifier current. The maximum inversion limit has been chosen as 140° electrical when the output current is nil. When the output current is at its maximum, namely 20kA in each module, the β control gain has been chosen so that the inversion limit is reduced proportionally to the current to 106° electrical.

The amplifier can be controlled in two different ways (inside a range determined by adjustable voltage and current limits):

- VOLTAGE CONTROL (mode used during JET operation, PDFAx behaves as a voltage amplifier)
- CURRENT CONTROL (mode used only during commissioning).

VII. DUMMY LOAD COMMISSIONING

Extensive commissioning has been carried out on dummy load (9.1mH 4.1mΩ) and each PDFAx has been tested up to its full ratings, output current and voltage, overvoltages (crowbar triggering) duty cycle (one pulse every 600s) and current sweeping capability.

As type test, a short circuit test has been carried out at maximum α, 5° electrical, to demonstrate the effectiveness of the PDFAx internal protective action (maximum current peak reached: 90.3kA after 8ms)

VIII. RATINGS

Table I

MAIN CHARACTERISTICS	PDFA 1	PDFA 2	PDFA 3	PDFA 4
Nominal duty cycle	20s/580s	20s/580s	20s/580s	20s/580s
Nominal AC supply voltage U_n	36kV	36kV	36kV	36kV
Nominal output current In	40kA	40kA	40kA	40kA
Continuous current rating	8kA	8kA	8kA	8kA
2 tap transformer	no	yes	yes	no
No load voltage at Un (tap 1)	910V	1180V	1180V	910V
No load voltage at Un (tap 1)	/	930V	930V	/
Minimum output voltage at Un (tap 1)	500V	650V	650V	500V
Minimum output voltage at Un (tap 1)	/	500V	500V	/
Maximum blocking capability	1500V	1800V	1800V	1500V
Frequency bandwidth in voltage control	200Hz	200Hz	200Hz	200Hz

JG95.146/12c

IX. COMMISSIONING ON THE DIVERTOR COILS

The current has been risen progressively in each divertor coils and the magnetic coupling between the Divertor coils themselves and the other poloidal coils (mainly P1 and P4) have been checked in turn. The current limit loop has been optimised and the initial overshoot due magnetic coupling between coils and the vessel has been reduced to an acceptable value of 10%

X. OPERATION EXPERIENCE

The first experimental campaign has revealed that because there was no full intertripping between the 4 PDFAx, the current in one coil could rise dangerously (in terms of forces allowed in the coil system) due to flux conservation when the current in an adjacent coil is forced to decay, for instance if the amplifier reference requests a full inversion. This intertripping has now been implemented via the Coil Protection System (CPS) [3].

An example of current sweeping patern at a frequency of 4Hz (the range 0.5 to 2Hz being forbidden to avoid mains resonance) is shown on figures 5 and 6 for a 3MA plasma discharge.

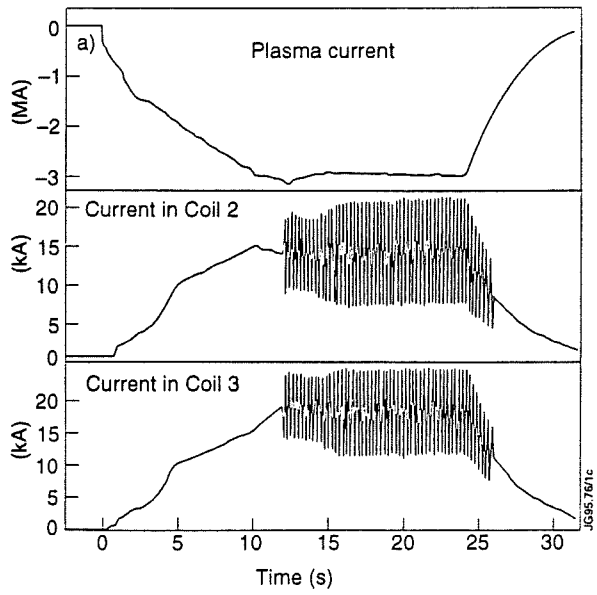

Fig. 5:

The Use of Carbon Fibre Composites in Divertor Target Plate Tiles and Structures

H. Altmann, E. Deksnis, J. Fanthome, C. Froger, C. Lowry, A. Peacock, M. A.Pick
JET Joint Undertaking, Abingdon, Oxon OX14 3EA, UK

ABSTRACT

Carbon-Carbon fibre composite (CFC), in the form of target plate tiles, is a standard material for intercepting conducted power in divertors. Its good thermal conductivity and ability to withstand high temperatures without melting give it an advantage over other materials for plasma facing components. Supporting structures are generally made from stainless steels or Inconels. In a radiating divertor, designed to operate with detached plasmas, heat is deposited by radiation on to both plasma facing components and supporting structures. Consequently CFC has been chosen as a structural material to overcome the limitations of metal structures. The various material properties such as thermal conductivity, strength, rigidity and anisotropic behaviour need to be taken into account for the design. Tests have been carried out on a range of CFC materials from different manufacturers to determine these properties. Thermal behaviour has been studied through power load tests in the JET Neutral Beam Test Bed. Structural properties have been measured through mechanical tests on prototype assemblies. Clamping and joining methods have been developed for the assembly of CFC plates to form structurally and thermally robust tile carriers for a radiating divertor.

INTRODUCTION

The selection of CFC material for use in a divertor depends upon a number of factors such as working environment, component application, mechanical stresses, thermal stresses and material properties. CFC has become a standard material for intercepting conducted power on to target plate tiles owing to its good thermal conductivity and shock resistance, low atomic mass and ability to withstand high temperatures without melting. The next design of the JET divertor is expected to operate with radiating plasmas which will subject the supporting structure to radiated powers up to $2MW/m^2$. This level can lead to buckling and distortion in conventional metallic structures so consequently CFC material will be used for the supporting structure as well as for the plasma facing tiles.

INPUT PARAMETERS

The following parameters are assumed for purposes of assessing the performance of CFC material:

A. Conducted power on tiles $\leq$ 20MW/m2.
B. Conducted power on structure <6MW/m2
C. Radiated power $\leq$ 2MW/m2.
D. Max. allowable stress = 0.6 x minimum guaranteed failure value (table 1). Design factor $\approx$5.
E. Maximum allowable temperature $\leq$ 1500°C.

MATERIAL PROPERTIES

Manufacturers of CFCs tend to use in-house techniques for the production of their material and consequently a fairly wide range of properties is found between the different brands. The basic production technique consists of building up the material to the required thickness with woven carbon fibre sheets. This leads to 2-dimensional (2D) material but fibres can be introduced through the thickness of the sheet by dragging some fibres perpendicular to the layers by means of a "needling" process to produce 3D or quasi-3D material. Fullscale weaving through the layers is also possible. The next stage is to fill the voids between the fibres with carbon, either by pitch or resin impregnation or chemical vapour deposition (CVD). This results in a structure with low thermal conductivity but good strength. The thermal conductivity is enhanced by high temperature (>2000°C) graphitization in a furnace but with some loss of mechanical strength. These processes vary in detail between different manufacturers

The non-isotropic nature of CFC affects the material properties in the following way:

- Material strength depends upon the loading direction with the maximum strength along the fibre direction.
- Thermal conductivity depends upon the fibre direction, being highest along the fibres and lower across the fibres.
- Thermal expansion is dependent on the fibre distribution, being lower along the fibres and highest across the fibres.
- Bowing caused by thermal gradients under surface heating is dominated by thermal expansion with some contribution from thermal conductivity such that the bowing is maximum across and minimum along the fibre direction.
- Density variations are an unavoidable consequence of the carbon impregnation process and can affect strongly the thermal conductivity.
- Graphitization of the carbon improves the thermal conductivity but decreases the mechanical strength.

For any particular product there will be variations in properties owing to variations in the process conditions. Manufacturers are able to predict these properties reasonably accurately and consequently will guarantee minimum values Any design should be based on these minimum values.

MATERIAL SELECTION

The following requirements and considerations are relevant in the selection of materials for both tiles and structure:

Table 1: Thermal and Mechanical Properties of Some Carbon Fibre Composites Considered by JET for Fusion Applications

n/a means data not available or not asked for by JET.

		SEP N11	SEP N11-2	SEP A11	DMS 728	DMS 712	SGL 1502 ZV22	SGL 1002 ZV22	Le Carb Lorr A035
Tensile strength x (MPa)	Typ	40	40	75	70	70	n/a	n/a	n/a
Room Temp	G min	34	35	n/a	n/a	n/a	n/a	n/a	n/a
Flexural Strength (MPa)	Typ	80	80	150	105	105	200	80	n/a
Room Temp	G min	48	70	n/a	85	85	150	70	60
Interlaminar shear strength (MPa)	Typ	18	20	30	13	10	8	8	n/a
Room Temp	G min	14	15	n/a	10	7	7	7	n/a
Ther. Exp. Coeff x, y/z (10^{-6})	Typ	2/2	2/2	<2	0/10	0/12	-0.5/12	-0.5/7	1.0/1.5
RT to 300°C	G max	3/3	3/3	n/a	0.5/12	1/15	-0.7/15	-0.7/10	2.0/3
Thermal conductivity x, y/z	Typ	120/90	55/40	18/12	150/160	210/60	190/22	125/30	170/n/a
($Wm^{-1}.k^{-1}$) 300°C	G min	105/80	50/35	n/a	110/145	140/40	170/20	115/25	150/145
Youngs modulus x, y/z (GPa)	Typ	20/15	16/12	25/12	30/30	30	120/n/a	28/n/a	n/a
Room Temp	G min	n/a	n/a	n/a	n/a	n/a	90/n/a	25/n/a	n/a
Elec. Res. x, y/z μΩm	Typ	6/10	17/25	n/a	n/a	4/13	4/n/a	25/n/a	n/a
Room Temp	G min	n/a	n/a	n/a	n/a	n/a	n/a	7	n/a
Type		Needled	Needled	Quasi 3D	2D	2D	2D	2D	Quasi -3D

- Specific gravity >1.6 to minimise both deuterium absorption and outgassing as well as to maximise the strength and thermal conductivity.
- Full graphitization of the impregnated carbon at temperatures >2000°C to minimise the deuterium absorption and outgassing while increasing the thermal conductivity. The decrease in strength as graphitization proceeds is unavoidable.
- Differences in thermal conductivity and strength along the three axes will influence the way both mechanical and thermal loads can be applied to the material. Table 1 gives manufacturers' minimum guaranteed values and the average values for some of the materials tested at JET. A point worth noting is the link between high thermal conductivity in the fibre directions for the 2D materials and the lower thermal conductivity and lower strength perpendicular to the fibre direction. In the case of the 3D or quasi-3D materials, the increase in strength and thermal conductivity along the third axis leads, in general, to a consequent reduction in these properties along the other axes. The consequence of this is that the 2D materials would be the natural choice where high thermal conductivity is essential and that 3D materials are more suitable for structural applications where mechanical loads appear on all axes. One of the main challenges when working with 2D materials is ensuring that mechanical stresses in the cross-fibre direction do not exceed the relatively low allowable values.
- Resistance to thermal shock, especially in tile material, is essential. Experimental studies at JET on a range of CFC materials [1] have shown that these materials can withstand much higher flux levels than expected, based upon finite element analysis using mechanical data. Information in this area is limited and tends to be classified in military areas.
- Bowing of CFC material under non-uniform heating is mainly a function of the expansion coefficients. Two-dimensional material has significant differences between the bowing in the directions along and across the fibres. This can affect strongly the choice of fibre direction for tile applications. If, for example, conducted power is intercepted at a very shallow angle, say <2°, than a large bowing effect will increase the interception angle over the front half and decrease it over the rear half of the tile. In this case the preferred fibre direction would be in the direction of the incoming power to minimise the bowing effect. For large interception angles, the bowing effect becomes negligible.
- Impurity levels in the CFC need to be kept as low as possible to avoid contamination of the plasma.
- Electrical conductivity is a factor in the generation of electro-magnetic forces on tiles and structures but generally is of secondary importance in material selection compared to other properties such as thermal conductivity and strength. The highest forces on divertor tiles and structures come from halo currents [2] reacting with the poloidal and toroidal magnetic fields.

These considerations of material properties and expected thermal and mechanical loads on the next JET Divertor design have led to the choice of Dunlop DMS 712 (2D) material for the tiles and Sepcarb N11 and N11-2 (3D) material for the carriers. The fibre direction in the tiles will be into the thickness for good thermal conductivity and either poloidal or toroidal, depending upon the requirement for low thermal expansion and bowing. The uniformly distributed strength of Sepcarb N11-2 makes it suitable for carrier construction but the greater thermal conductivity, despite the lower strength, of N11 dictated its use in areas of high radiated or conducted power. A typical application is a protection rib shown in figure 1 where it can intercept conducted power up to $6MW/m^2$ for 10 seconds. The corresponding temperature contours at the end of such a pulse have been computed with ABAQUS and are shown in figure 2. The maximum surface temperature is ≈1100°C.

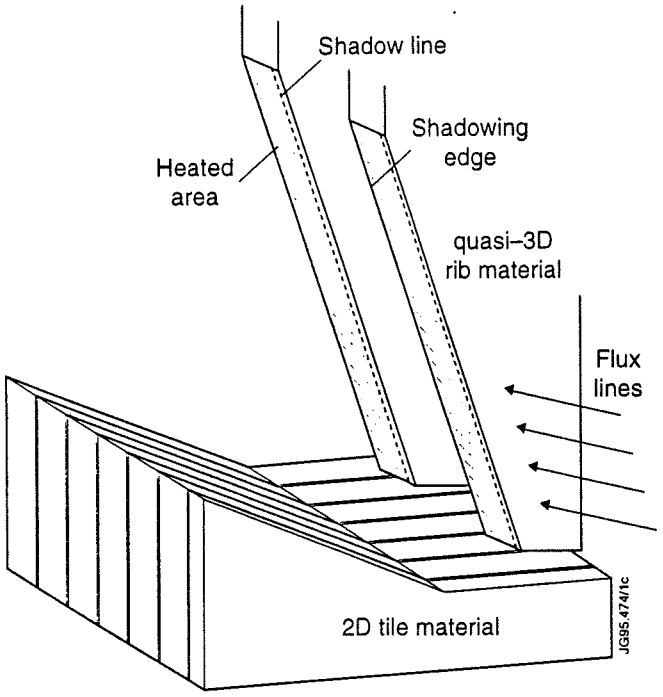

Fig.1: Carrier protection ribs.

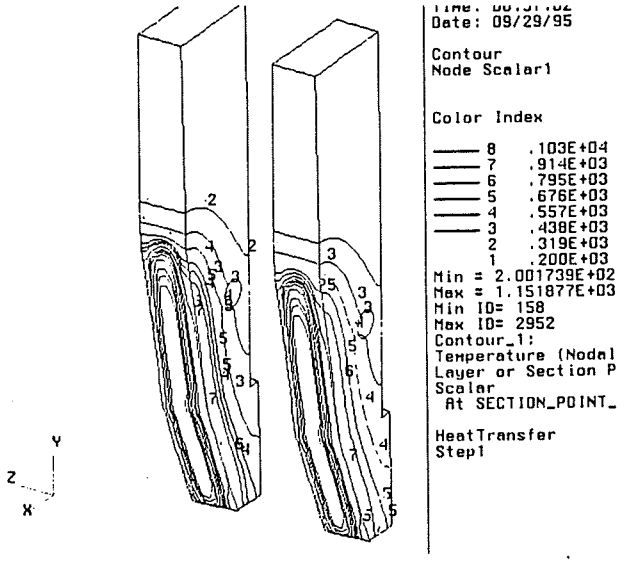

Fig.2: Temperature contours on protection ribs

FIXING AND JOINING TECHNIQUES

The most common technique for attaching tiles inside the JET torus has been through a single central screw fitting. A threaded metal insert is screwed into the rear of the tile and pinned against rotation. This system is suitable only for 3D material or 2D materials with the thread axis perpendicular to the fibre plane if a large bending moment is applied during clamping. The tile attachment, shown in fig. 3, was tested in 2D material with the thread axis parallel to one fibre direction. The tile was supported at each corner and pulled down at the centre. The combination of bending moment and hoop stress across the thread led to inter-laminar splitting of the tile at a load on the insert of 6.4KN. A tile fixing method was developed that would not apply a bending moment across the fibres. Figure 4 shows the chosen dumbbell system which moves the load points to the outside of the tile, in line with the corner contact pads. The bending moment is applied in the strong fibre plane and removed from the cross-fibre direction. Additional tie-rods in tension across the fibres maintain the geometric integrity in the case of thermally induced cracks.

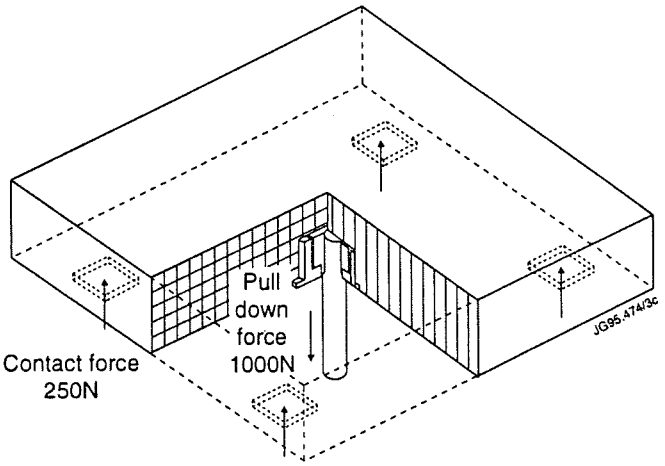

Fig.3: Central tile fixing.

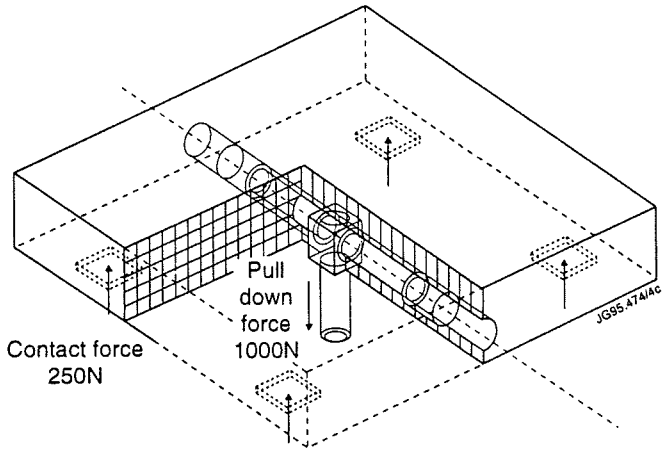

Fig.4: Dumbbell tile fixing.

Construction of a carrier requires a different joining technique. Tapping threads directly into CFC is feasible but the fibrous, anisotropic nature of the material leads to chipping of the threads. Consequently a barrel nut and bolt system, as shown in figure 5 has been tried successfully. In general an M6 bolt is made from Nimonic 80A and a barrel nut from aluminium-bronze, torqued to 10Nm, to produce a non-seizing combination. Certain areas under high thermal load can reach temperatures above the safe value for al-bronze and alternative materials such as Inconel and CFC are being tested.

THERMAL AND MECHANICAL TESTING

Tile material from 4 European manufacturers was subjected to high power load testing in the JET Neutral Beam Test Bed [1]. The 2-D materials developed cracks in the fibre planes at temperatures in excess of 2000°C but this did not affect the tile performance with the tie-rods maintaining the tile geometry. The 3-D materials remained crack-free but were not tested to the same level as the 2D material. Mechanical testing of the dumbbell fixing system was carried out to

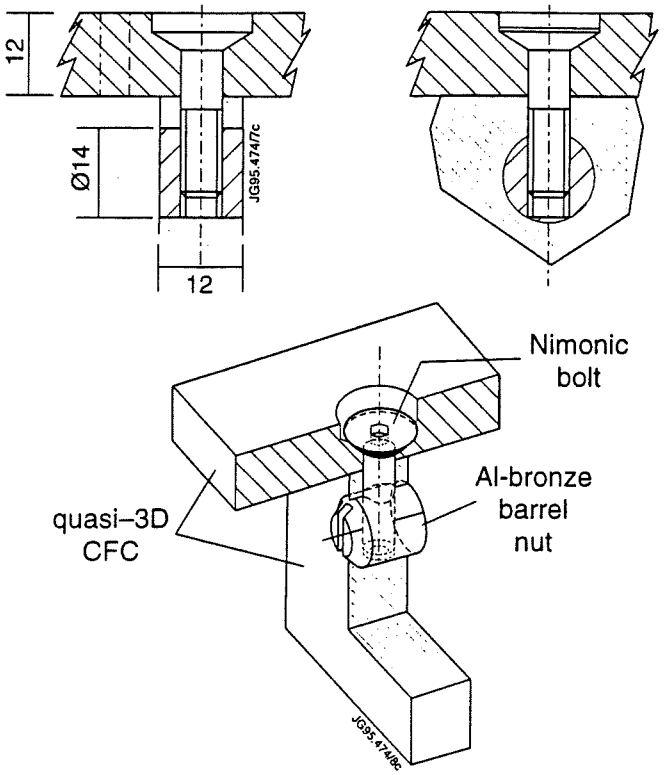

Fig.5: Barrel nut and bolt fixing.

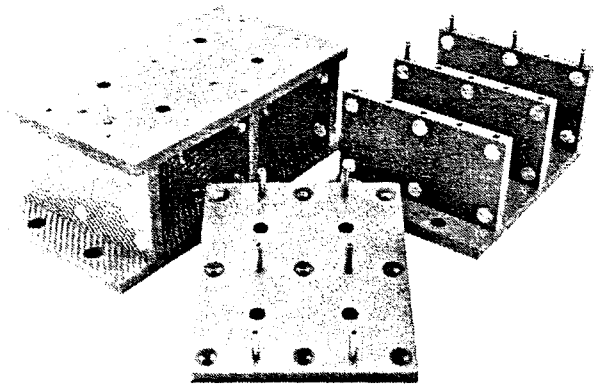

Fig.6: Prototype model structure.

check the tile behaviour under halo current loads. At a load of 13.7kN the dumbbell deformed plastically but the tile remained intact. Mechanical testing of a prototype model structure from Sepcarb A11 was carried out to study the behaviour of the barrel nut bolting system under bending and tensile loads. Figure 6 shows the model in component and assembled form. The first bending test applied equal and opposite forces to the upper and lower plates to induce an S-bend in the vertical ribs. The second bending test applied a bending moment about the lower barrel nut joints. Figure 7 shows the load/deflection curves for the two cases. An approximately linear behaviour is seen up to forces of 6KN and 3KN respectively, estimated to be about 7 times greater than for the worst-case disruption. A third test to failure checked the pull-out force for a barrel nut in a 12mm CFC plate. The result is shown in figure 8. The material failed in tension across the minimum section above the insert.

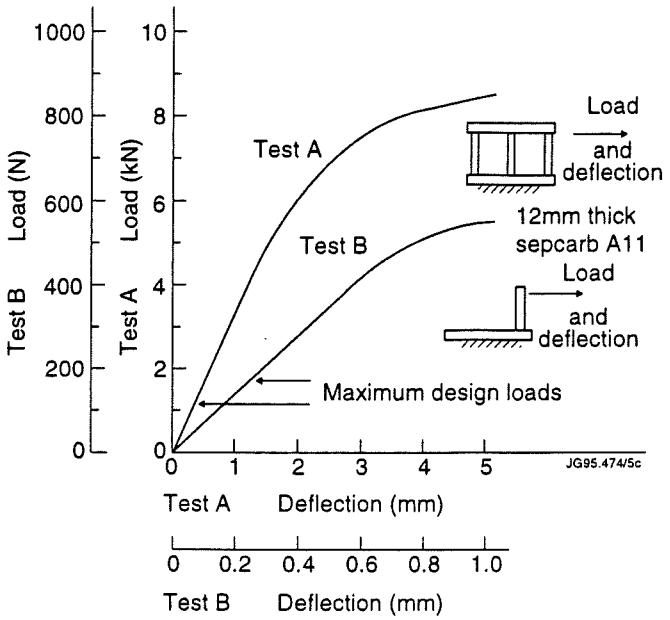

Fig.7: Bending test on bolted assemblies.

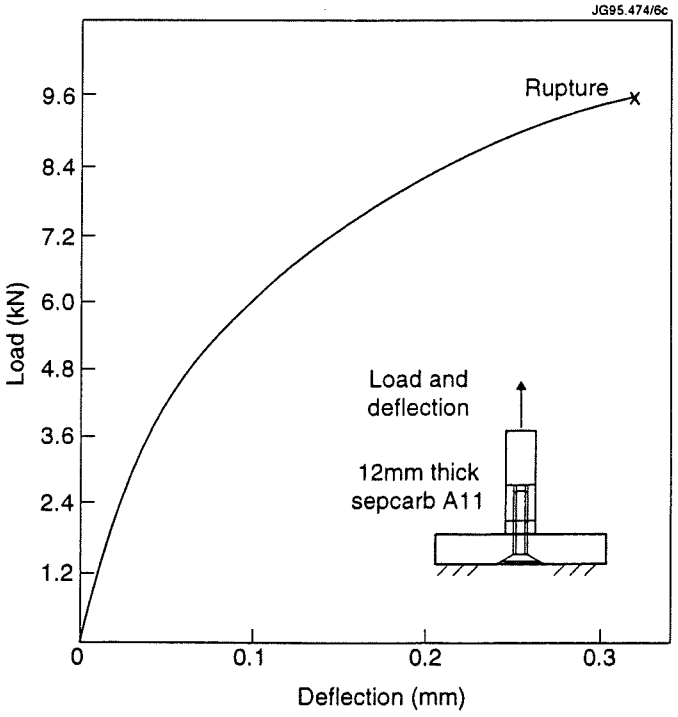

Fig.8: Pull-out test on barrel nut/bolt fixing.

REFERENCES

[1] M.A.Pick et al, "Large carbon fibre reinforced carbon tiles for a Mark II divertor in JET", Journal of Nuclear Materials 220-222 (1995) 595-600.

[2] M.A.Pick, P. Noll, P. Barabaschi, F.D. Marcus, L. Rossi, "Evidence of halo currents in JET", 14th SOFE, San Diego 1991, pp. 187-190.

ICRF SYSTEM IN THE JET PUMPED DIVERTOR CONFIGURATION

A. S. Kaye, V. Bhatnagar, M. Bures, P. Crawley, B. Fechner, C. Gormezano, J. Jacquinot, P. Lamalle, R. Lobel, J. Plancoulaine, E. Righi, F. Rimini, M. Schmid, A. Sibley, A.C.C. Sips, D. Start, M. Timms, B. Tubbing, T. Wade, R. Walton

JET Joint Undertaking, Abingdon, Oxon OX14 3EA, U.K.

ABSTRACT

After one year of operation the new A2 ICRF system installed for the pumped divertor phase of JET has achieved a coupled power of 16 MW, a coupled energy of 70 MJ, and combined heating with NB of 32 MW, each in ITER relevant high density, highly radiating, ELMy H-mode plasmas.

The generators and antenna system now operates over 30 kV, with rapid, on-line matching and phase control of four coupled current straps. The coupling to the plasma and heating efficiency are phase dependent - coupling improves but heating efficiency falls with decreasing k//; good heating in monopole phasing has been observed after installation of a new separator between the set of antennae in one of the modules. Cross-coupling between straps enhances the imbalance in plasma coupling of the inner and outer straps of the array due to a mismatch in the feed lines. Modifications to reduce this imbalance and improve low k// operation are described

The A2 array is similar in size to one row of the current ITER in-port antenna design. The implications for such a design are discussed.

I. INTRODUCTION.

A new set of eight 'A2' antennae was installed in JET in 1993 to match the new plasma configuration. These antennae are arranged in four arrays each having four current straps at nearly constant pitch in order to control the launched spectrum. At the same time, substantial modifications were made to the RF generator control system to enhance the matching and phase control to take account of the cross-coupling in the four strap array, and to improve the immunity to cross-talk between arrays. This system has been in operation on the torus during the pumped divertor campaign. This paper describes the technical performance achieved on the system during this campaign, the results of inspection after removal from the torus, the enhancements now being incorporated, and the implications for an RF system on ITER.

II. DESCRIPTION OF THE A2 RF SYSTEM

The A2 antennae have been previously described in detail [1] - a number of features which have turned out to be important are outlined here. The pumped divertor configuration of JET required a plasma profile displaced inwards from the A1 antenna by 2-300 mm. A new set of antennae was designed to match to this new configuration. At the same time, the eight antennae were re-arranged into four arrays each with four current straps at nearly equal pitch. This configuration enables the spectrum to be well defined over a wide range, from monopole to $7m^{-1}$ in dipole (180 degree between adjacent straps). This configuration is not without penalty. We now have four coupled current straps, which both complicates the matching system and modifies the coupling resistance on each strap. In addition, the antennae are no longer symmetrical about the transmission line ports, necessitating the use of a cross-over line inside the antenna from the transmission line to the inner current straps. Furthermore, the inner and outer straps are of somewhat different design, and therefore RF characteristics.

The antennae project up to 1m from the vacuum vessel and the plasma is highly elongated. Resilience to disruptions strongly influenced the design of the antennae, with a strict limit imposed on the forces to be transmitted to the torus wall. Each antenna is a thinwall flexible structure supported by the torus wall via 10 or 11 articulated arms on each side of the antenna. These arms are connected to the antenna via capacitors formed by plasma spraying alumina onto inconel plates. Each articulated joint is electrically isolated and bridged by a flexible earth strap. There is a gap between the back wall of the antenna and the torus wall increasing from typically 90 mm at the top to 200 mm at the bottom.

RF image currents in the sidewalls and septum of the antenna degrade the enhanced spectrum of the four strap array, in particular, in phased operation. Both are therefore slotted radially to a depth of typically 100mm.

The voltage on the A1 antenna was limited by arcing on the conical ceramic support for the current straps. The A2 antenna does not have this support. The current straps are thin wall fabrications of large cross-section to support the bending stresses with minimum eddy currents, and a DC break is included in the transmission lines feeding the inner straps; this allows all in-vessel ceramic supports to be removed.

The protection of the antenna from the plasma is provided by poloidal limiters on each side of each four strap array, and by CFC tiles mounted on rails above and below the array. The limiter tiles are 17 mm, and the top and bottom tiles 7mm, in front of the magnetic surface tangential to the screens. The top and bottom rails are supported by the limiter structure. The joint to the left limiter is electrically closed, whilst that to the right limiter is electrically isolated via a ceramic coated pin. The limiters are electrically connected to the torus via laminated current straps at the mid point and either end. All of this limiter structure is electrically and mechanically independent of the antenna. RF currents can flow from limiter to antenna only via the torus wall and the current straps on the support arms, or stray capacitance. The limiter structure has

dimensions c. 2m high x 2m toroidally, which is typically one quarter to one half wavelength over the frequency range of the system.

The generator control system for the A2 antenna was extensively modified to take account of the additional complexity of matching and phase control on the four coupled straps of each array, and also to incorporate improvements arising from A1 experience [2]. The changes include:

- larger, faster trombones in each line;
- conjugate coupling networks, comprising 3dB couplers with appropriate termination, linking the outer straps on each array, compensating for the effects of cross-coupling in current drive (90 degree) phasing;
- digital, automatic matching system for each four strap coupled array, including control of stubs, trombones and phase on each line, and frequency for each array;
- digital measurement and control of the amplitude and phase, and linked protection systems;
- narrow band filtering within the matching system to allow discrimination against cross-coupling between arrays;
- ELM alleviation by increasing the reflected power trip threshold during an ELM, and by restoring the power without a ramp after an ELM induced trip.

With the exception of the conjugate coupling network, these systems have been progressively brought to full performance over the operating campaign.

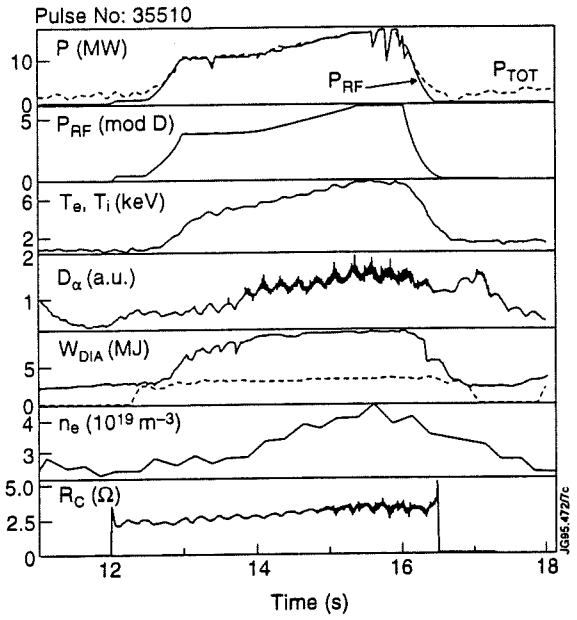

Fig.1 JET pulse with 16MW coupled RF power

III. TECHNICAL PERFORMANCE OF THE A2 SYSTEM

A. Coupled power

The A2 system has coupled up to 16 MW to the plasma, limited by the high voltage required to couple full power at typical coupling resistance - this pulse is summarised in fig 1. In combination with neutral beam, up to 32 MW of combined heating has been achieved; 70 MJ has been coupled in a single pulse; RF only H-modes have routinely been produced at 5MA; the H-mode threshold is somewhat less with RF than NB in some cases. Many of these results have been obtained in ITER relevant highly radiating ELMy H-modes. These results have been described elsewhere [3].

B. Voltage Limits

The voltage limits in dipole increased during the campaign from 20 kV to an average of 28 kV across all straps, and 34 kV on one array. Much of this improvement has arisen from electronic developments, in particular elimination of sidebands on the primary oscillators which led to generator instability. The voltage limit is now found to improve with high voltage conditioning of the antenna, and to degrade after disruptions and giant ELMs. Inspection of the antenna and vacuum lines after recent removal from the torus shows sign of tenuous arcing in one of the antenna housings, some modest but systematic arcing within the antenna support structure, and in general little sign of arcing in the vacuum transmission lines. One window has been heavily metallised and failed on the inner ceramic apparently following an instability in the generator. The pressurised side of the windows often show tenuous arc tracks. There is no obvious limitation in the antenna, which may enable further modest improvements with the elimination of arcs and associated gas release in the support structure. It is noted that the present performance is an improvement on the A1 antennae, and reflects the elimination of the ceramic supports.

C. Coupling Resistance

The coupling resistance measured on A2 is less than anticipated [1], in particular at larger gap between the antenna and plasma. This is shown in fig 2,

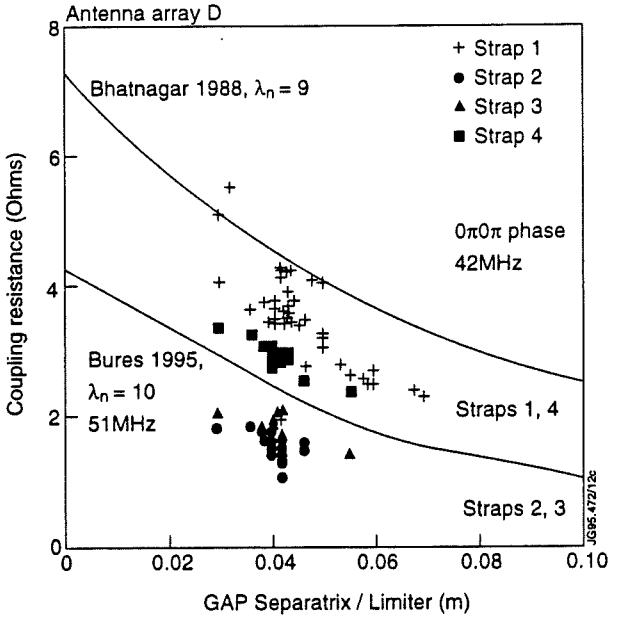

Fig.2 Comparison of measured and computed coupling resistance v. distance of plasma from the antenna

which compares predicted and measured coupling resistance in dipole phasing as the gap to the separatrix is varied. A refined model [4] gives improved agreement with observation, as also shown in fig 2. This model differs primarily in the detail of the modelling of the antenna itself - the plasma model has minor changes, for example in the density profiles, but provides similar data to the antenna model. The antenna is represented as a series of striplines, which can be chosen to give satisfactory agreement with observation. Numerical simulation of experimental data at TFTR has shown a three-dimensional antenna model to be required to reproduce measured coupling resistance using measured density profiles [5]. It is clear that improved coupling prediction codes, and in particular validation of these codes are required, and this is under way.

The average coupling of the inner and outer straps is weakly dependent on frequency, with a broad maximum around 42 MHz, close to the design objective. However, the inner straps are often found to have much less coupling than the outer straps. This imbalance depends on frequency, as illustrated in fig 3, which shows the coupling resistance in dipole measured with varying frequency on a series of nominally identical plasmas.

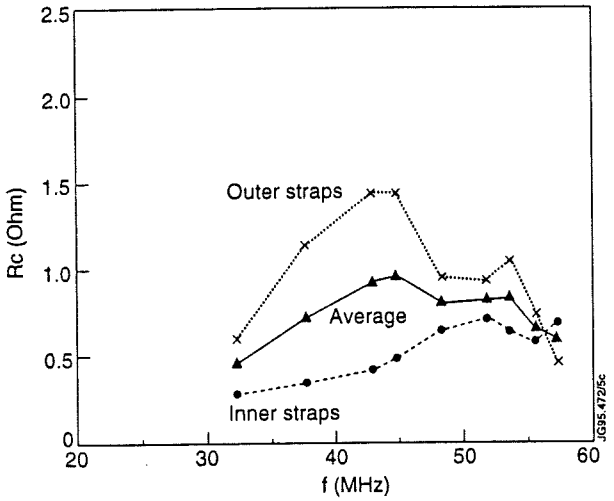

Fig.3. Frequency dependency of measured coupling resistance on plasma of inner and outer straps and average coupling.

The inner straps show much lower coupling than the outer straps at low frequency, increase to equal the outer straps at about 52 MHz, and exceed the outer straps at 56 MHz. This frequency dependence is now well established over many measurements. In monopole, the coupling is higher on all straps, and the imbalance reduced.

Table 1
The scattering matrix of a four strap array measured on plasma at 51 MHz

$\|S_{ij}\|$				arg S_{ij}			
0.831	0.062	0.049	0.053	-113	81	54	56
0.062	0.842	0.050	0.050	81	-121	58	58
0.049	0.050	0.815	0.084	54	58	-139	72
0.053	0.050	0.084	0.798	56	58	72	-110

The cause of this imbalance has been investigated using both measurements on the torus and on the prototype antenna. Scattering matrix measurements on the (two strap) prototype antenna using a lossy foam (Echosorb) as a load have been found to reproduce the basic features of the torus observations. Typical matrix elements are shown in fig 4. The coupling resistance calculated from such measurements is illustrated in fig 5. Whilst this is a powerful technique which allows assessment on the test bed of modifications to the antenna the

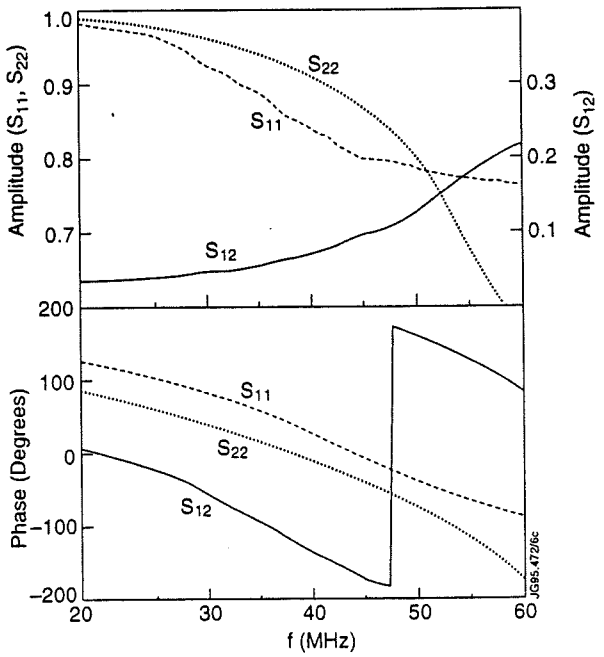

Fig.4 Scattering matrix measured with foam loading of the prototype antenna

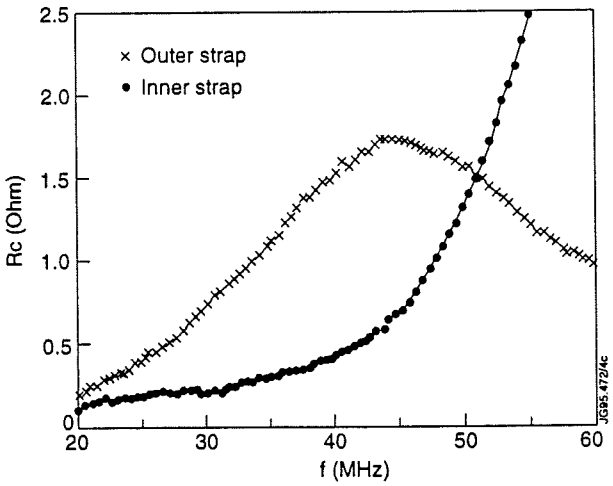

Fig. 5 Coupling resistance in dipole calculated from foam loaded scattering matrix.

foam does not fully represent the plasma. In particular, the dielectric constant of the foam is much less and the frequency dependence of the loss different, and the data consequently needs to be treated with caution.

The scattering matrix of the four strap antenna array has also been measured using foam loading both before installation and in the torus. A method has been developed [6] which allows the measurement of the four strap scattering matrix on plasma in a single pulse. A typical result is given in Table 1. Again, this should be treated with caution as the phase data is critical, and subject to significant error. The large values of S_{13} and S_{14} are noted. These have been found to be necessary to reproduce the monopole data. The large phase angle of S_{12} relative to S_{11} is also noted. This reduces the coupling resistance in dipole and enhances monopole.

An important part of the imbalance arises from a mismatch between the crossover strap to the inner conductors and the 30 ohm lines/current straps on either side. The crossover strap appears as a 70 ohm line, 430 mm long with a phase velocity of 0.95. A simple model representing the antenna as a length of 70 ohm line in series with a 30 ohm short circuited line reproduces the frequency dependence of the antenna current as shown in fig 6.

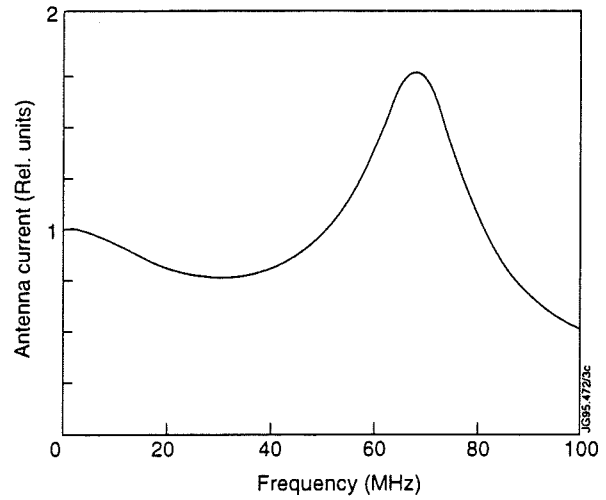

Fig 6. Calculated effect of mismatched line on current in the antenna

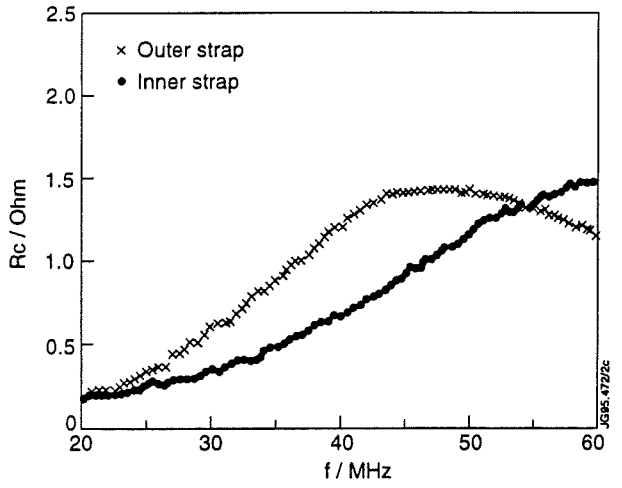

Fig.7 The coupling resistance in dipole of a two strap array with modified crossover, from foam measurements

The effect of reducing the impedance of this crossover line has been calculated taking the measured resonant frequency on the inner and outer straps of 47/41 MHz respectively. The impedance of the crossover line on the prototype antenna has been reduced to about 35 ohms by an increase in capacitance to the back wall. The measured scattering matrix agrees well with that calculated. The corresponding coupling resistance is shown in fig 7. The imbalance is much reduced although still present. More importantly, it is found that the cross coupling between straps is such that the outer strap coupling decreases as the inner improves, with the average coupling remaining essentially unchanged.

D. Heating efficiency and impurities

The heating efficiency of the A2 antenna has been found to be sensitive to phase. As the k// is reduced, the heating efficiency decreases as shown in fig 8, until in monopole phase, negligible heating is observed. This is in contrast to A1, which showed a heating efficiency largely independent of phase [7,8].

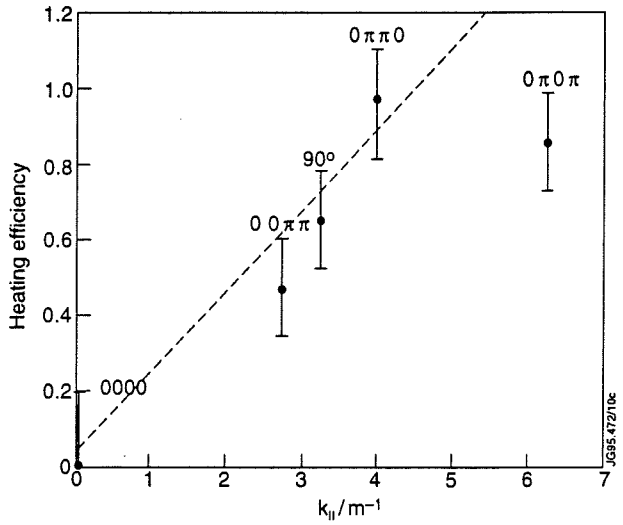

Fig.8 Measured heating efficiency dependence on k// (without separator)

When operating at low k//, particularly in monopole, visible glows are observed on the one poloidal limiter in line of sight of the viewing system. These glows are diffuse areas typically 0.2 m in extent along the limiters. Usually, just one is seen near the top of the antenna, but occasionally two appear. The position of this glow depends on the helicity at the boundary in a manner which indicates the source to be near the radial section of the left hand current strap viewed from the plasma. The glow is short lived (<10 millisec) at the end of the pulse, indicating that it is not thermal radiation from hot tiles and thus not representing significant power loss. At high power, the pulse length in monopole is limited by an influx of carbon leading to a disruption.

Inspection in vessel showed no damage to the limiters, and only slight melting of a few of the knuckles holding the ends of the screen elements at the top of the antennae. Significant surface melting was observed on the top and bottom tile supports, and tenuous arcing had damaged the electrical breaks isolating the right hand end of the rail from the limiter. This indicates substantial interaction between the antenna and the top rails, and kilovolt RF voltages appearing on the insulators. It is noted that the capacitance of this break is close to resonance with the inductance of the rail in the frequency range of interest.

The toroidal separation between limiters is about 2.2 m, compared to 0.9m on the A1 antenna. The radial clearance between the limiters and screen has been increased to 17mm on A2 from 11mm on A1 in proportion to the square root of the connection length, to give similar density at the screen. However, with the increased separation, this density is very sensitive to the poloidal curvature of the separatrix at the antenna. Plasmas with tight curvature, as routinely obtained on high beta plasmas for example, can penetrate close to the screen, both increasing the density at the screen and establishing flux lines linking the screen to the limiters which are prone to sheath rectification and impurity production [9]. In addition, with the wide antenna array, these flux lines can project large areas and enclose substantial RF flux - these have been modelled in some detail [10] and the appearance of high voltages under typical conditions confirmed.

In order to alleviate this process and enable monopole operation, a 'separator' has been installed on one array. This comprises an additional limiter 60 mm wide mounted in the c. 90 mm gap between the two antenna of the array. The tile face is about midway between the screen elements and the limiter tiles. The separator section, as subsequently modified, is shown in fig 9. The separator is supported by the top and bottom protection rails. This increases the disruption loads on the rails, which have each had two additional supports to the torus fitted as illustrated. These supports also earth the rail to the torus, and have also enabled the electrical break to the limiter to be short circuited. These earthing changes are intended to reduce interaction with the rails.

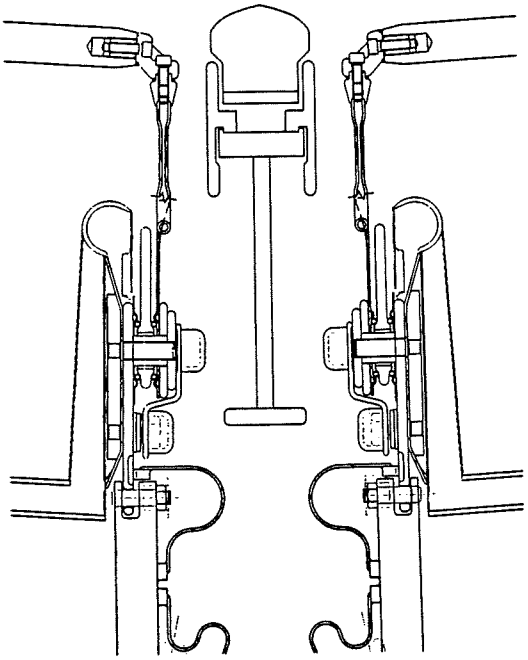

Fig.9 A section through the separator (as modified)

In the limited period of operation with this separator in place, it has been found that the heating efficiency in monopole (normalised to dipole efficiency) has been much improved as in fig 10. In addition, the arc damage previously observed on the ceramic break in the rails, and on the top/bottom tile assemblies have all disappeared. The voltage is however limited to 20 kV by arcing across the small remaining gap between the separator and the antenna. Inspection of the antenna after subsequent removal from the torus confirms this arcing, and also indicates substantial currents in the support arms between the antenna and the torus, in particular at the corners of the antennae, both with and without the separator.

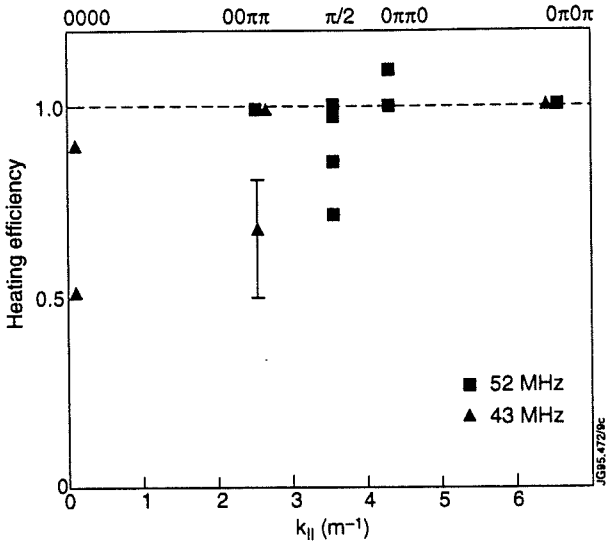

Fig.10 The heating efficiency after installation of the separator

These observations are all consistent with the appearance of substantial leakage flux trying to close around the back of the antenna through the slotted side walls, but forced by the support arms to close around the top and bottom of the antennae. This flux induces sufficient voltage between the antenna and the limiter/separator assembly to induce arcs, and also induces currents in the corner straps to produce the observed damage. The obvious remedy to this is to establish good RF contact between the limiter/separator and the sides of the antenna. This is likely not only to improve the voltage limit but also the coupling. Such a link is, however, severely complicated by the consequential disruption currents in the structure with a DC connection, and by space limitations/spurious resonances for a capacitative link. No viable solution for such a link has been found. Detailed modifications to the separator design, combined with additional rails partially blocking the sidewall slots on the antenna and increased current ratings on the support arm assembly, appear to increase the voltage limit sufficiently and are being incorporated in the antenna at present.

IV. IMMINENT MODIFICATIONS

All antennae have been removed from the torus and are presently being modified as follows:

A. Crossover strap

An additional plate is being fitted to the crossover strap to increase the capacitance to the back wall and reduce the impedance to about 30 ohms. The prototype antenna has been modified and tested at both low and high power. This modification has been shown above to much reduce the imbalance, which will allow a significant reduction in peak voltage at full power. The scattering matrix for the modified four strap array on plasma has been estimated from all of the available data. This indicates an improvement in average

coupling of perhaps 20 % at mid frequency, no change at 50 MHz and perhaps a slight decrease at 55 MHz.

B. Separator
Separators are being fitted to all modules, with the design modified to increase the gap to the antenna from 13 to 17 mm, and with boron carbide coating of the side plates - this modified section has been shown in fig 9 above. In addition, the sidewall slots are being blocked for 200 mm at each corner of the antenna, and adjacent to the radial section of strap near the centre of the antenna. This will reduce the flux around the closed ends of the antennae and thus the voltage induced between screen and separator. More robust earthing straps are being fitted on the support assembly.

C. Limiter position
Inspection of the antenna, and measurements of the density on the limiter tiles indicate that the power density from the plasma on the antenna screens is very low. This is in part due to the new plasma position control system which does not allow operation with the separatrix close to the limiters. The antennae are therefore being moved 6 mm into the torus, which reduces the gap to the tiles to 11 mm. In addition, the lower straight limiter section is being modified to follow the curvature of the antenna to reduce the shielding of the lower part. Estimates of the coupling resistance from codes and from operational data indicate an improvement of 20% in coupling from these changes.

V. IMPLICATIONS FOR ITER

Experience with the A2 antenna has some implications for the design of an RF system for ITER. Many of the difficulties experienced with A2 arise from constraints on the design specific to the pumped divertor phase of JET, in particular the control of disruption loads. Others are more general and are summarised as follows:

A. Coupling
Improved codes and validation of those codes are required. Radial and poloidal currents in the antenna at the feeds and short circuits appear to degrade coupling, as does leakage flux around the ends. A half-wave current strap with centrally peaked currents and minimum current at the feeds as envisaged in the present ITER design minimises these effects and is also likely to be more accurately modelled. Monopole operation gives better coupling, but the design criteria for efficient operation remain to be fully understood. Cross coupling between straps can modify the balance between straps and needs to be taken into account. ELM tolerant matching and protection systems are needed to improve power delivery to ELMy plasmas.

B. Protection limiters
The design of these is critical to the performance at low $k_{//}$. The limiters should be in close RF electrical contact with the antenna, and prevent any leakage flux around the back or ends - an extensive 'earth plane' around the antenna about flush with the screen is ideal. The previous vaulted ITER first wall with continuous plasma facing conducting shell in close contact with an antenna recessed into the wall or port is a good example. Slotting of sidewalls complicates this issue and needs to be well justified in improved heating or current drive efficiency. Large arrays such as JET A2 and as envisaged for ITER, can have dimensions in the toroidal direction similar to the wavelength. New effects which are not well understood can arise in this case, and sub-division into toroidal segments is a good precaution in the interim.

C. Voltage limits
The A2 antenna design used E-field criteria from A1, and the lack of significant arcing in the antenna up to 30 kV on the torus confirms these values. The voltage limits at JET indicate that operation of ITER above 30 kV requires better understanding of these limits, in particular at ceramic supports/windows. The removal of ceramic supports from JET has been instrumental in increasing the voltage limit - any such ceramics are likely also to be a prime source of difficulty on ITER.

VI. CONCLUSION

The coupling efficiency, heating efficiency and limitations to operation of the A2 antenna after one year of operation, including a period after installation of a prototype separator, has been reviewed. Together with the results of inspections both in-vessel and after removal of the antenna from the torus for modification, these results have led to an improved understanding of the antenna and some enhancements to the design. The implications of this experience for ITER have been reviewed. Whilst the design of large arrays optimised for FWCD is only partially understood, and coupling prediction codes need further validation and development to take into account the real geometry, the design basis for ICRF heating systems is well founded.

ACKNOWLEDGEMENT

R Goulding, P Ryan and G Bell of Oak Ridge National Laboratory and D D'Ippolito of Lodestar have contributed to the work described here through numerical modelling of the antenna, and various measurements on the flat bed models.

REFERENCES

1. A. S. kaye et al, Fusion Engineering and Design 24 (1994) 1-21
2. T. Wade et al, Fusion Engineering and Design 24 (1994) 22
3. D. S. Start et al, to be published in Proc. 11th Top. Conf on RF Power in Plasmas, Palm Springs, May, 1995
4. M. Bures et al, 21st EPS Conference on Controlled Fusion and Plasma Physics, Montpelier, 1994, Europhysics Conf. Abstracts 18B,Part II, 944-951
5. M.D. Carter et.al, Nuclear Fusion, to be published.
6. P. U. Lamalle et al, to be published in Proc. 22nd EPS Conf. on Controlled Fusion and Plasma Physics, Bournemouth, 1995.
7. V.P. Bhatnagar et al, Radiofrequency Power in Plasmas, Charleston 1991, AIP Conf.Proc. 244, 115-124
8. V.P. Bhatnagar et al, 18th EPS Conference on Controlled Fusion and Plasma Physics, Berlin, 1991, Europhysics Conf. Abstracts 15C, Pt I, 369-372
9. M. Bures et al, Plasma Physics and Controlled Fusion, 33, 8, 937, 1991
10. D. D'Ippolito, Private communication

Diagnostics for the JET MKII Divertor

P. C. S. Prior and the JET Diagnostic Engineering Group
JET Joint Undertaking, Abingdon,Oxon,OX14 3EA, UK.

I. INTRODUCTION

During the 1995 shutdown of JET the permanent structure for the MkII Divertor is to be installed, with removable target tile carriers and tiles for the MkIIa configuration. Diagnostics have been designed, constructed and are being installed to accommodate these new arrangements. This paper describes the engineering aspects, construction and installation.

II. MKII DIVERTOR AND DIAGNOSTIC INTERFACES

The major elements of the divertor are shown in figure 1.

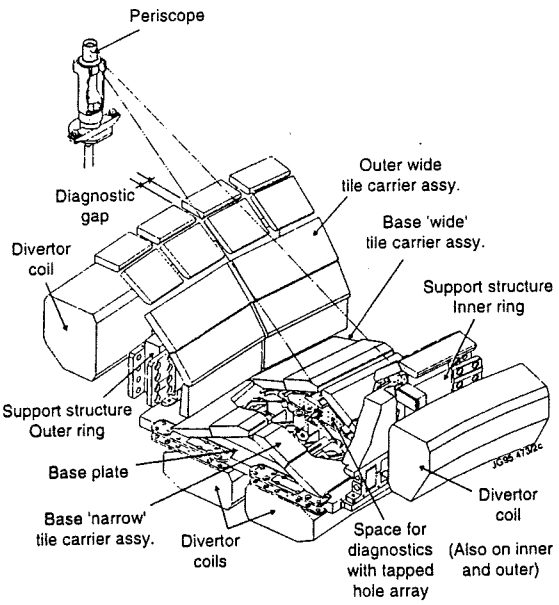

Fig. 1 JET MKII divertor 'module' general arrangement

24 modules make up the complete divertor and space is provide for the installation of diagnostics between the wide and narrow tile carriers. A standard matrix of tapped and dowel holes is provided on the wide carrier for the mounting of diagnostics. Alternate toroidal gaps between the tiles of at least 10mm provide lines of sight of the plasma and space for the installation of Langmuir probes and microwave antennas. The divertor is a hostile environment for diagnostics with tile back surfaces reaching 700°C and radiant heat loads through the tile gaps from the plasma. Remote handling electrical connectors are fitted to allow the remote removal of the tile carriers.

III. ELECTRICAL SYSTEM

The MkII divertor structure replaces the existing MkI design but utilises the same basic electrical instrumentation system. 8 electrical vacuum feedthroughs, mounted in the lower ports of the vacuum vessel, are terminated at nine 80 pin connectors on the inner wall. As the toroidal distribution and types of diagnostic have been revised for the MkII a new toroidal distribution and connection system has been designed which connects from the existing sockets to the support structure modules and then to the tile carrier assemblies. A new feedthrough on a mid plane horizontal port is to be installed providing additional connections including 'hard wired' services. Figure 2 shows a schematic of the wiring routing.

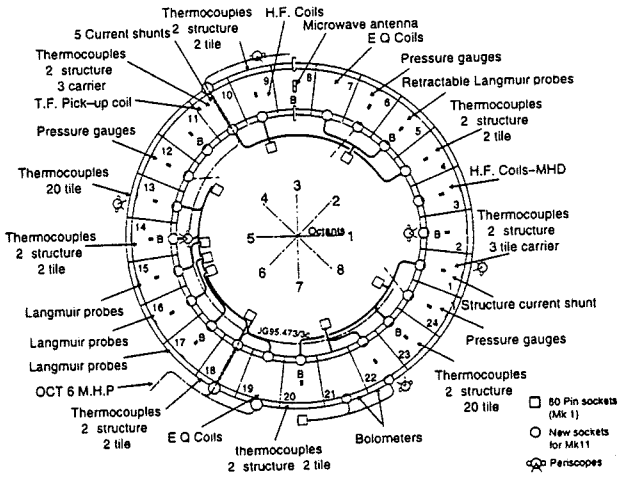

Fig. 2 Diagnostic locations and wiring.

A. *Wiring types*

The following wire types are used. a) Mineral insulated cable Ø1.0 or Ø1.5mm with its ends sealed with metal/ceramic/metal vacuum seals. These are robust cables but their terminations are bulky (Ø5 mm). b) Glass braid insulated twisted pairs with stainless steel outer braiding and either K-type thermocouple or OFHC copper conductors Ø 0.4 mm. This is a flexible material which can be easily terminated, however exposed glass insulation is very vulnerable to damage. c) Glass braid insulated single core cable with stainless steel outer braid and Ø1.0 mm Glidcop®[1] conductor. This provides a more robust cable for high

current applications. d) Glass braid insulated quads with double stainless steel screen developed especially for the low noise requirements of the bolometers.

B. *Electrical connectors*

To allow the in-vessel connection of systems during installation under conditions of beryllium contamination (requiring in-vessel operators to wear 'full suits') and subsequent remote handling operations, four types of connector have been developed. All the connector designs result in an 'untwisted' section of wire with its subsequent pick up problems. Where possible the connectors are oriented to present this area to the toriodal field which can be compensated for. Where this is not possible dummy connections are made to assess the errors induced.

1) Manually installed connectors: In various sizes from 2 to 80 contacts these are based on commercial male /female sliding socket contacts (∅1.0 mm male pin - alumel/chromel) and are not remotely handleable. Various versions are available compatible with both M.I. and braided cables and are used for the interconnection of wiring looms and diagnostic sensors.

2) *Remotely installed connectors*: Typically with around 20 contacts these connectors use the same socket contacts as the manual connections but the mounting configuration and design allows for remote installation and removal. These connectors are used on all tile carriers to allow their remote handling. In-vacuum tests have shown that the contacts can handle 10 A without damage or welding.

3) *Sprung contacts*: To connect the fixed Langmuir probes mounted on the 'narrow' tile carrier a sprung contact has been developed allowing remote removal of the tile carriers and allowing for the relative movement between the tiles during a plasma shot. In vacuum testing has shown that the stainless steel/aluminium bronze contacts can handle at least 9 A, at a peak of 100 V with 1mm movement at 2 Hz without excessive wear, welding or electrical noise Figure 7 shows the contact in position.

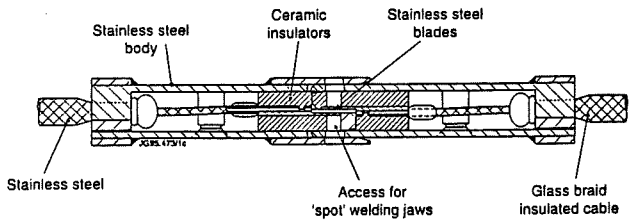

Fig. 3 'Hard wire' connector

4) *'Hard wire' connectors*: To minimise noise and maximise the reliability some systems are to 'hard wired' without sliding contacts. To facilitate this a 2 contact connector has been developed which can be resistance spot welded in vessel. Figure 3 shows the cross section of the connector.

C. *Cable protection and management*

The cabling has a typical upper service temperature of 500°C. To protect the cables from high heat loads (from the plasma or the backs of the hot tiles) thermal shields are incorporated into the diagnostic designs.

The space available for wiring in the tile carriers is small. In particular the inner and outer carriers are very confined. Allowances must be made for the travel of the RH connectors which further constrains the available space. Cable densities are especially high for the bolometers and pressure gauges.

IV. DIAGNOSTIC SYSTEMS AND LOCATIONS

Figure 2 shows the toroidal distribution of the diagnostics around the divertor and shows the systems that will be available at the start of the next campaign. Most of these are modified and improved versions of the systems installed for the MKI divertor. These systems are grouped and discussed according to their mounting location. Only those systems closely interfaced with the divertor are described here.

A. *Structure mounted*

The following systems interface directly with the support structure and are mounted before the structure modules are installed in the vacuum vessel.

1) *Equilibrium coils*: 2 sets of 22 Equilibrium coils (in normal/tangential pairs) are mounted within special modules (7&19) of the support structure. Each coil consists of an Inconel core wound with ∅1.0mm mineral insulated cable and has an effective area of $0.025m^2$. Figure 4 shows the typical arrangement. Accurate plasma position control in the divertor region, which is remote from magnetic sensors on the vessel walls, relies on this system. One set of is to be 'Hard wired' to maximise reliability.

2) *Bolometers*: Part of a set of high resolution Bolometer cameras are mounted on modules 21 and 22. These provide 16 channels and view the plasma through the 20mm 'diagnostic' tile gaps. Bakeable heads that do not require water cooling are used. Due to the special electrical requirements of additional screening, quad cables, low microphony and the position of the existing wiring in the vessel, the cameras are connected via a socket mounted on the outer ring of the support structure module.

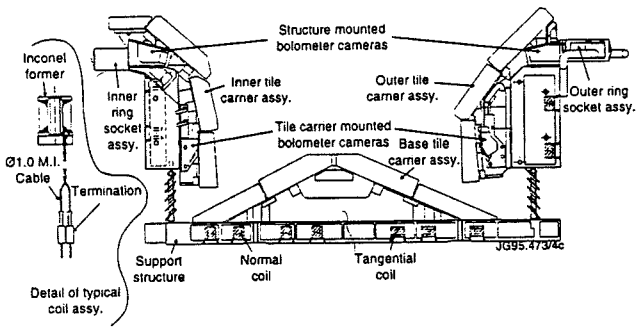

Fig. 4 Bolometers and EQ coils.

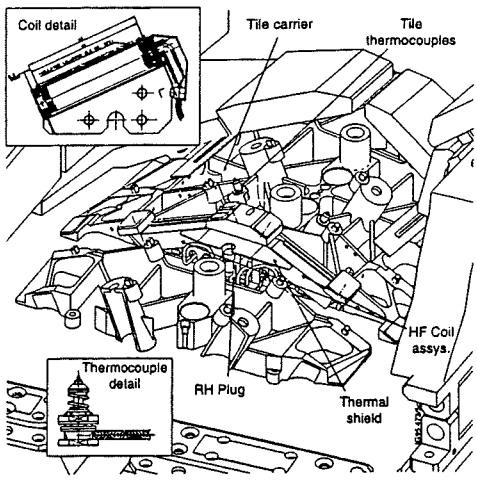

Fig. 5 MHD coils and tile thermocouples.

3) *Thermocouples and shunts*: A number of K-type thermocouples are welded to the structure to measure its temperature and series of current shunts are fitted to asses the currents circulating in the structure base plate and rings.

B. *Tile carrier mounted*

The attachment to the tile carrier has been made common for each diagnostic instrumentation package which is attached to the carrier during its assembly with its tiles.

1) *Tile Thermocouples*: To provide a measurement of the tile temperature K-type thermocouples are mounted within the tile carrier structure. Additional holes have been incorporated in the webs to allow fixing and wire routing. The thermocouple junctions are held against the back surface of the tile by spring pressure (≈10 N). This simplifies installation of, and avoids modification to, the tiles. Clearly some reduction in thermal response is to be expected. Tests at JET have shown that the thermocouple measures 93% of the equilibrium temperature of the tile and 90% of this value is achieved in 5s following the end of a pulse.

2) *MHD Pick up coils*: Two pairs of magnetic coils are mounted in the base carriers for MHD measurements in conjunction with other 'fast coils' in the vessel. Each coil is formed from titanium wire wound around a ceramic former providing an effective area of 0.017 m^2. This gives good frequency response up to 500 kHz. See figure 5.

3) *Toroidal field Coil*: A single coil mounted in module 10 for toroidal field measurements in the divertor region above the base structure. Coupled with other TF measurements at the top of the vessel field variations can be monitored and estimates of 'Halo currents' made. This coil is constructed from Ø1.5 mineral insulated cable wound on an Inconel former providing an effective area of 0.043 m^2.

4) *Pressure gauges*: At three toroidal positions ion gauges are mounted on the inner, base and outer tile carriers. Each gauge requires a 30 A supply for its filament. 6 pins in the RH connector are used to provide this.

5) *Retractable Langmuir probes*: Figure 6 shows the arrangement of two sets of moving probes. Coils, mounted across the toroidal field, provide 0.175 Nm of torque in a field of 3 T when supplied with 3 A. A flexible link connects the coil to a bar, sliding in alumina bearings, which carries the array of individually insulated probes. Each probe is connected via a flexible Nickel braid. Typical movement times of 10 ms are expected and maximum exposure to the plasma of 20 s.

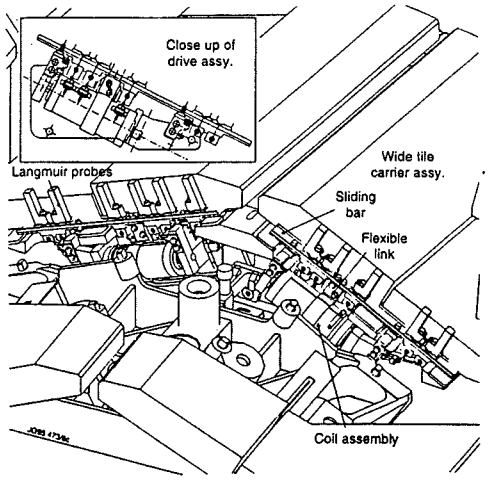

Fig 6 Retractable Langmuir Probes

6) *Bolometers*: To complete the set previously described a further 3 cameras are mounted on the inner and outer tile carriers. These are connected via the remote handling connectors.

C. *Tile mounted*

1) *Fixed Langmuir probes*: An array of fixed Langmuir probes is mounted on the tile edges at several toroidal locations. The relationship between probe and shadowing tile edge can be controlled and measurement accuracy maintained during tile expansion and movement. A set of sprung contacts is used to connect to the probes mounted on the narrow tile carrier. Figure 7 shows the arrangement.

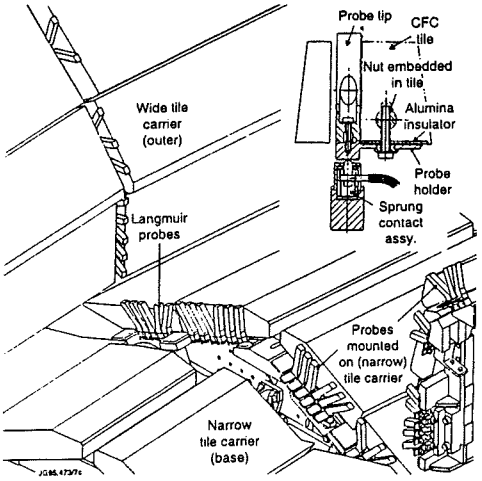

Fig. 7 Fixed Langmuir probes

D. *Viewing diagnostics.*

1) *Microwave systems*: A set of antennas are mounted close to the support structure and provide two sight lines through the divertor plasma. The antennas are located between the tile carrier assemblies and the tile edges are modified to provide adequate clearance. These are coupled to a reflectometer, interferometer and ECA measurement Figure 8 shows the antennas in position.

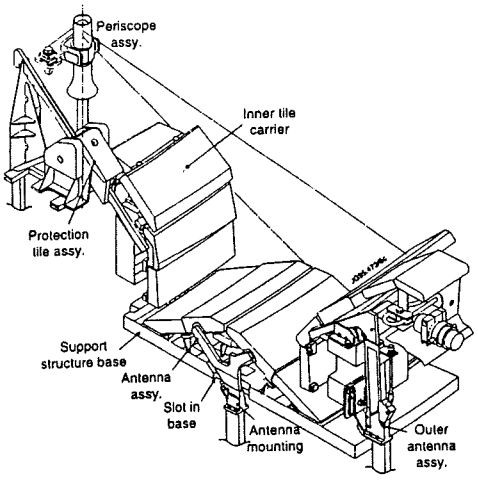

Fig. 8 Microwave antenna and periscopes

2) *Periscopes*: Optical systems provide a view of the plasma as shown in figure 8. Cameras for the visible spectrum and fibre optic arrays connected to spectrometers covering 400 to 750 nm are used to view the divertor. The lines of sight are through the upper tiles.

V. EXPERIENCE WITH THE JET MKI DIVERTOR INSTRUMENTATION

JET has recently completed an operational campaign in mid 1995 and extensive experience with the MKI diagnostics has been obtained.

Following the initial installation of the feedthroughs and the MKI diagnostic system a failure rate of <2% was observed. Most of these were due to known damage which had occurred during installation of the more delicate systems.

During the last operational campaign faults have appeared on some of the low voltage/low current diagnostics signals. These appear typically as intermittent increases in line resistance, sometimes midshot. For the magnetic measurements which, are integrated and used as plasma position control signals, this has serious effects leading to disruptions. Attempts to cure these faults by passing high current spikes (sometimes called 'fritting') have been partially successful but the repairs seem to be only temporary.

To characterise the inaccessible in-vessel wiring a Time Domain Reflectometer is to be used. This will allow the position of the faults to be estimated (expected to be at one of some 12 junctions in a typical feed/return pair) and any degradation monitored.

Further in-vacuum testing of connectors and cable joining techniques is on going in an attempt to isolate the cause of the faults. Clearly these failures are of great concern.

To avoid these problems on critical systems 'hard wiring' is to be used with all joints either welded or vacuum brazed.

VI. CONCLUSION

A complete suite of diagnostics have been successfully integrated into JET's new MKII divertor design. The tile carriers and attached diagnostics can be removed from the vacuum vessel by remote handling techniques for either repair or replacement. JET's next operational campaign and remote tile exchange will provide valuable experience of the diagnostic performance and reliability.

REFERENCE

[1] SCM Metal Products Inc, Ohio, USA.

APPLICATION OF 'BEST-FIT' SURVEY TECHNIQUES THROUGHOUT DESIGN, MANUFACTURING AND INSTALLATION OF THE MKII DIVERTOR AT JET

B. Macklin, R. Brade*, G. Celentano, R. Shaw**, J. Tait, E. van Lente
JET Joint Undertaking, Abingdon, Oxfordshire, OX14 3EA, UK.
*GEC Alsthom, Leicester, UK.
**ITER-EDA, San Diego, U.S.A.

The precise installation and alignment of large components in an activated and beryllium contaminated fusion device is a problem which must be faced in JET as well as future devices such as ITER. To guarantee the successful alignment of the MKII Divertor in JET it was essential that, early in the design phase, realistic manufacturing and installation tolerances and restrictions were identified and considered.

The main components of the MKII divertor structure are an inner and outer ring mounted on a base plate (figure 1). The overall diameter of the assembly is 6m and is dismantled into 24 sub-assemblies (modules) for installation [1]. The structure must be installed very accurately whilst wearing full pressurised suits. As the other major in-vessel components remain unchanged i.e. RF antennae, poloidal limiters and guard limiters it is important that the new divertor be installed to the same centre as these components i.e. to the machine centre which is defined as the centre of the in-vessel datum system. Major considerations in the design process were the installation accuracy required, the installation method and restrictions imposed by the existing in-vessel structure. Joints between modules could only be made from one side due to access restrictions. Design of the support system had to be such that minimal modification to the existing in-vessel structure would be required. The tight tolerances necessary to ensure the mechanical integrity of the module joints were compromised by the necessity to have realistic assembly tolerances.

I. BEST-FIT CONCEPT

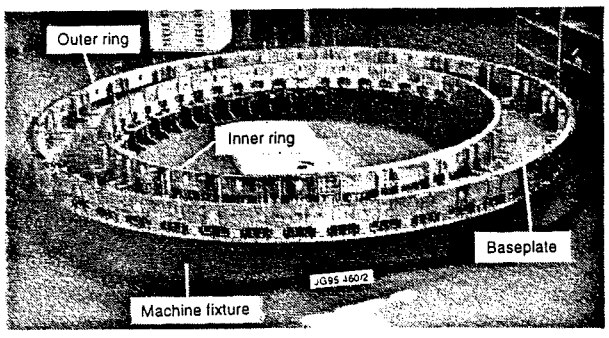

Figure 1 Divertor Structure Components.

JET's Computer Aided Theodolite (CAT) system [3] was used extensively and successfully in the previous shutdown when the MKI Divertor was installed [2]. It was decided that this system should be used again. From previous experience it was clear that optimum use of the CAT system implied a different approach to manufacturing and installation. When a component is manufactured within a tolerance band, which is inevitably significant on a 6m structure, to attempt to install the component to its theoretical dimensions is simplistic. The installation team will not know if any error they see is due to incorrect positioning of the component or an inherent manufacturing 'error' or inaccuracy. Therefore the concept of installing a component to its 'as-built' coordinates was developed. This allowed the use of a 'best-fit' approach where the actual component dimensions are allowed to float into their best average fit to the theoretical dimensions. This technique has the advantage of allowing the effect of any single dimensional error, be it a manufacturing or installation error, to be minimised (figure 2). This implies, of course, a maximum allowable error at a point.

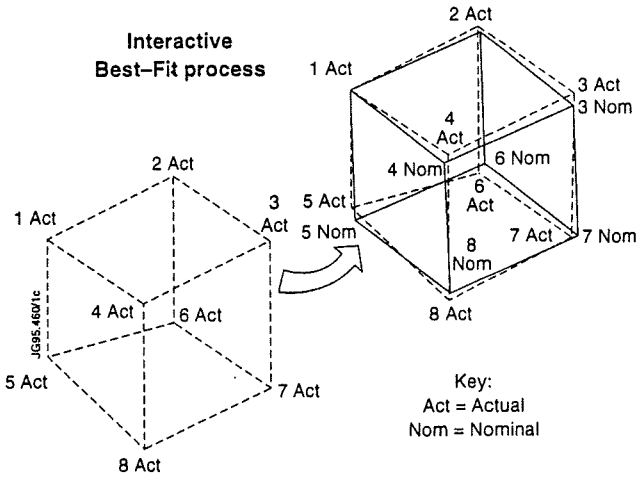

Figure 2 Illustration of Best-fit Technique.

The best-fit is achieved by using the CAT system computer software to overlay the as-built file onto the nominal file (figure 3). It was therefore necessary to plan to use the CAT system during the manufacturing cycle of the divertor structure both to confirm that the required dimensions had been achieved and to record the necessary as-built information necessary for installation.

II. MANUFACTURING CONCEPT

a. Overview

From an early stage in the manufacturing process it was clear that the assembly of the components of the divertor i.e. baseplate and ring segments would be critical to the achievement of the conflicting tight tolerances on position, roundness and concentricity. Consequently the CAT system was first used to survey the fixture (figure 2) on which the

components were to be located for final machining. Final machining included skimming of the datum diameters and base surface as well as drilling of the H7 dowel holes required at the joints between the modules. Inner and outer rings were assembled on the fixture using precision dowels for location, final machined and then removed from the fixture as complete assemblies. Similarly the baseplate assembly was located on the fixture for final machining. Inner and outer ring assemblies were then assembled onto the baseplate (first assembly) [1]. Confirmation of the accuracy of the positioning of the dowel holes guaranteed the location of the components for the final machining operations and was a crucial part of the manufacturing concept.

b. Machining Fixture Survey

Results of the machining fixture survey were analysed using the CAT system software to determine first the centre of the ëbest-fití circles through the baseplate location dowel holes. Similarly, 'best-fit' circles were fitted to the dowel holes on the inner and outer rings. These were checked for roundness and concentricity with the baseplate centre. The positions of all surveyed points were compared with their theoretical positions as defined in a ënominalí file. This file was generated using JET's CAD system and allowed a very quick check on the position of all dowel holes. Critical dimensions such as the chords between dowels for adjacent modules were also checked carefully. All survey results were assessed in the light of slightly tighter than contract tolerances at this stage to allow for subsequent dismantling and reassembly.

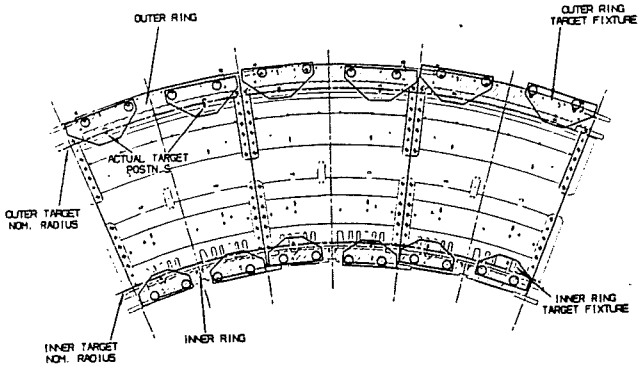

Figure 3 Best-fit Applied to Divertor Structure.

c. First Assembly

The manufacturing process for the divertor structure included two major assembly operations:- the first and second assemblies. During the first assembly the main components of the inner and outer ring and baseplate were brought together for the first time. This was followed by a CAT survey of the complete assembly while still located on the machining fixture (figure 4). The CAT system software was used to analyse the results of this survey. Best-fit circles through the inner and outer ring and baseplate were checked for diameter and concentricity. The positions of surveyed points were compared with nominal file positions. Critical chords across module joints as well as diagnostic location features were examined. This survey confirmed that the components had been manufactured and assembled correctly and within tolerance.

d. Second Assembly

The structure was then broken down into 24 sub-assemblies (modules), each one consisting of an inner and outer ring and baseplate segment. Modules were then cleaned, baked and vacuum leak-tested and fitted with other components e.g. baffles prior to the second assembly. The second assembly was a simulation of the installation method and sequence planned for use during the installation at JET. A final survey of the complete structure after the second assembly provided the file of 'nominal' coordinates for the installation. It provided a very valuable opportunity to identify any weaknesses in the planned installation method. As the second assembly was carried out under ideal conditions i.e. without wearing pressurised suits in a confined space, it provided a useful guide to the best assembly accuracy which would be achievable.

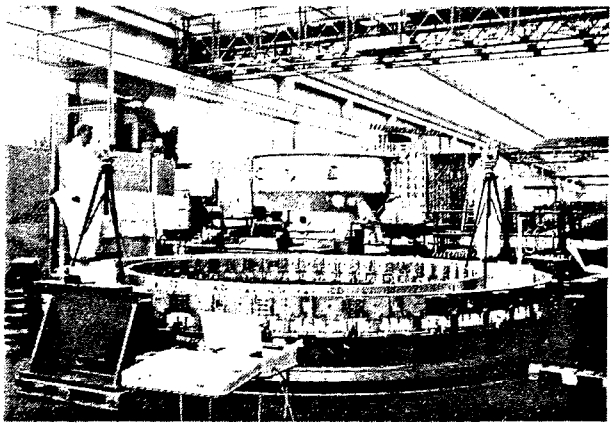

Figure 4 Survey of Structure after First Assembly.

III. SURVEY PREPARATION AND DEVELOPMENT

a. Equipment

To maintain the high standard of optical survey work which was a feature of the MKI Divertor installation at JET presented a challenge for the MKII installation team when all work would have to be carried out whilst wearing pressurised suits due to the beryllium contamination of the vacuum vessel. Initial development included modifying the theodolites by fitting miniature video cameras to the eyepiece. Whilst early tests looked promising, it was considered that less sophisticated alternatives should be considered. In parallel modified half-suits with smaller than normal helmets and optically clear panels were developed

and tested. Successful trials with these suits confirmed that this was the most reliable way of continuing optical work in-vessel. To accomodate a requirement for very accurate height surveys a new precision automatic digital level with an invar barcode staff was procured. Special techniques and software were developed to allow the output from this instrument to be manipulated by the CAT system software.

b. Manpower

The volume of optical survey work planned for the MKII installation combined with a higher level of radiation and a much shorter shutdown meant that the survey team had to be doubled from four to eight people. Accordingly four additional inspectors were recruited and trained in the specific survey techniques which had been developed for the previous shutdown at JET.

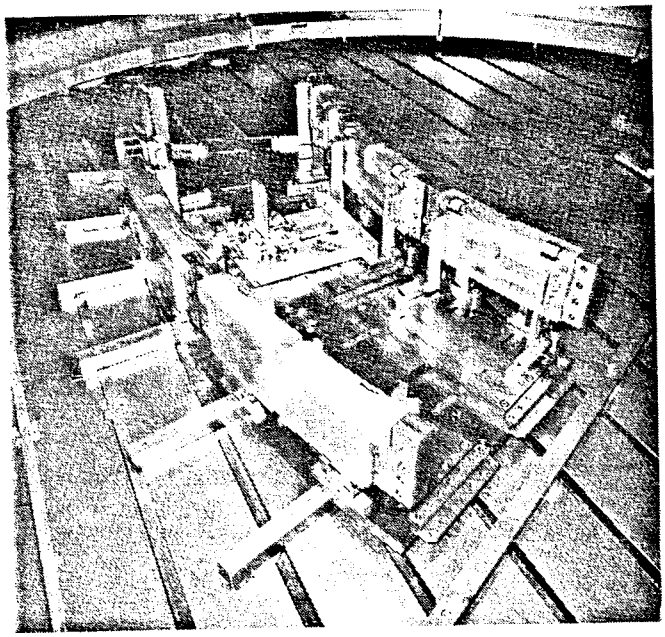

Figure 5 'Dummy' Modules Used for Trials.

c. Techniques

The optimum survey technique for all surveys related to the machining fixture, the first and second assemblies at the manufacturers and the in-vessel installation was studied and developed extensively at JET. JET's CAD system was deployed to determine optimum theodolite locations and then to prepare a series of drawings which detailed instrument positions, number of set-ups and points to be surveyed. An extensive series of trials was also carried out on a detailed engineered mock-up of the structure to ensure minimum time delay during the manufacturing and installation cycle and to qualify the survey accuracy achievable (figure 5). These trials also allowed the development and evaluation of the necessary optical target fixtures to fit the datum features, which unfortunately were slots. Tests carried out proved fit, absolute accuracy and repeatability. All tests were carried out within a greater framework of assembly, handling and training trials. Installation trials were carried out with the structure mock-up in JET's training facility (a full size replica of 4 octants of the vacuum vessel). Useful experience was gained here particularly with regard to optimising the technique for adjusting module positions. It soon became apparent that if the the modules were level satisfactory positioning could be achieved in a few iterations.

IV. IN-VESSEL DATUM SYSTEM

a. MKI Datum System

During manufacturing alot of care was taken to ensure the dimensional accuracy and concentricity of the components of the Divertor structure. Equally important was to ensure the concentricity of the new and old divertors. New surveys of the in-vessel datum system, which had been created by and used with the CAT system during the MK1 Divertor shutdown, afforded the means to ensure this. Previous use of the CAT system had resulted in a system of 184 in-vessel datum points. However, the subsequent campaigns of operation and the flexibility of the vacuum vessel resulted in movement of the vacuum vessel and the loss of the absolute values of the datum system. Employing the best-fit approach, the datum points can be resurveyed and the resulting file can be best-fitted to the that used during the previous shutdown. This ensures concentricity of the old and new datum systems.

b. Establishing a New Datum System

High levels of radiation and the difficulty and consequent time implications of carrying out an extensive survey with optical instruments while wearing pressurised suits ruled out the possibility of using the CAT system for the re-survey of the datum system. Instead convergent photogrammetry, which has the principle advantage of speed of data capture, was used [4]. The resulting data file was in a form compatible with the CAT system software and could be easily best-fitted to the file which defined the old datum system. The CAT system, using these datum points, can then be used to determine the position of components relative to the centre of the JET machine.

V. MKII DIVERTOR STRUCTURE INSTALLATION

Typically modules will be installed in groups of three, progressing both clockwise and anti-clockwise from a block of three datum modules. The datum modules will be positioned with the assistance of the CAT and the in-vessel datum system and then locked in position. Up to eight separate CAT surveys will be required to check the position of the modules as the build progresses round the vessel. Completion of the circle will be followed by a CAT survey of the complete structure to confirm concentricity, circularity etc. before final lowering and torquing of the structure. After lowering the structure may be surveyed using photogrammetry. This survey would use self adhesive targets fixed to the surface of the structure and will allow a more extensive evaluation of the structure geometry than the CAT surveys which uses targets at discrete points only - typically six per module. Experience gained during the second assembly indicates that this survey may not be

necessary and that a CAT survey would be satisfactory. Either survey will provide the 'as-installed' position of the divertor structure. Accurate 'as-installed' information is critical, in particular to provide accurate information necessary for the design of the MKII Gasbox tile carriers which will be installed remotely.

VI. PLANNING FOR SURVEYS IN THE FUTURE AT JET

The next major planned shutdown at JET will be for the installation of the MKII Gasbox Divertor cofiguration. This shutdown will follow the tritium experiment (DTE1) currently planned for late 1996. High levels of radioactivity are anticipated such that man access to the vacuum vessel will not be possible. Accordingly a full remote handling shutdown is being planned. Research has been going on at JET over the last year to identify survey systems suitable for use in a remote handling scenario [6]. Videogrammetry, along with selected laser scanning techniques have been identified as being potentially suitable for remote deployment. Videogrammetry is a digital form of convergent photogrammetry, which uses a motorised, remotely operable CCD camera which could be mounted on JET's Articulated Boom. One of the major limitations of most survey systems with regard to remote operation is the problem of targetting. Not surprisingly there are no commercially available optical targets which are vacuum and plasma compatible. Tests were recently carried out at JET using a simple form of target which was an accurately machined 6mm diameter hole in an inconel block. When the hole is selected on a screen with a cursor best-fit algorithms are used to determine its centre which is the datum point. Comparison of survey results using these targets and conventional targets showed a correlation of better than (0.3 mm. A design and development programme is now underway to optimise the targets. Factors being considered are the need to shield the datum face from the plasma while still maintaining its visibility. Different configurations of hole will be assessed to determine that which gives the optimum contrast between the hole and surrounding metal in poorly lit conditions and considering that the surface may be coated with beryllium.

A manual (i.e. with the camera hand-held) videogrammetry survey is scheduled to take place at the end of the present shutdown in any case. This survey will provide the coordinates of the in-vessel datum targets which will be used for the 'best-fit' at the start of the next shutdown. Trials carried out in JET's training facility (figure 6) have shown that the digital model of the vacuum vessel and its components can be interrogated to yield positional information about any component in the model by selecting the appropriate feature of the component using a cursor. The accuracy will of course be reduced but should still be of the order of 1mm.

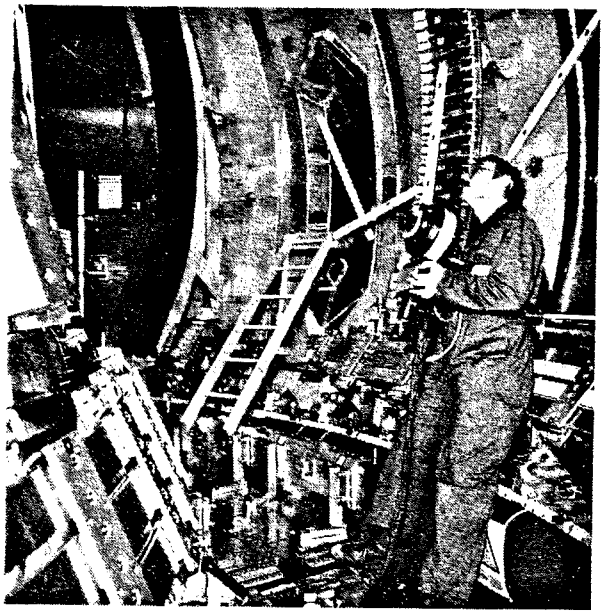

Figure 6 Videogrammetry Trials in JET's Training Facility.

VII. CONCLUSION

The successful completion of the manufacturing stage of this project confirms the benefit of extensive and detailed preparation and development of the survey and installation concepts in parallel with the manufacturing sequence. Early CAT checks confirmed the high quality of the manufacturing sequence agreed with De Pretto [5]. The second assembly confirmed that the structure could be built accurately inside the vacuum vessel. Refinements to the proposed installation method were established. CAT surveys on completion of the second assembly confirmed that manufacturing and assembly had been achieved to within (0.3mm which was well within the allowable tolerance. In fact only 20(of the allowable tolerance was used.

REFERENCES

1. Manufacture and Installation of JET MKII Divertor Support Structure. G Celentano et al., 16th Symposium on Fusion Engineering, Champaign 1995

2. Alignment Systems for Pumped Divertor Installation at JET. B Macklin et al., 18th Symposium on Fusion Tecnology, Karlsruhe 1994

3. Leica AG, Photogrammetry and Metrology, CH-5035, Unterendfelden, Switzerland

4. ESIC Reseau Eurisys, St. Quentin en Yvelines, France

5. De Pretto-Escher Wyss S.r.l., I-36015 Schio, Italy

6. Investigation of Measurement Systems Suitable For Use in Remote Handling Operations at JET, E van Lente, JET Report April 1995

Measured Currents in JET Limiters During Disruptions

P. Andrew, P. Miele, P. Noll, R. Pearce, M. Pick, L. Rossi
JET Joint Undertaking, Abingdon, Oxon OX14 3EA, UK

ABSTRACT

Structures mounted inside a tokamak must be able to withstand the electromagnetic forces which arise during disruptions of the plasma. This paper reports on halo current measurements in the JET tokamak during disruptions.

A toroidally distributed array of current sensing tiles reveal that in many disruptions a high degree of toroidal uniformity exists. However in exceptional disruptions the halo current measured at different toroidal positions varies by more than a factor of 2. This latter class of disruption has been observed to result in an asymmetric displacement of the vacuum vessel.

The total halo current is estimated to be up to 15% of the initial plasma current. The halo current width for a particular disruption is estimated to be 8cm.

INTRODUCTION

Elongated tokamak plasmas are susceptible to an axisymmetric instability in which the plasma undergoes a basically vertical motion [1]. A loss of feedback control of the plasma vertical position causes an uncontrolled vertical displacement and will result in a disruption. Alternatively the disruption of the plasma due to other causes will generally result in a loss of vertical stability.

The local changes in magnetic field due to the change in plasma vertical position and plasma current induces currents in the vessel structure. This gives rise to eddy current forces. Forces on vessel components may also arise from currents flowing between the plasma and the vessel, outside the confinement region [2]. This attached current (halo current) tends to be much larger than the scrape off layer currents flowing in a stable plasma [3], probably due to the same large field changes which drive the eddy currents in disruptions. The segment of the halo current flowing in the vessel produces a force on the wall. An opposite restoring force is experienced by the plasma.

Evidence of halo current [3, 4, 5, 6] includes 1) measured difference in toroidal field just inside the top and bottom of the vessel, indicating a net radial current in the plasma, 2) the motion of the vertically unstable plasma which seems to indicate an extra stabilizing force at work, and 3) measurement of the current collected by vessel wall tiles. In addition in JET [6] and JT-60 [7] there is circumstantial evidence of halo currents based on observed damage to in-vessel components.

METHOD OF MEASUREMENT

Fig. 1 shows a cross section of the JET vessel. The mushroom tiles occupy 56 toroidal positions and 2 poloidal positions. Instrumented mushroom tiles are located at 8 toroidal positions, and 2 poloidal positions (Fig. 2). The instrumented tiles are electrically connected to the wall through a 4.65mΩ resistance. The measured resistive voltage drop used to deduce the current is on the order of 10V. Inspection of the mushroom tile current signals during poloidal and toroidal field changes without plasma indicate that the signals are robust against pick-up due to stray loops.

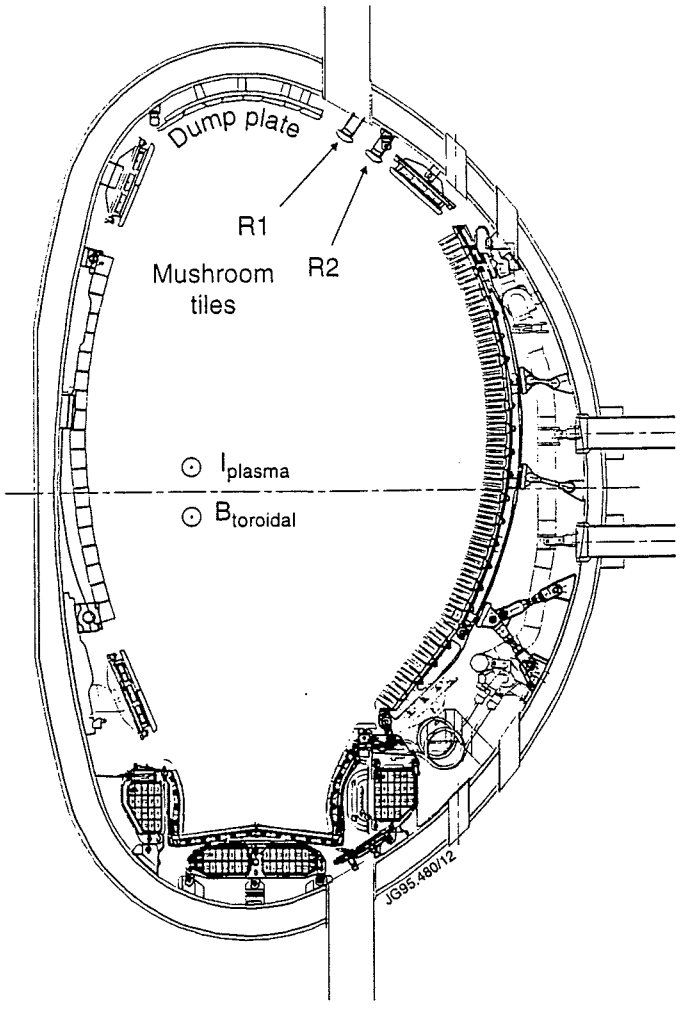

Fig. 1 Cross section of the JET vessel. R1 & R2 denote the two different mushroom tile poloidal positions.

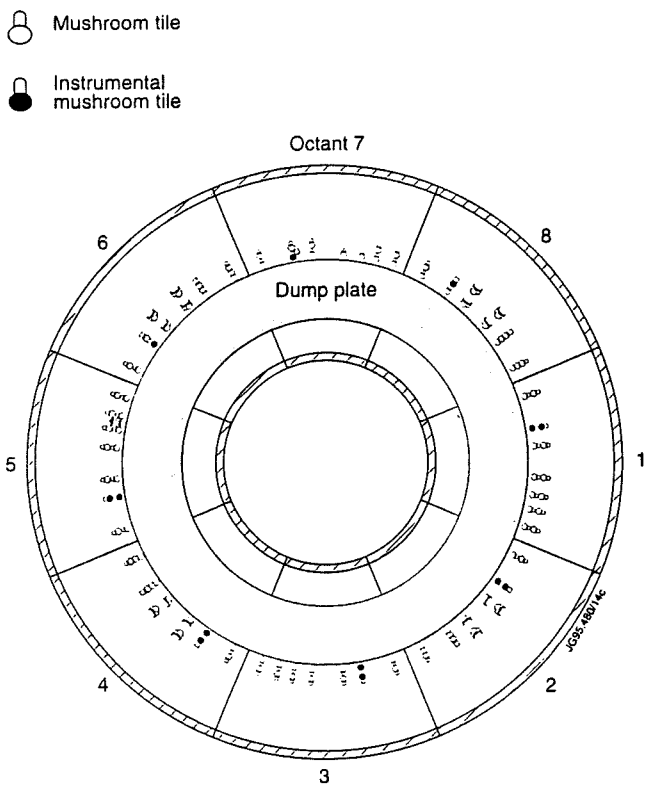

Fig. 2 View from below showing the toroidal distribution of the mushroom tiles.

RESULTS

Fig. 3 shows traces for all the instrumented mushroom tiles for a 3MA plasma which ended in disruption. Also shown are the plasma current and the radial and vertical position of the plasma current centre. In this case, the plasma underwent a significant vertical movement before the plasma current decay. It is this category of disruption which was observed to result in the largest mushroom tile currents.

The mushroom tile current is positive (i.e. into the wall) which is consistent with a halo current flowing along field lines in the same direction as the plasma current. The mushroom tile was usually measured to be in this direction when the plasma moved upward in the disruption. When the plasma moved downward, there was generally no signal on the mushroom tiles.

The dashed lines in Fig. 3 show that the currents in the R1 and R2 rows of tiles are synchronized within their own row, but not with one another. This indicates an axisymmetric motion of the plasma in which the region where the halo current intercepts the wall sweeps over the R2 row, and then the R1 row.

It is difficult to assess the toroidal symmetry of the measured halo current at any single instant because of the fluctuating signals. Fig. 4 shows the integrated mushroom tile signals mapped out according to the toroidal and radial position. For the 3 positions out of 16 (2 rows × 8 octants), where no signal was available, an estimate based on the value from the

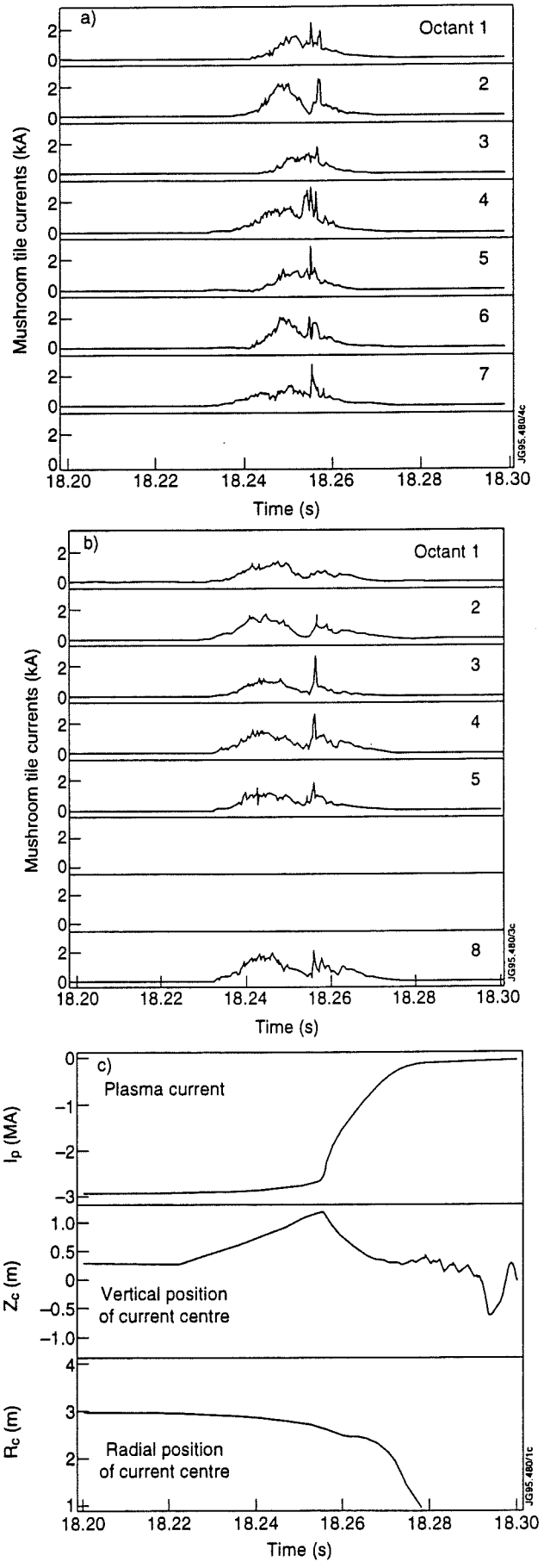

Fig. 3 The measured current collected by a) the 7 mushroom tiles at poloidal position R1 and b) the 6 mushroom tiles at poloidal position R2. Also shown is c) the plasma current and the position of the plasma current centre during the disruption of pulse No. 34250.

If the poloidal extend, $\Delta\ell$, of this region is assumed to remain constant during the sweep, knowing the distance between rows R1 and R2 gives $\Delta\ell \simeq 0.34$m. This will be larger than the halo current width, d, since the current is impinging on the wall at a small angle. Because of the systematic difference in the current measured at even and odd numbered octants, we know that row R2 must at least partly shadow row R1. From this, the maximum width of the halo current is then estimated to be d ~ 0.08m. It should be noted, however, that the width d may have been larger during a later phase of the disruption, specifically when the plasma reaches its maximum vertical displacement. Furthermore, it might be that the width is larger in other disruptions where circumstances do not allow the width to be estimated.

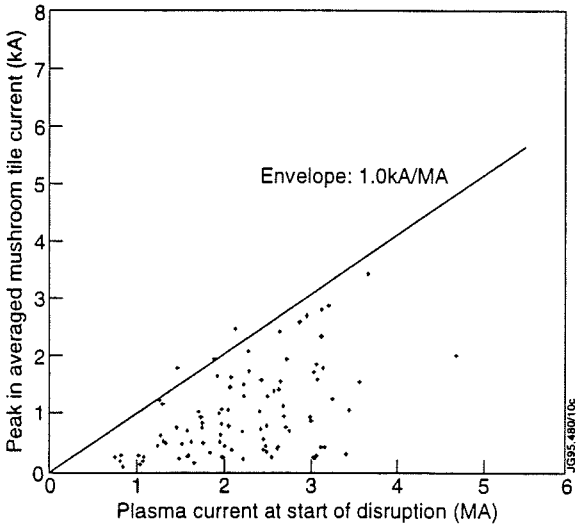

Fig. 7 Peak values of the mushroom tile current averaged over the R1 and R2 sensors.

ESTIMATE OF THE HALO CURRENT MAGNITUDE

In the case of the symmetric disruption in Fig. 3 it was concluded that the poloidal extend of the halo current contact area was of the same order as the poloidal distance between the rows of mushroom tiles. Furthermore it was also concluded that the field lines approached at a shallow angle, such that there is some shadowing of mushroom tiles by one another. Under these conditions, the poloidal component of the total halo current is intercepted by the mushroom tiles. Scaling up the peak, total current measured by $\Delta x/2\,\pi R$ gives $I_H = 0.19$MA, where Δx is the toroidal arc length between instrumented tiles and the tiles which partially shadow them, and R is the major radius at the tiles. Making the same calculations for many disruptions, should yield values ranging between zero and the maximum poloidal component of the halo current.

Fig. 7 shows the peak value of the sum of the measured currents for approximately 200 disruptions from the 1994/1995 operational campaign. The values fill the region between zero and the envelope shown for two reasons 1) some disruptions at a given plasma current may have an inherently small halo current, 2) In some cases the mushroom tile will not completely intercept the halo current. The limiting envelope, applied to all the mushroom tiles gives $I_H = 18\%$ I_p, where I_p is the value of the halo current just prior to the disruption.

CONCLUSIONS

From a toroidally distributed array of instrumented limiters it was observed that the majority of disruptions lead to a toroidally symmetric (within 20%) distribution of the halo current. However, in exceptional cases there is a marked toroidal variation in the mushroom tile current with mode number n = 1.

During the vertical displacement of the plasma the region of halo current attached to the walls could be seen in some disruptions to sweep past the different poloidal locations of the current collecting tiles. The width of the halo current perpendicular to the poloidal field was estimated to be 0.08m, although it may have been larger during a later phase of the disruption.

Finally, from the sum of the collected current it was concluded the magnitude of the poloidal component of the halo current was $I_H \leq 15\% I_p$ where I_p is the plasma current just prior to the disruption.

REFERENCES

[1] J.A. Wesson, "Hydro Magnetic Stability of Tokamaks", Nucl. Fusion 18(1978)87.

[2] F.B. Marcus, F. Hofmann, S.C. Jardin, P. Noll and G Tonetti, "Simulations of Control, Perturbation, Displacement and Disruption in Highly Elongated Tokamak Plasmas",Nucl. Fusion 30(1990)1511.

[3] M.J. Schaffer and B.J. Leikind, "Observation of Electrical Currents in Diverted Tokamak Scrape-off Layers", Nucl. Fusion 30(1991)1750.

[4] E.J. Strait, L.L. Lao, J.L. Luxon and E.E. Reis, "Observation of Poloidal Current Flow to the Vacuum Vessel Wall during Vertical Instabilities in the DIII-D Tokamak", Nucl. Fusion 31(1991)527.

[5] P. Barabaschi and P. Noll, "Effects of Vertical Plasma Displacement and Disruptions on Internal Structures in JET", Proceedings of the Workshop on Electromagnetic Forces, Karlsruhe, Germany 1992.

[6] M.A. Pick, P. Noll, P. Barabaschi, F.B. Marcus, L. Rossi, "Evidence of Halo Currents in JET", 14th IEEE/NPSS Symposium on Fusion Engineering (1991) p 187.

[7] K. Masaki, T. Ando, K. Kodoma, T. Arai, Y. Neyatani, R. Yoshino, S. Tsuji, J. Yagyu, A. Kaminaga, T. Sasajima, Y. Ouchi, T. Koike and M. Shimizu, J. Nucl. Mater. 220-222 (1995) p3 90.

[8] E. Bertolini, M. Buzio, P. Noll, T. Raimondi, G. Sannazzaro and M. Verrecchia "Engineering Analysis of JET Operation", these proceedings.

same octant scaled by the averaged R1 vs. R2 signal is shown. This disruption was typical of the majority of disruptions in that there seemed to be more current collected on the even numbered octant positions. This systematic toroidal asymmetry is not believed to be a result of asymmetric halo current, but due to asymmetric shadowing of the tiles. If the halo current is flowing along field lines in

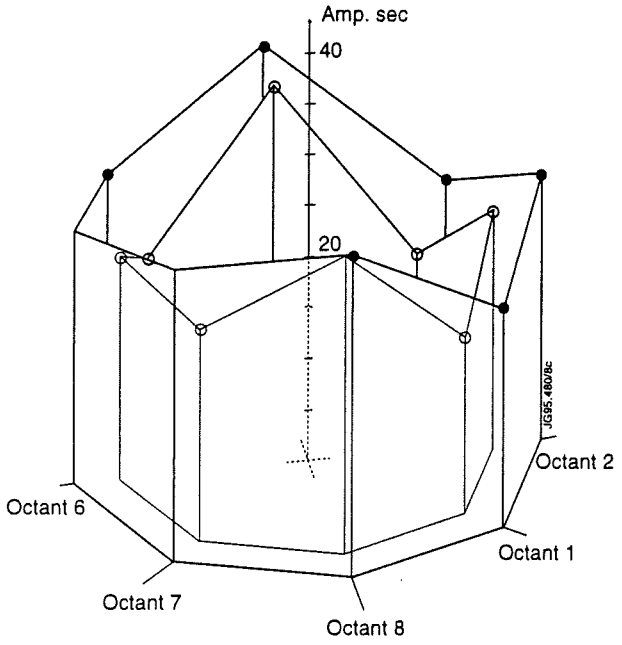

Fig. 4 The time integrated mushroom tile currents for pulse No. 34250 mapped out toroidally.

a vertically displaced plasma, then look at the ceiling of the torus (Fig. 2), current would approach a mushroom tile flowing counter-clockwise with a radially inward twist. The tiles at the toroidal position just before the mushroom tiles are laid out in a slightly different way in the odd octants than the even octants. The data suggests that the layout of the tiles in the even octants shadows the instrumented tiles to a higher degree than in the odd octants. Typically the current collected in the even numbered octant positions is 50% higher than in the odd positions.

Apart from this systematic asymmetry the majority of disruptions show a high degree of toroidal uniformity (within ~ 20%).

There are, however, exceptional cases in which there is a pronounced toroidal asymmetry. The example in Fig. 5 is typical of the observed asymmetry; the integrated mushroom tile current varies approximately sinusoidally with toroidal position, with a period of unity and a zero offset. In this example, the measured currents were originally symmetric, but then dropped to zero at different times for the different positions. Other cases exist, however, where the mushroom tile currents are asymmetric throughout the disruption and the integrated current is negative in some octants.

The disruptions where the halo current is observed to be non-uniform are consistently associated with toroidally asymmetric displacement of the vacuum vessel [8] which indicates the presence of asymmetric forces. It was also observed that the average integrated halo current tended to be highest during these asymmetric disruptions, although the plasma current was not higher in these disruptions.

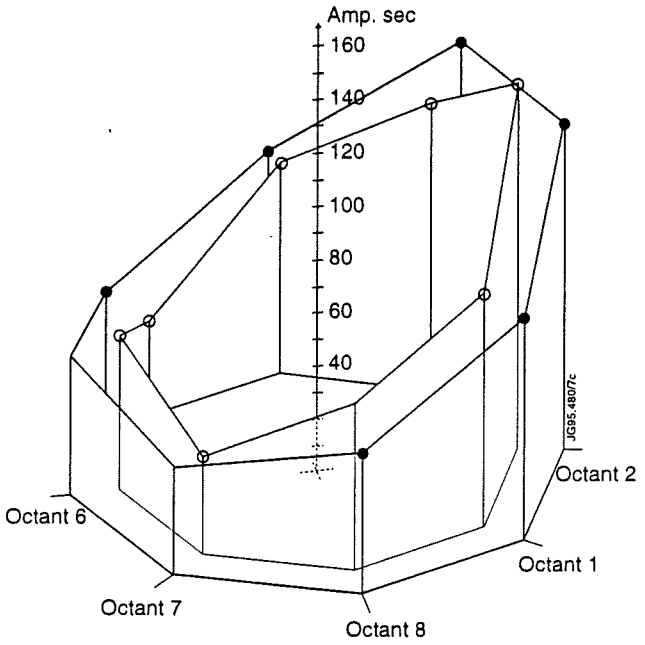

Fig. 5 The time integrated mushroom tile currents for pulse No 34078 mapped out toroidally.

ESTIMATE OF THE HALO CURRENT WIDTH

Fig. 6 shows the average measured halo current per tile for the toroidally symmetric disruption illustrated in Fig. 3. The region where the current is attached to the walls sweeps across row R1 then row R2.

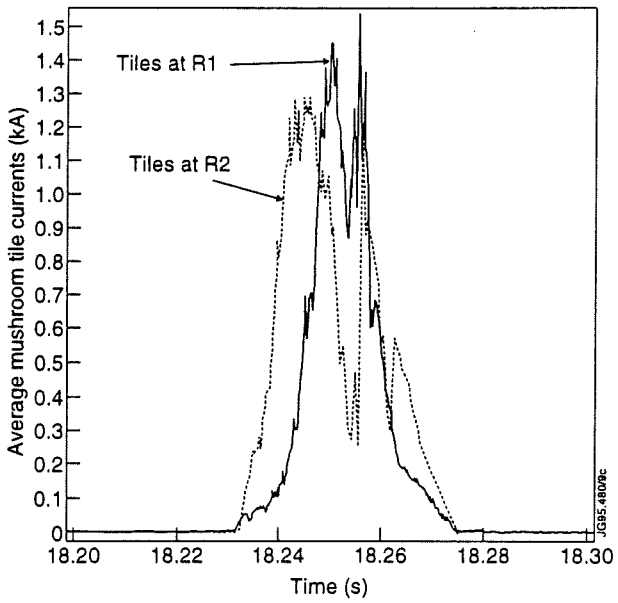

Fig. 6 The mushroom tile currents at poloidal positions R1 and R2 averaged over the different toroidal positions.

The TF Ripple Experiment

Modification of the JET Toroidal Field System

M. Huart, D. Chiron, P. Doyle, V. Marchese, G. Sannazzaro,
P. G. Smith, B. Tubbing, G. Zullo
JET Joint Undertaking, Abingdon, Oxon OX14 3EA, U.K.

ABSTRACT

The interleaved structure of the TF coils allows to obtain a programmable TF ripple field by feeding the two sub-sets of the TF coils with different currents. This would allow to vary the ripple field within one JET pulse and allow a direct assessment of the increased ripple on confinement time, fast particle losses, plasma rotation and H-mode. The TF ripple experiment (RIPPLE 2) was carried out in the Pumped Divertor configuration in conditions relevant to ITER. In this configuration, the normal field ripple at the plasma edge is about 0.1%. In the experiment, the ripple field was varied up to 2% at the plasma edge, the plasma current was typically 2-3MA and the TF field 2-2.5T.

I. INTRODUCTION

The JET Toroidal Field Power Supplies [1] comprise of a flywheel generator with two series connected diode rectifiers (TFGC) and two mains driven transformer-thyristor rectifiers (TF-SU1/TF-SU2) symmetrically arranged. The mid-point of the TFGC diode rectifiers is grounded via a high impedance resistor.
The JET Toroidal Field Coils (fig. 1) comprise of two sub-sets of 16 coils, interleaved with upper and lower terminals, with two compensating busbars for the upper and lower terminal connections.

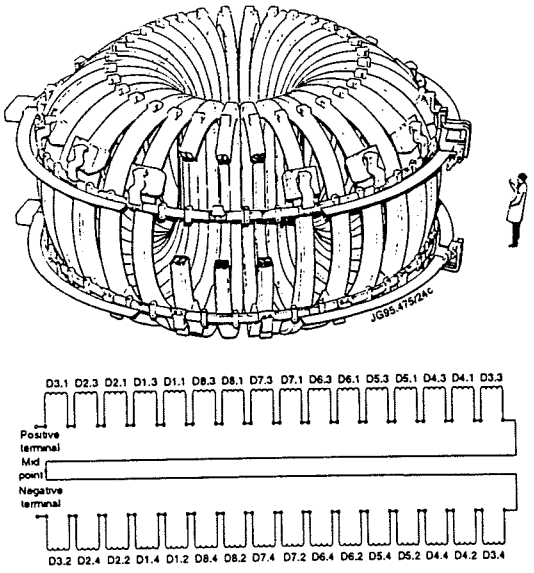

Fig 1. 3D Overview and electrical schematic diagram of the JET 32 TF coils.

II. NEW TF CIRCUIT CONFIGURATION

The Toroidal Field Coil System was designed with a mid-point busbar with current carrying capability for the operation with 16 coils (fig 1.). Whereas the TFGC diode convertors have indeed a mid-point (fig. 2a), a differential current cannot be maintained in the two stator windings since it will produce an overheating of the rotor damper cage. Therefore, the Toroidal Field Power Supplies need to be re-arranged in an asymmetric configuration (fig. 2b) with a new neutral busbar designed to carry the rated imbalance current (table 1). The change of configuration is achieved by new busbars and bolted links.

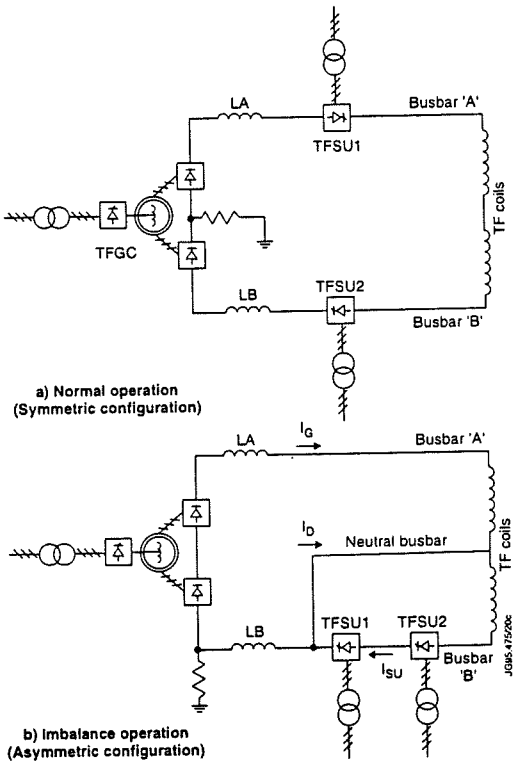

Fig 2. Configuration of the TF Power Supplies

TABLE 1 - SCENARIO OF RIPPLE 2 EXPERIMENT

SCENARIO NO. 1:	SCENARIO NO. 2:
Toroidal Field : 2.5T	Toroidal Field : 2.0T
Average TF current : 50kA	Average TF current: 40kA
Imbalance TF current: 30kA	Imbalance TF current : 40kA
TF Ripple δ : 0.3 x δ_{16}	TF Ripple δ : 0.5 x δ_{16}
Maximum duration of the imbalance current: 10s	

III. FAULT ANALYSIS - CONTROL FAULTS

In the imbalance configuration of the TF circuit (fig 2b), the two sets of 16 TF coils are supplied from different power supplies. In view of the strong coupling between the two sub-sets of coils (interleaved structure) a fault involving the freewheeling of one power supply will lead to a rapid increase of the current in the "healthy" loop (up to twice the average current). Control faults can therefore be severe and needed proper analysis. Three fault scenarios were identified, all three occurring at the end of the TF current rise (TFGC output voltage is highest):

scenario no. 1: the TF-SU1/TF-SU2 output voltages go to zero (freewheeling). The negative imbalance current is detected and trip the flywheel generator (normal operation, $I_D \geq 0$)

scenario no. 2: as scenario no. 1, but the protection fails. When the current detected by the TFC-DCCT exceeds 55kA, the flywheel generator is tripped on DC overcurrent (fig 3).

scenario no. 3: the FGC-DCCT fails (output to zero). The control loops react by exciting the TFGC and de-exciting the TF-SU's. When the current, detected by the FGC ACCT's, exceeds 70kA (DC equivalent), the flywheel generator is tripped on AC overcurrent.

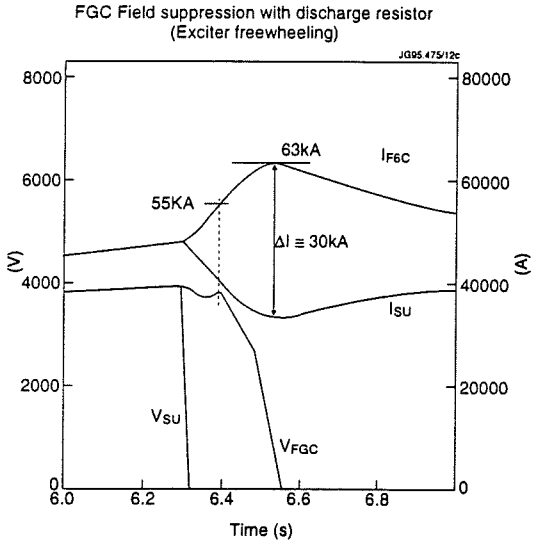

Fig. 3 Fault Scenario no. 2: loss of TF-SU1/TF-SU2 (freewheeling) during TF current rise

IV. OVERVIEW OF CONTROL AND PROTECTION SYSTEM

A. Control System

In the Ripple-2 Experiment, the TF currents are best defined by two variables, namely the TF coil average current (I_{AV}) and the TF coil imbalance current (I_D). The average current defines the magnetic field on axis (B_T) while the imbalance current defines the ripple (δ) defined as amplitude of the field perturbation.

We have $\frac{\delta}{\delta_{16}} = \frac{I_D}{2I_{AV}}$ $(0 < \frac{\delta}{\delta 16} < 0.5)$, δ_{16} = pure 16 coils

In view of the different time response of the power supplies and the different time constant of the circuits (table 2), the control system was designed as two separate control loops (fig. 4); the TF average current loop controls the TFGC and the TF imbalance current loop controls the TF-SU1/TF-SU2.

TABLE 2 - CIRCUIT CHARACTERISTICS

1. MAIN CIRCUIT (AVERAGE CURRENT)	2. IMBALANCE CIRCUIT (IMBALANCE CURRENT)
- INDUCTANCE : 660mH	- INDUCTANCE (CALC.) : 9.5mH
- RESISTANCE : 62 mΩ	- RESISTANCE:: 16.5 mΩ
- TITLE CONSTANT: 10.6S	- TIME CONSTANT: 0.6s

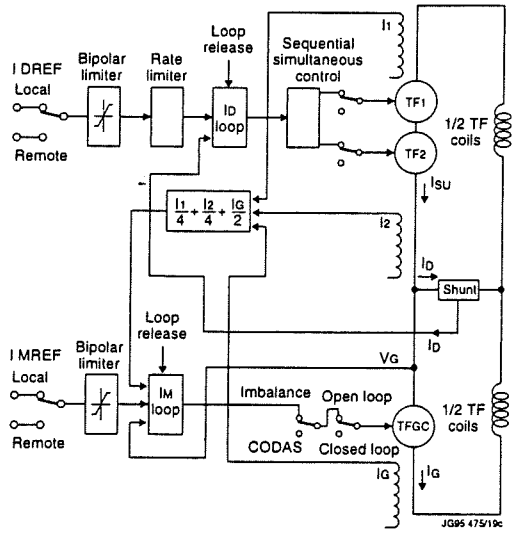

Fig. 4 Control loops for TF average current and imbalance

B. Protection System

B.1. TF Load Interface Cubicle. Control faults can have severe consequences. Hence the need to integrate the control and associated detection/protection system into one single equipment. The TF Load Interface Cubicle was designed for this purpose.

The hardwired protection logic (fig. 5) is designed to coordinate the protection actions between the three power supplies, TFGC, TF-SU1 and TF-SU2. Three levels of protection actions are foreseen (action levels).

B2. Coil Protection System (CPS) The TF measurements for the coil protection system was changed to be consistent with the new circuit configuration. Likewise, the settings of overcurrent trips were set as I1A = 55kA (+5%, + 10%) and I1B = 65kA (+5%, +10%). In addition, the model of the TF circuit, built-in within CPS, was changed from a

one circuit to two circuits equation. This model computes coil voltages from measured currents and compares with the measured voltages and trips once a discrepancy is detected.
Most faults have two detection levels corresponding to the protection action level 2 and 3.

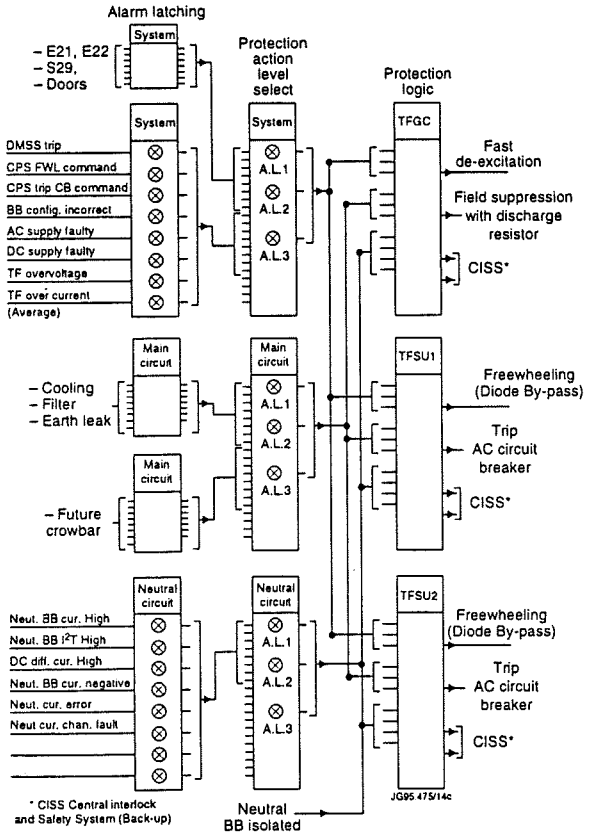

Fig. 5 Hardwired Protection Logic

V. ANALYSIS OF STRESSES IN THE TOROIDAL FIELD COILS

A. Operation With Imbalance Current

A.1. In-plane loads. The stresses in the TF coils were calculated for the two scenarios defined in table 1. Fig. 7 and 8 show the operating points of scenarios no. 1 and 2, respectively axial stress and shear stress, due to in-plane loads only. They are compared with the operating points corresponding to normal operation at 3.45T and to the operation with 16 coils only (Ripple-1 experiment).
From fig. 7 and 8, it is clear that scenario no. 1 has higher axial and shear stress than scenario no. 2.
A2. In-plane and out-of-plane loads. The total axial and shear stress was calculated for scenario no. 1. The maximum values obtained are:
- axial stress (copper) : 66 MPA (<100 MPa)
- shear stress (insulation) : 9.5 MPa (<15MPa)

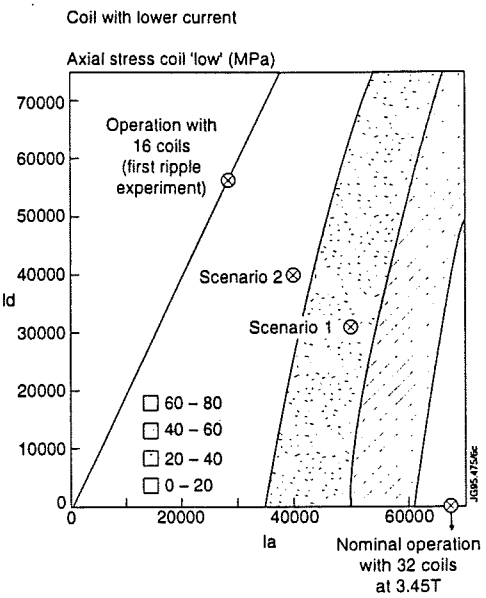

Fig. 7 Axial Stress in TF Coils with variable imbalance current (in-plane loads only)

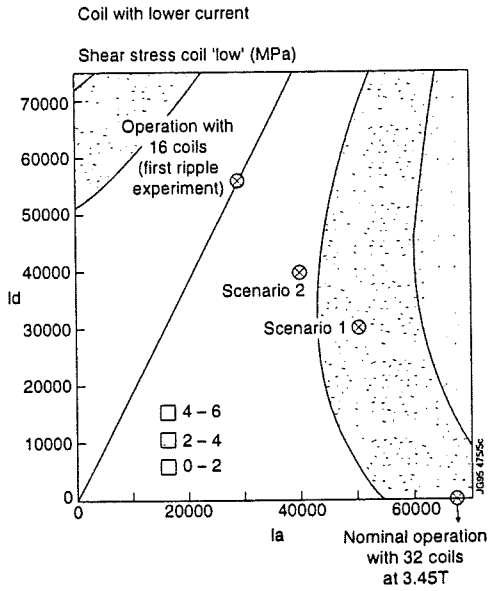

Fig. 8 Shear stress in TF coils with variable imblance current (in-plane loads only)

B. Fault Scenarios

Table 3 summarises the maximum fault currents calculated in the three faults scenario no. 1, 2, 3 (see III above) and for three cases of FGC trips, namely:
a. full inversion of FGC exciter (field inversion)
b. freewheeling of FGC exciter and insertion of discharge resistor in excitation circuit (field suppression)
c. failure of exciter to freewheel followed 100ms later by insertion of discharge resistor.

TABLE 3 - FAULT CURRENTS

Fault Scenario	1a	2a	2b	2c	3b	3c
TFGC Peak Current (kA)	57	59	63	69	76	80
Imbalance Peak Current (kA)	-20	-25	-30	-42	-57	-63

Table 4 summarises the maximum stresses. It should be noted that, as a result of the simulation of the control faults (reported in III above), the following measures were implemented:

a. measurements of the imbalance current (with current shunt) instead of computation from the difference of the FGC/TFSU currents
b. detection of negative imbalance current and trip set at -5kA
c. detection of error $e = I_{SU} - I_{FGC} - I_D$ (imbalance current error) and trip set at 5kA absolute
d. detection of error $e = I_{DREF} - I_D$ (imbalance current error) and trip set at 10kA absolute.

TABLE 4 - MAXIMUM STRESSES IN FAULT CONDITIONS

FAULT SCENARIO	INTERTURN SHEAR STRESS (MPa)	TENSILE STRESS IN COPPER (MPa)
2c	10	85
3b	12	106
3c	13	121

To obtain the fault currents calculated in scenario no. 3 would require the simultaneous failures of protections b,c and d above.

VI. EXPERIMENTAL RESULTS

A. Power Commissioning

The power commissioning included live tests of the protection system during the TF current rise phase. These tripping tests allowed to verify the simulations results reported under III above. The experimental results show that the peak value of the imbalance current is larger than expected, even after correction of the simulation to take account of the actual FGC speed.

Good corrolation of experimental and simulated results were obtained by increasing the mutual inductance from 153 mH to 156 mH. The inductance of the imbalance circuit (table 2) is correspondingly reduced from 9.5mH to 8.0mH.

These new values were used to update the fault currents given in table 3. These are shown in table 5 (old values shown in bracket).

TABLE 5 - FAULT CURRENTS
(WITH CORRECTED COEFFICIENTS)

Fault Scenario	2a	2b	2c	3b
TFGC Peak Current (kA)	62 (59)	66.5 (63)	71 (69)	80 (76)
Imbalance Peak Current (kA)	-29 (-25)	-37 (-30)	-45 (-42)	-64 (-57)

B. Ripple-2 Experiment

The Ripple - 2 Experiment was carried out with JET in the Pumped Divertor Configuration. In this configuration, the edge ripple (δ_{32}) is about 0.1%. The toroidal field circuit was operated with a variable imbalance current to produce a N = 16 ripple component. The edge ripple was varied up to 0.5 x δ_{16} (equivalent to about 2%).

With NBI injection, loss of plasma energy of the order of about 5% were measured while the plasma rotation was reduced by a factor 2 with a 1% ripple. These losses appear somewhat larger than expected on the basis of classical theory.

The ripple field had some peculiar effects on the H-mode. While with a ripple field of 1% a small improvement in H-mode performance is obtained (elm behavior), a degradation of the H-mode performance was observed with a ripple field of 2%. The H-mode threshold is somewhat lowered in the presence of a ripple field (fig 9).

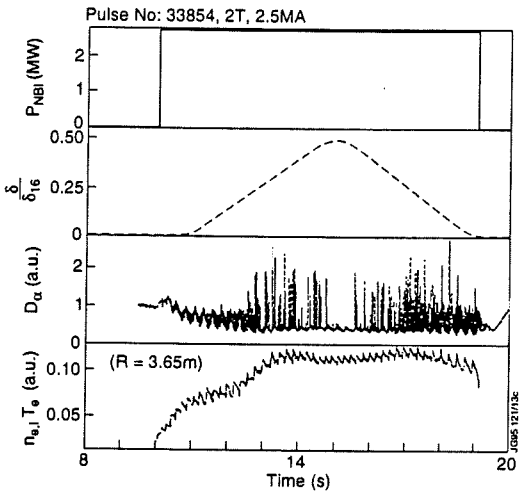

Fig. 9 Effect of varying ripple on H-mode, with PNIB near the threshold.

ACKNOWLEDGEMENT

The authors wish to thank the Chief Engineer, Dr. E Bertolini, for his leadership in coordinating the studies on the fault scenarios in this new configuration of the TF circuit.

REFERENCES

[1] E. Bertolini et al, *"The JET Magnet Power Supplies and Plasma Control System"*, Fusion Technology, Volume 11, Number 1, pp71-119.

[2] B J D Tubbings et al, *"Experiments with Toroidal Field Ripple in JET"*, Proceedings of the 22nd EPS Conference on Control Fusion and Plasma Physics, Bournemouth (UK), July 1995 (to be published).

PERFORMANCE OF THE JET PUMPED DIVERTOR CRYOPUMPSYSTEM

W. Obert, K. Barth, L. Herblin[1)], C. Mayaux, G. Saibene, E. Thompson
JET Joint Undertaking, Abingdon OX14 3EA, UK, [1)] CERN Geneva CH

ABSTRACT

An integrated chevron type cryopump system for the JET pumped divertor program consisting of two independent 180° elements has been operational at JET since mid 1994. The pumping speed of the pump in situ in the torus is ~200000 l/s being limited by the conductance of the water-cooled high heat flux elements in front of the cryopump. The LN shield provides a high pumping speed for impurities such as water and hydrocarbons. An Argon spray facility enables the deposition of Argon frost directly onto the cryopump and to pump He-gas by cryosorption. The pumping speed for He has been found to be nearly the same as for D2. The operation of the pump has been very stable and unaffected by all kind of plasma operation conditions, disruptions or deposition of large quantities of Argon. The operation of the cryopumps was so beneficial for the vacuum and series of experimental programs that cryopumps were kept practically in permanent operation during the full 94/95 experimental campaign.

INTRODUCTION

A key component for the success of the Pumped Divertor (PD) programme of JET [1] were the new two in vessel PD cryyopump systems which have been routinely used to provide high performance active pumping during plasma pulses. The operation of the PD cryopumps proved to be paramount for series of experiments during the experimental campaign [2,3] as it allowed:

- achievement of a torus vacuum with negligible impurity content with the consequence that the PD cryopumps were routinely used for vacuum conditioning together with Glow Discharge Cleaning and Be-evaporation;
- demostration of density control of the plasma;
- achievement of the longest steady-state H-mode (20sec) at JET;
- production and operation of detached plasmas;
- the production of plasmas with highest fusion performance at JET;
- the study of helium transport and removal of plasma exhaust particles;
- thr study of radiative divertor H-modes.

II SET-UP OF THE JET PD CRYOPUMPS

The design of the JET Pumped Divertor cryopump system and its cryosupply system has been described elsewhere [4,5]. There are two independent 180° cryopump segments with separate cryosupply installed at the bottom of the torus (see **Fig.1**) and integrated into the Pumped Divertor structure. The total length of the two systems is ~ 20m, the height is ~ 0.3m. The cryopumps have been designed to be protected against the hot torus (operated at up to 300°C) and the 45 MW plasma power (20 MW of it nuclear power in the DT phase) by water cooled structures.

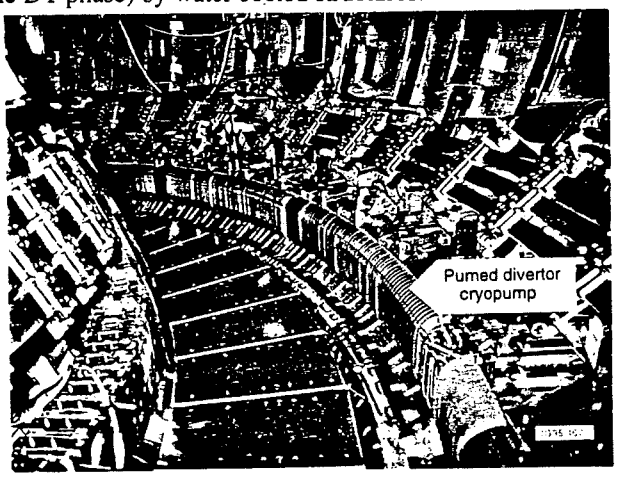

Fig. 1 The in-vessel cyopump for the JET pumped divertor as installed at the bottom of the torus before the installation of the high heat flux elements

The new divertor structure with its integrated cryopump system and the main conductances and pumping speeds are shown in **Fig.2**. The main elements of the cryopumps are the cryocondensation panel cooled by supercritical (sc) helium at 2.7 bar, consisting of six staggered slightly corrugated thin wall stainless steel tubes with 20mm diameter connected in series, liquid nitrogen cooled chevron baffle and solid stainless steel backpanel with 20mm diameter cooling tubes.

Argon spray facility: Helium gas cannot be pumped by cryocondensation but by cryosorption on 4K Argon frost. A special feature of the PD cryopump systems is an integrated Argon spray facility (see **Fig.2**) which consists of four thin wall (0.1mm) stainless steel tubes with 8mm diameter. At 22.6mm intervals (between each chevron) a 0.1mm hole which has been produced by laser drilling. The thin wall tube and the shape of the hole have been chosen to give a flow pattern close to a cosine distribution and to avoid the production of a direct narrow beam. This system allows the direct spraying of Argon onto the 4K Helium surfaces and reduces the Argon load to the torus walls. The Argon pressure inside the tube is < 100 mbar in order to avoid freeze up of the Argon inside the tubes which are at a temperature close to that of liquid nitrogen.

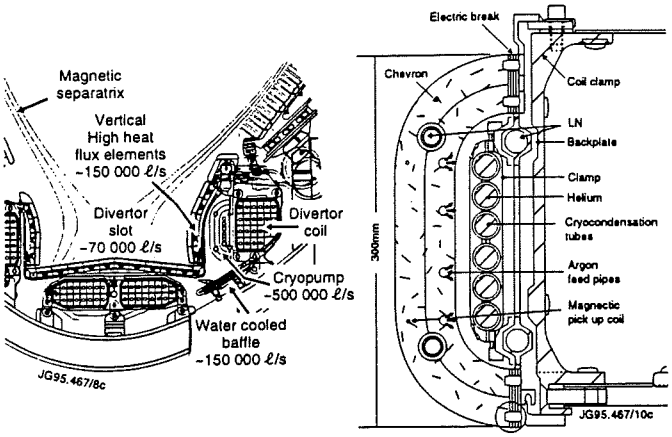

Fig. 2 Set up of the JET Pumped Divertor cryopump system and the main conductances and pumping speed of the JET Pumped Divertor Cryopumps.

III PUMPING SPEED

The pumping speed of the PD cryopumps has been measured by steady state and dynamic analysis by admitting gas pulses into the torus and determined by the ratio of the equilibrium pressure to the mass flow, by the decay time of the torus vacuum pressure and by comparison with gas pulses pumped only with the torus turbomolecular pumps (S ~10 000 ls), which eliminates the problem of calibration of pressures, flows and/or torus volume.

A Deuterium

Figure 3 shows typical pulse traces for 5s Deuterium pulses with and without running cryopump, for one and two pumps operating and with and without torus turbo-molecularpumps operating.

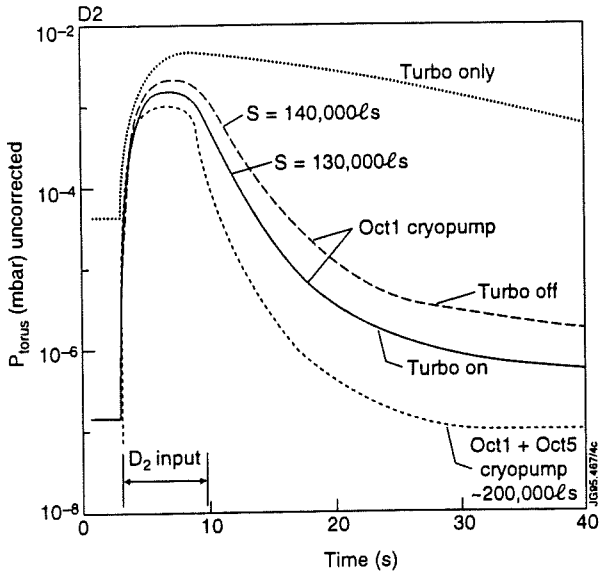

Fig. 3: Torus pressure as function of time during and after 5 s Deuterium pulses under different pumping conditions

The results of the various evaluations show that the pumping speed S of the PD cryopump towards the torus is

S ~ 200 000 l/s (for D_2)

or ~ 20 times higher than that of the installed turbo-molecular pumps. The 1/e pump down time of both PD cryopumps is

τ ~ 1 second for D_2

B Hydrogen pumping

Fig. 4 shows the vacuum traces for *hydrogen* pulses with both PD cryopumpsystems running and with and without torus turbomolecular pumps operational. It can be seen that the PD cryopumps provide practically no pumping for hydrogen due to the high vapor pressure of H_2 at the operation temperature of the supercritical helium loop.

The cryopump stays stable without signs of a uncontrolled regeneration during extended periods (>20 min) at 10^{-4} mbar H_2 pressure. H_2 plasma operation with the sc helium cooling is therefore possible but without the benefit of the high pumping speed of the PD cryopump

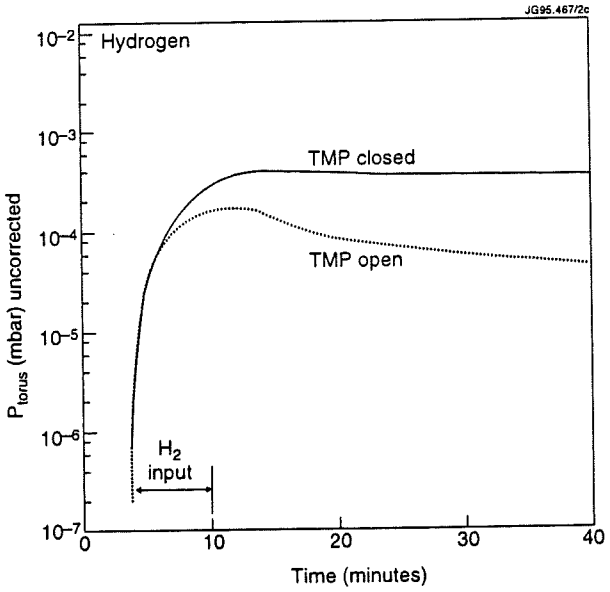

Fig. 4 Torus pressure as function of time during and after 5 sec. hydrogen gas pulses with and without torus TMP system pumping

C Helium Pumping and Argon Frost

1) Argon frost: Typical torus pressure traces during Argon seeding are shown in **Fig.5**. The Argon gas introduction allows a constant Argon seeding in the flow range of up to 200 mbarl/s.

The curves in Fig. 5 show the good performance of the Argon Gas Introduction and the stable consant flow rates for unlimited time periods. This is due to the high

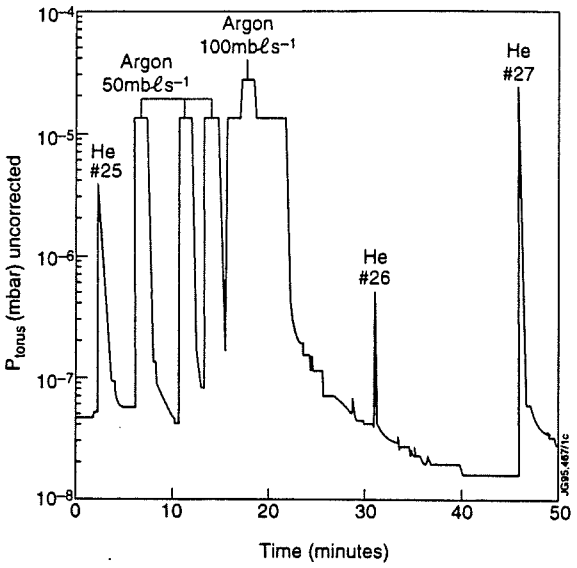

Fig. 5 JET torus vacuum as function of time during series of typical Argon seedings and subsequent helium pulses.

performance pressure reducer used in the system. Using the spray facility gives a torus pressure which is a factor of 25 smaller than by seeding via the torus.

There is a slow tail of base pressure with increasing Argon load after the end of the Argon seeding probably caused by the hold-up in the torus carbon tiles.

The heat load from Argon seeding (~40 W, up to 100s) is not noticeable on the cryopump temperatures

2) Helium pumping: Cryopumping tests of Helium gas condensed on Argon frost are shown in **Fig. 6.**

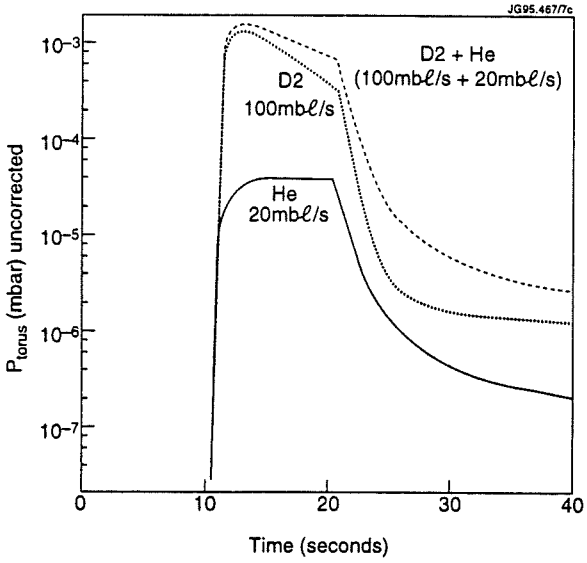

Fig. 6 JET torus vacuum as function of time during a 10 s gas pulses with Deuterium, Helium and a mix of Helium and Deuterium (20:80) with fresh Argon frost layer

The results of the helium pumping tests can be summarized as follows:

The pumping speed with a fresh Argon frost layer is 80% of the pumping speed with D_2 cryocondensation for helium and for D_2/He mixture (80/20). The deterioration of pumping after several He-pulses requires regular reloading of Argon. It was also found that the pumping speed does not change whether the pumps are operated with liquid or supercritical helium.

The plasma operation requires conditioning pulses due to hold up of He on Carbon tiles as the first pasma pulse after Argon seeding ended often with a disruption.

The Ar/He ratio used was 25:1 and there was an additional 5 bar l Ar predeposit for a uniform Argon layer on the $7m^2$ cryosorption surface.

IV TORUS VACUUM

Effect of helium: Fig. 7 shows the effect of closing the torus tirbomolecular pumps when the PD cryopumps are running with sc helium.

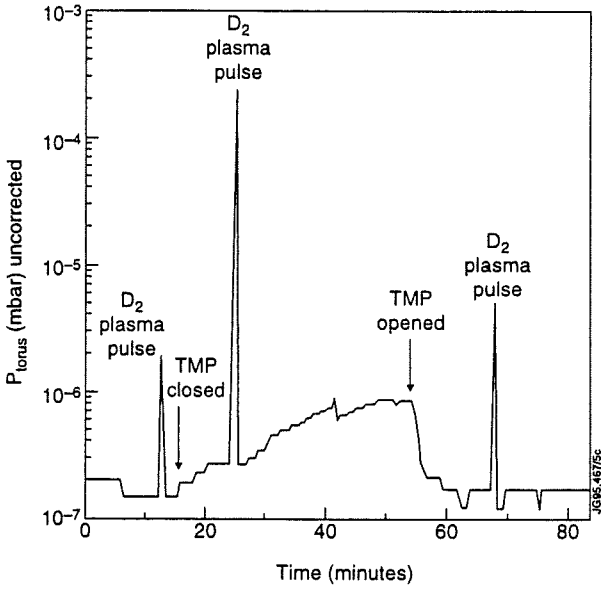

Fig. 7 Torus pressure as a function of time with operational PD cryopumps and with open and closed torus turbomolecular pumps

The pressure of the torus is dominated by hydrogen which will not be pumped below 10^{-6}mbar by the 4K cryosurfaces (see hydrogen pumping). The base pressure of the torus vacuum with baked vacuum vessel (>250°C) is between 10^{-7} and 10^{-6}mbar depending on the history of the vessel conditioning and the operation of the cryopump has only a small effect on the torus end pressure once the torus walls are fully conditioned. The corresponding hydrogen outgassing rate is the range of 10^{-2} to 10^{-3} mbar ls^{-1}.

In addition the torus vacuum has a negligible level of impurities with PD cryopumps running at ScHe temperatures.

Liquid nitrogen: The LN cooldown reduces the base pressure by more than a magnitude when the vacuum is

dominated by water in cases after pumpdown following an intervention where the torus was exposed to atmospheric air.

The operation showed unexpectetly that the torus vacuum is very sensitive to changes in the LN shield temperature of the PD cryopump. Small temperature changes in terms of cryogenic radiation shielding requirements (i.e. between 90K and 140K) appear to release considerable amount of mass 18 and 28 particles (see **Fig. 8**).

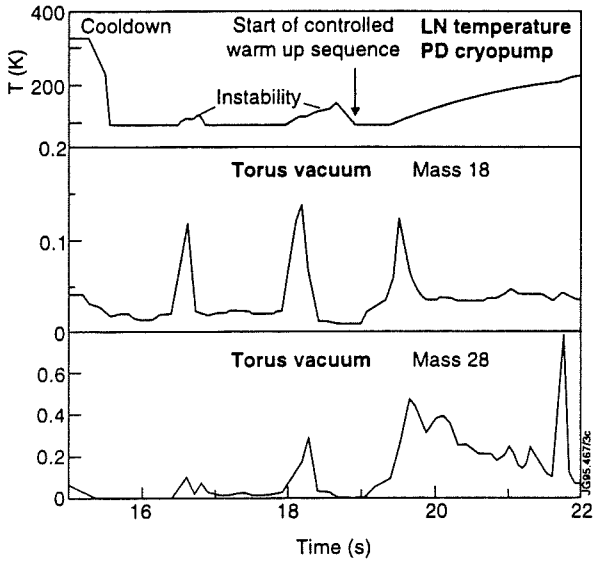

Fig. 8 PD cryopump outlet temperature and torus vacuum mass 18 and mass 28 as function of time during cooldown and warm-up sequences.

V. OPERATION EXPERIENCE

- The operation of the PD-cryopump has been be very stable and reliable (see also [6]).
- Both the PD cryopumps were kept operational practically continuously during the last experimental campaign due to their beneficial effect to the torus vacuum which has negligible impurity levels with the PD cryopumps running ($<10^{-9}$ mb partical pressure).
- The cryopumps had to be regenerated before **Glow Discharge Cleaning** as the helium loop cannot "survive" the high heat load from the thermal conductance due to the base pressure between 10^{-1} and 10^{-2} mbar. However the LN loop was left running during GDC in order to collect the released impurities.
- It is possible to operate the cryopump continuously for over a week without regeneration.
- The hardwired protection against emergency conditions such as water leaks and potential freeze up of water-cooled pipework surrounding the cryopump worked very well.

1) Cryosupply: The supply of the cryopump with supercritical helium proved to be very stable and reliable. No oscillations or flow instabilities were observed.
The forced flow liquid nitrogen supply showed flow instabilities which caused temperature variations between 90 and 140 K. These could be avoided by permanently "overfilling" the LN cryoloop.

2) Instrumentation: The PT 100 sensors of the LN loop worked well. The fully bakeable FeRh sensors for the helium loop drifted during operation. This was not a problem because control of the loop used the temperatures at the plant.

3) Heat Load: The operation of the plasma pulse is not noticeable on the cryoloop temperatures as the loads during D_2 operation without nuclear heating are very small compared to the DT conditions which were taken into account for the design.

VI. CONCLUSION/SUMMARY

- The Pumped Divertor in-vessel cryopump system was a key element for the success of the recent JET experimental campaign.
- The cryopumping system fulfilled its specification and provided ~200 000 l/s pumping speed for Deuterium.
- 80% of the pumping capability was found for He and He/D_2 by cryosorption on fresh 4K Argon frost.
- The thermal load was well within the specification.
- As the system has been designed for a full 45MW plasma with 20MW nuclear power the plasma pulses from the present operation with Deuterium are not noticeable for the cryopump temperatures.
- The cryosupply using supercritical helium as coolant proved to be very reliable and stable in operation.
- The cryopump was used practically constantly throughout the experimental campaign due to its beneficial effect on the torus vacuum.
- The operation during the last 14 months operation showed that no modifications or improvements of the cryopumps will be necessary.

REFERENCES

[1] The JET team (presented by D.Stork) "The New Experimental Phase of JET and Prospects for Future Operation", Procceedings 15th Int. Conf. on Plasma Physics and Contr. Fus. Res., Seville (1994)

[2] The JET team, presented by M. Keilhacher,"JET Results with the New Pumped Divertor and Implications for ITER" to be published in a special issue of Controlled Fusion and Plasma Physics.

[3] G. Saibene et al. "Effects of Active Pumping and Fuelling on Divertor Plasma Discharges at JET" Proceedings of 22nd Europ. Phys. Soc. Conf., Bournemouth (1995) to be published

4] W. Obert et al."JET Pumped Divertor Cryopump", Proceedings of Symposium on Fusion Technology, SOFT 16, London 1990, pp 488-492[

[5] W. Obert "The Liquid Nitrogen and Supercritical Helium Cooling Loop for the JET Pumped Divertor Cryopump" Adv.in Cryogenic Engineering , Vol. 39, pp1569-1576, Edit. P. Kittel, Plenum Press, NY 1994

[6] W. Obert, et al, "Performance of the Supercritical Helium Cooling Loop for the JET Divertor Cryopump, to be phblished in Adv. in Cryog. Eng., Proceeding CEC 1995, Columbus.

THE JET HYDROGEN-OXYGEN RECOMBINATION SENSOR - A SAFETY DEVICE FOR HYDROGEN ISOTOPE PROCESSING SYSTEMS

J L Hemmerich and P Milverton
JET Joint Undertaking
Abingdon, Oxon, OX14 3EA

ABSTRACT

Fusion vacuum systems for processing of deuterium and tritium pose safety hazards by formation of potentially explosive mixtures in case of air inleakage. Early detection of such hazards is essential for the safety of process equipment for fuel purification and recycling. Having established the fact that conventional oxygen monitors do not work well in hydrogen atmospheres at low pressures, we developed a sensor compatible with this duty. It is based on the detection of the oxygen-hydrogen reaction heat in a differential thermoelectric calorimeter, using a proprietary AECL wetproof catalyst for promoting the recombination reaction and semi-conductor thermopiles for detection. Operating at room temperature, the sensor provides signals in excess of 1mV for explosive hydrogen-air mixtures at pressures as low as 1mbar. The differential principle employed suppresses erroneous signals originating from hydrogen sorption/desorption heat on the catalyst.

The design and performance of these sensors will be described in detail.

Two of the sensors have been installed on the main forevacuum lines of the JET device to provide unambiguous alarms in case of air inleakeage. A previously developed (batch processing) oxygen detector reacting a sample in a vessel at 77K by means of a hot platinum filament (-900K) will then be used for exact quantitative assessment of the combustible mixture. Depending on the result, a suitable safe process route will be selected.

INTRODUCTION

The development of controlled thermonuclear fusion to a source of energy involves the handling of the hydrogen isotopes deuterium and tritium at low pressures (10^{-4} to 10 Pa) in the actual reactor and at higher pressures (up to approximately 100 kPa) in auxiliary gas purification and isotope separation systems. Such processes carry the risk of formation of explosive hydrogen/air mixtures, eg by inleakage of air into the low pressure section of the process loop and by subsequent compression to atmospheric pressure. This risk would be aggravated by the release of the radioactive isotope tritium following explosive destruction of a process loop. It is therefore desirable to detect the pressure of oxygen in hydrogen at sufficiently low pressures and concentrations as a warning for dangerous process leaks. Once identified, hazardous mixtures can then be safely purified, eg by selective absorption of O_2 on molecular sieve at cryogenic temperatures. Such procedures, being uneconomic and time consuming, are not normally employed in the process main stream.

EXISTING OXYGEN MONITORING DEVICES

1) *Commercial oxygen detectors*:

A range of commercially available electrolytic O_2 detectors were tested on mixtures of air (1 to 5%) with hydrogen in the pressure range of 0.1 to 1 kPa. In this pressure range, the signals were found to be too low and irreproducible for reliable detection. Furthermore, we obtained information [1], that conventional electrolytic oxygen detectors operating at atmospheric pressure would exhibit erroneous signals when exposed to tritium, requiring frequent sensor replacement.

2) *JET batch recombination sensor*:

This device, described in detail earlier[2], measures the pressure of a gas sample in a sample flask at 77K before and after recombination by means of a platinum filament heated to 600°C. The pressure change observed corresponds to three times the oxygen partial pressure, since H_2O, the reaction product of $2H_2 + O_2$ exhibits negligible vapour pressure at 77K. The main disadvantage of this batch sampling method is the low repetition rate of ~ 5 minutes.

H_2-O_2 RECOMBINATION SENSOR

To avoid the disadvantages of the above described detection devices, a new sensor[3] was developed which is tritium compatible, stable and operates continuously at room temperature. Its principle is shown in Fig 1. It uses a proprietary wetproof AECL catalyst(3) originally developed for tritium sampling devices. The reaction heat is detected by a semiconductor thermopile(2). The thermopile is arranged in a pocket on a vacuum flange(1), the catalyst is retained by wire mesh(4). The signal(10) of the thermopile is a direct measure of reaction heat in the catalyst. A vacuum-tight envelope(5) and pressure gauges, hydrogen and air admission valves and a vacuum pump (6, 7, 8, 9) are used to adjust test mixture composition and flow rate. This device showed good sensitivity to pressures well below 1 kPa for hydrogen with 1 to 4% air, but still suffered from undesirable side effects:

- sensitivity to ambient temperature fluctuations;

- a strong (but quickly decaying) positive (= heat generation) output signal upon admission of pure H_2 or pure air due to the heat of adsorption of gas molecules on the catalyst surface;

- a strong (but quickly decaying) negative (= heat consumption) signal during pumpdown after tests due to the heat of desorption of gas molecules from the catalyst surface.

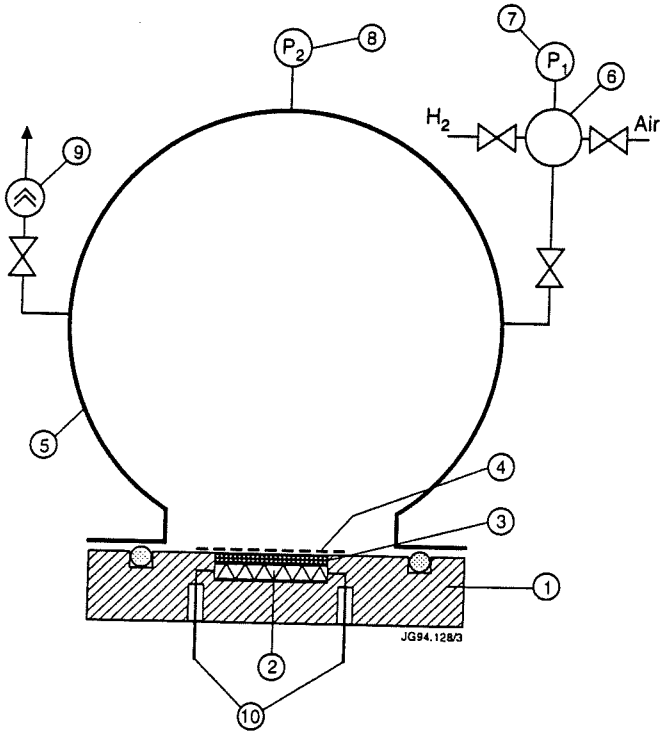

Fig 1 Schematic of single thermoelectric recombination heat detector

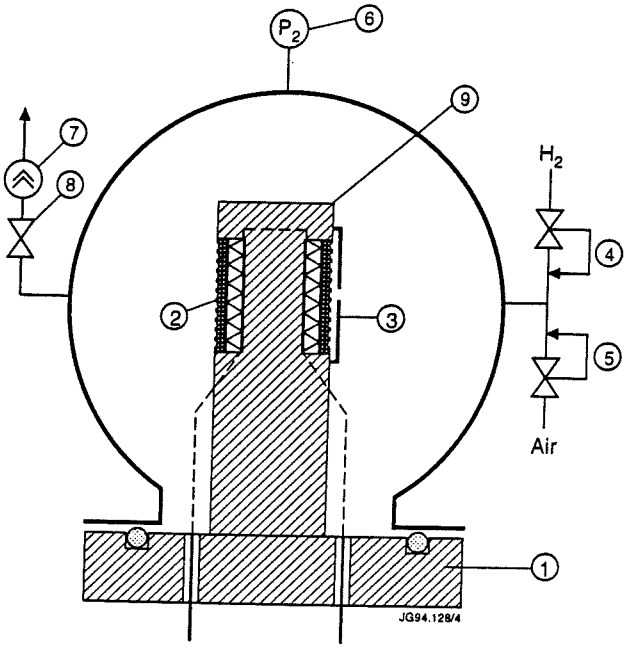

Fig 2 Schematic of differential sensor

DIFFERENTIAL H_2-O_2 RECOMBINATION SENSOR

These disadvantages were overcome by using a differential sensor shown in Fig 2: two identical sensors (2 and 3) are used, their signals being electrically subtracted. The main sensor (2) permits access for the reactant gas mixture over the full surface area of the catalyst, the reference sensor (3) is covered with a mask which reduces the exchange area between reactant gases and catalyst to about 1% of the sensor area. This device exhibits the expected improvements:

- insensitivity to temperature changes;

- in case of pressure changes (gas admission or pumpdown) the pressures of the majority gas in both catalyst pockets and therefore adsorption or desorption heat are virtually identical and hence cancel each other;

- the main sensor admits the reactant minority over the full area, whereas the masked reference sensor signal is two orders of magnitude lower. Hence, this differential sensor shows virtually the same sensitivity as the single sensor but simultaneously suppresses error signals due to temperature fluctuation and gas pressure changes.

Fig 3 shows the final version of the differential sensor: both main and reference sensor are arranged side by side on a 6" OD Conflat® flange, the mask on the reference sensor (nickel foil with 3mm DIA hole) is clearly visible.

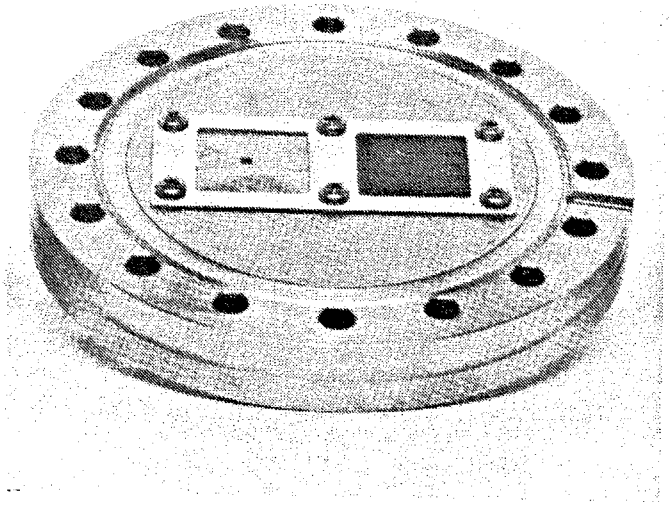

Fig 3 Differential sensor embedded in a vacuum flange

SAFETY HAZARDS OF WETPROOF AECL CATALYST

A quick functional test of this final assembly by puffing hydrogen gas onto the sensor area in atmosphere revealed a serious safety hazard: a short blast of hydrogen was sufficient

to raise the catalyst temperature to ignition; subsequently, the catalyst continued burning in air under development of dense, acrid fumes, with sparks flying through the high transparency mesh screen. In this form the sensor did not appear acceptable for safety reasons, as it could act as an ignition device for explosive gas mixtures.

SAFE DIFFERENTIAL SENSOR

A minor modification remedied this deficiency: a triple layer of low transparency copper wire mesh covering both main and reference sensor fully suppressed ignition upon hydrogen exposure in air. The addition of the copper screens reduced the sensor signal by approximately 50%. However, the signal is still sufficiently strong for unambiguous detection of flammable mixtures.. This sensor is shown in Fig 4. Calibration tests were performed with 1 to 8% air in H_2 and 0.5 to 4% H_2 in air. These results are shown in Figs 5 and 6.

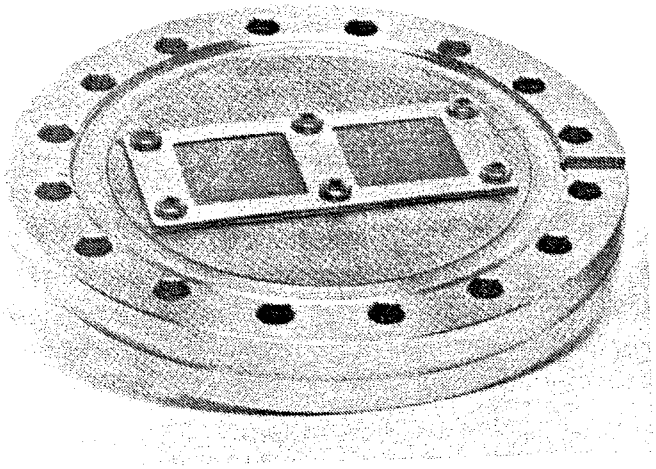

Fig 4 Differential sensor protected with copper mesh

The sensors have been connected to the gas transfer lines between the JET Torus and the Active Gas Handling Systems[4]. The signals are connected to trip amplifiers raising alarms for signals exceeding 1 millivolt. In case of alarms indicating the presence of combustible gas mixtures, the composition of these mixtures is further analysed by use of the previously described batch recombination sensor and, as required, by mass spectrometry and gas chromatography. Depending on composition a safe process route can then be selected.

CONCLUSION

The new differential recombination sensor is suitable for on-line detection of flammable mixtures in hydrogen isotope processing systems in the pressure range from 0.1 to 100 kPa. Two sensors have been installed in the gas transfer lines between the JET Torus and the Active Gas Handling System[4]. In co-operation with R. D. Penzhorn, two sensors will be tested at the Tritium Laboratory in Karlsruhe, Germany, with tritium-air mixtures in the near future.

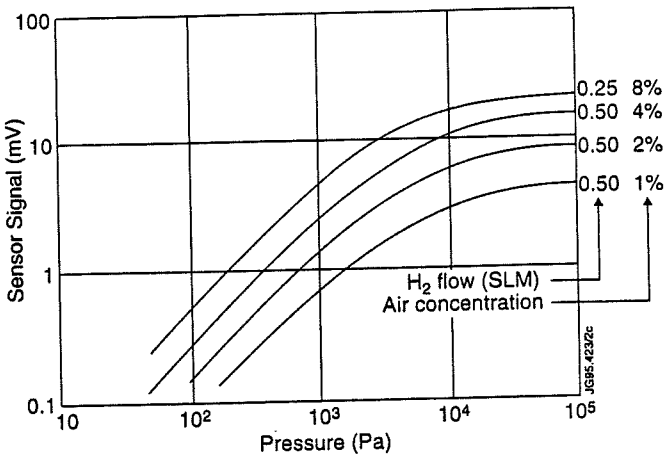

Fig 5 Sensor signal vs pressure for 1 to 8% air in hydrogen flowing across sensor array

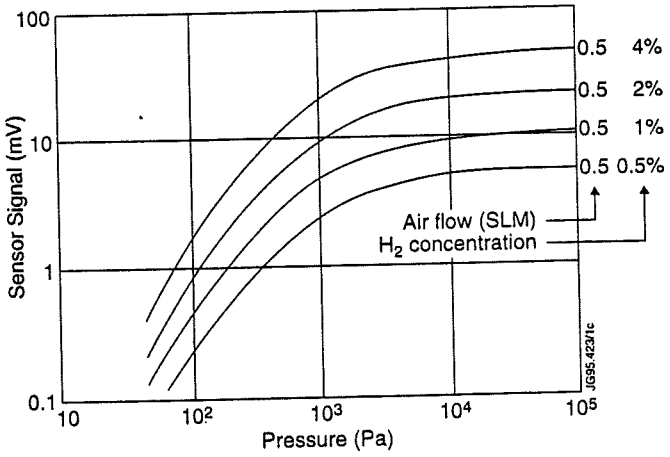

Fig 6 Sensor signal vs pressure for 0.5 to 4% hydrogen in air flowing across sensor array

Due to their high sensitivity at atmospheric pressure, such sensors can also be used to detect traces of hydrogen in air (signal ~ 1μV/ppm H_2). Due to their intrinsic safety feature (no electrical supply voltages required) they can be installed in hazardous areas.

REFERENCES

[1] G. Pautrot, ILL Grenoble, private communication.

[2] R. Lässer, C. J. Caldwell-Nichols, J. Dallimore, B Grieveson, J. L Hemmerich, A. Konstantellos, M. Laveyry, P. Milverton, R. Stagg and J. Yorkshades, "Analytical Equipment for the JET Active Gas Handling Plant", Fusion Technology 21, 406 (1992).

[3] UK and International patents pending.

[4] J. L. Hemmerich et al (many authors), "Installation and Inactive Commissioning of the JET Active Gas Handling System", Proc. 15th Symposium on Fusion Engineering, Hyannis, Ma, (1993), Supplement, pp. 37-41.

TRITIUM AND URANIUM INVENTORY MEASUREMENTS WITH THE JET AGHS PRECISION CALORIMETER

J L Hemmerich, P Milverton, G Newbert, N Green and A Miller
JET Joint Undertaking
Abingdon, Oxfordshire, OX14 3EA

ABSTRACT

The principle of temperature stabilization by inertial feedback control was further developed to provide a stable base for a thermoelectric calorimeter. Noise and long-term drift of the base temperature have been reduced to $\pm 3 \times 10^{-10} Ks^{-1}$. With this temperature stability, samples with large heat capacities, such as Amersham MKIV uranium getter beds for tritium transport and storage (total heat capacity of calorimeter chamber, uranium bed secondary containment and getter bed itself is $1370 JK^{-1}$), can be measured with a reproducibility of $\pm 2\mu W$. During a 14-day campaign, all Amersham getter beds presently held by JET were measured. The bed with the highest tritium content (22,40Ci) was repeatedly measured in 2-day intervals, and the results were found to follow the trend of the tritium decay well within the error band of ±0.4% (±0.3% due to tritium decay heat uncertainty, and ±0.1% due to calorimeter calibration accuracy). Tritium-free getter beds showed a power output of $7.5 \pm 2\mu W$, due to the decay heat of the total sum of all isotopes contained in their depleted uranium inventory of 320g. This compares reasonably well with subsequent measurements on a 4kg depleted uranium test sample of certified composition, procured from British Nuclear Fuels Limited.

INTRODUCTION

Tritium inventory assay by calorimetry offers the advantage of safety: the tritium can remain in its transport container. With this feature and steadily increasing accuracy, calorimetry is gradually replacing the conventional method of measuring pressure, volume, temperature and composition of a gas sample in an assay vessel [1, 2, 3]. The new JET calorimeter represents a major step in this direction with in-situ resolution of 100nW and 7 to 8 decades dynamic range. This performance has been achieved by further development of inertial temperature control [4, 5].

JET PRECISION CALORIMETER

The JET calorimeter contains a sample chamber of ~0.5ℓ useful volume (68mmø, 140mm high) which is connected to a temperature stabilised base through an array of semi-conductor thermopiles. The heat emitted by the sample and flowing through these thermopiles generates a thermoelectric voltage which is directly proportional to the heat flow. A series of calibration runs by electrical heating of a purpose-built resistor inside the sample chamber in the power range from 1μW to 10W established a calibration factor of 0.2914 V/W ±0.1% ±2μW valid for the full power range. The accuracy of ±0.1% covers the sum of all error sources (heat source voltage and resistance measurement, heater power supply fluctuation and calorimeter signal measurement), the short-term signal noise corresponds to ±0.2μW power.

Temperature stabilisation is achieved by inertial temperature feedback control [4, 5] using the heat capacity of 26kg copper connected to the calorimeter base through a separate set of thermopiles.

The whole assembly is placed in a vacuum vessel to suppress heat transfer by conduction and convection. Radiative heat transfer is suppressed by operating the double-walled vacuum vessel on an auxiliary water loop featuring a laboratory standard thermostat and temperature control improved by a combination of a fixed Pt 1000 resistance temperature bridge and another inertial temperature derivative sensor [5]. The water loop is controlled to within $\pm 10^{-3} K$ of the temperature of the calorimeter base. The detailed design of the equipment will be described in the future [6].

The calorimeter together with its control and measuring equipment is shown in Fig 1, and a sample can together with an Amersham U-bed in Fig 2. The sample container fits inside the calorimeter chamber and permits safe handling of getter beds, which after use for tritium storage are always externally contaminated. It also reduces the risk of contaminating the calorimeter chamber.

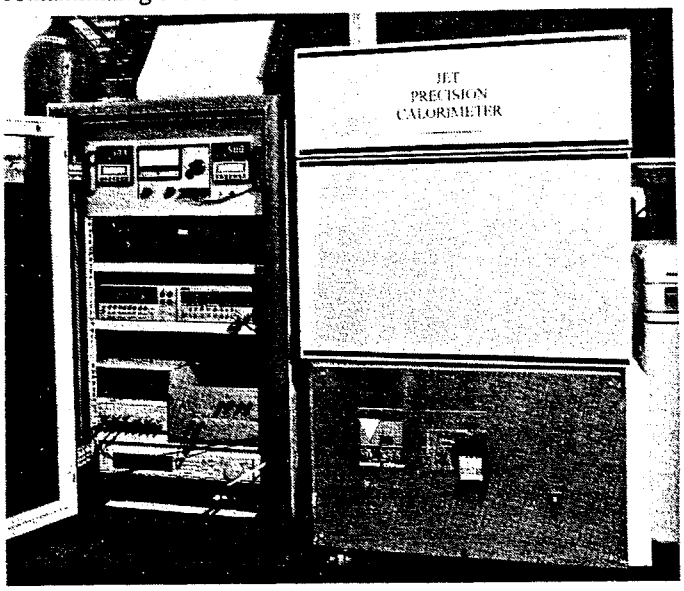

Fig 1 Precision calorimeter

The secondary containment has a lid with an 0-ring radial compression seal. The U-bed is suspended from the lid by means of a bracket sliding over the U-bed valve handle.

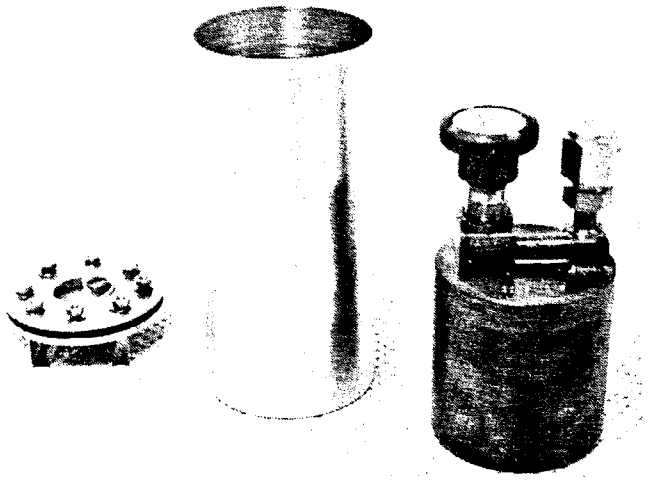

Fig 2 Amersham MKIV Transport U-Bed with calorimeter secondary containment

MEASUREMENTS

During a 14-day period a new sample (getter bed in sample can) was placed in the calorimeter chamber at 6.05am each day and measured the following day by taking a time average over a 1 hour period from 5 to 6am. This was found necessary to obtain ±2μW reproducibility: whereas the calorimeter chamber signal equilibrates with a time constant of 8.7 min, and is within (typically) less than 25μW of the final equilibrium value three hours after insertion of the sample, the final equilibration of temperature changes of the overall assembly caused by venting, sample insertion and pump-down is slower. Typical time constants are 2.5 to 3h. Furthermore, the calorimeter is affected by room temperature fluctuations (day/night temperature fluctuations of ±5°C lead to signal fluctuations of ±5μW). The best temperature stability is obtained over night, where a combination of room heater and standard air conditioning can maintain a room temperature of 20 ±0.5°C. Due to short nights (summer solstice) and variable weather conditions, the results still showed the after effects of ±2°C room temperature variation during the 2 week period.

Table 1 gives the results in chronological sequence.

The results are consistent with the getter bed history: UB4044 and 4045 were only used with deuterium. UB4049 was only filled with deuterium but had been connected to a tritium manifold, where it evidently took up ~0.1 to 0.2Ci tritium. UB4055 was filled with 2.5barl D_2 and 1% T_2, its inventory of 14.34Ci is left over from the JET tritium experiment in 1991. UB4046 was filled with 0.2g T_2; 0.1g were used in the JET tritium experiment in 1991, the remaining 0.1g subsequently removed by evacuating at 450°C.

Table 1

Date	U-bed #	Total Power (μW)	Tritium Inventory*(Ci)
14.06.95	4046	763.7 ± 2	22.44 ± 0.15
15.06.95	4049	14.6 ± 2	0.21 ± 0.06
16.06.95	4046	764.8 ± 2	22.47 ± 0.15
17.06.95	4049	11.4 ± 2	0.12 ± 0.06
18.06.95	4046	763.3 ± 2	22.43 ± 0.15
19.06.95	4045	7.2 ± 2	Uranium Only
20.06.95	4046	762.6 ± 2	22.41 ± 0.15
21.06.95	4044	7.9 ± 2	Uranium Only
22.06.95	4046	760.6 ± 2	22.35 ± 0.15
23.06.95	4055	491.2 ± 2	14.35 ± 0.12
24.06.95	4046	759.2 ± 2	22.31 ± 0.15
25.06.95	4055	490.5 ± 2	14.33 ± 0.12
26.06.95	4046	760.9 ± 2	22.36 ± 0.15
26.07.95	4kg Uranium	61.0 ± 2	Uranium only

*Total power minus 7.5μW (uranium)

The results show further, that in high resolution calorimetry, the decay heat of depleted uranium used as getter material is not negligible: 7.5μW (average from UB4044 and 4055) correspond to a tritium inventory of 0.22Ci. It should be pointed out that the decay heat of "depleted uranium" may vary depending on the separation process, in particular on the residual concentration of U234. This was observed by measuring a 4.000kg sample of depleted uranium procured from British Nuclear Fuels Limited. This sample, with known composition (U238-99.791%, U235-0.208%, U234-0.001%) showed a decay heat of 61.0 ±2μW. For a 320g quantity, this corresponds to 4.9 ±0.2μW. From this observation, it accrues, that in order to obtain ultimate precision, it is recommended to assay a large quantity of depleted uranium prior to filling individual batches into U-beds. The sample can could accept a uranium cylinder with ~8.5kg mass sufficient for ~25 U-beds. This measurement would only marginally increase the cost of U-bed manufacture, but provide a figure on uranium decay heat with a precision of ~±100nW per U-bed.

The U-bed with the maximum tritium inventory (4046 -22.4Ci) was measured every second day and these results are

shown in Fig 3 with a suppressed zero-line and a superimposed error band, based on the average value of the 14 day period and the known tritium decay characteristic [7]. The measured data are well within the error band representing a systematic error of 0.4% (±0.3% tritium decay heat uncertainty [7] and ±0.1% calorimeter calibration tolerance) ±2μW base line fluctuation caused by room temperature changes.

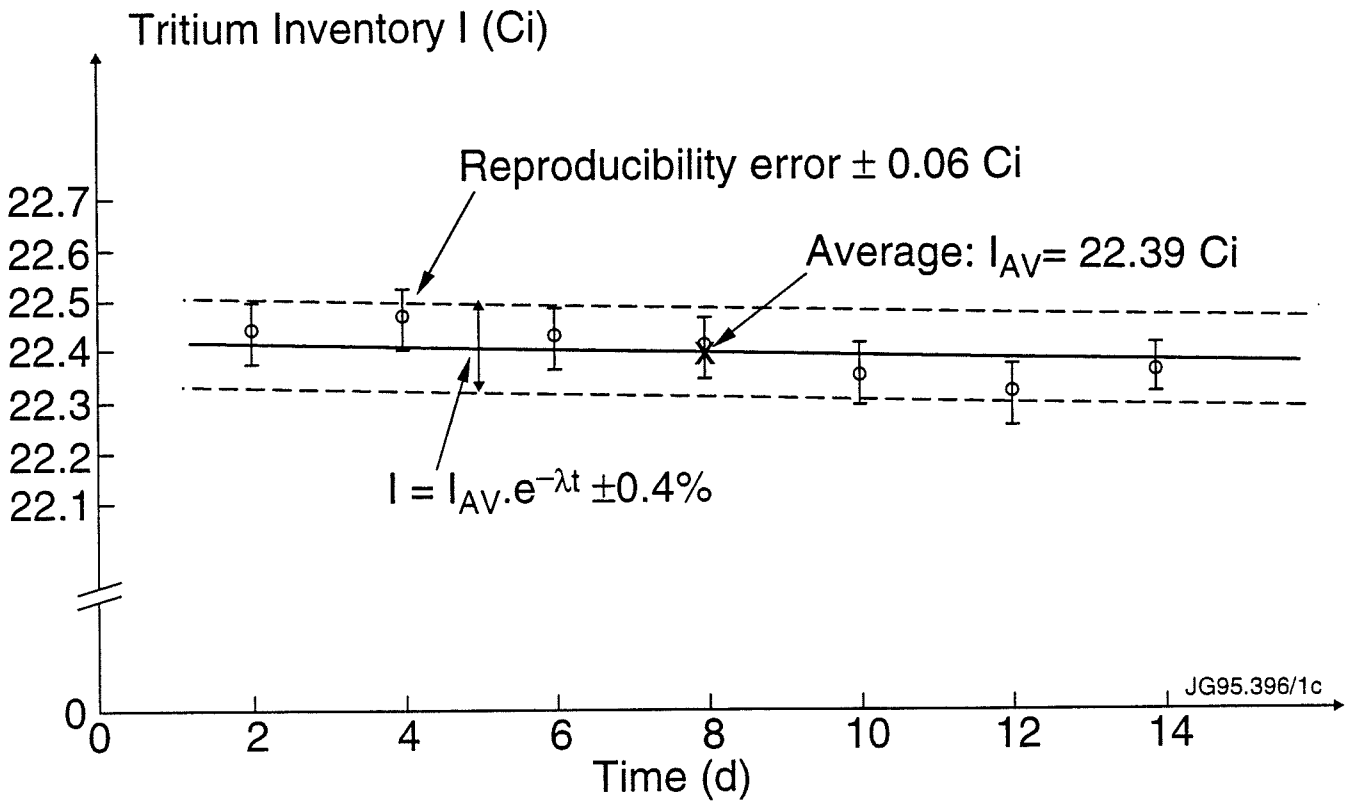

Fig 3 Results of U-Bed 4046 measured in 2-day intervals during a 14-day period. Superimposed is the tritium decay curve derived from the average of all the data and the decay constant from ref [7] with a systematic error band of ±0.4%.

CONCLUSION

The JET precision calorimeter, covering a thermal power range from 1μW to 10W has proven its capability to reproducibly measure samples to within ±2μW power output and an absolute accuracy of ±0.1%, which could be further improved by accurate calibration. At present, however, no further efforts in this direction are deemed necessary, as the basis for all measurements, the tritium decay heat [7] of 0.324W g^{-1} is only known to an accuracy of ±0.3%.

The performance of the calorimeter will be even more impressive at higher inventories: a quantity of 3g T_2 (total output power of 0.972W) will give a calorimeter signal of 283.2612mV, permitting a resolution of 0.35ppm. Irrespective of calibration accuracy, this will enable us to measure the decay constant to 0.2% accuracy in a 24h period or to 0.02% accuracy in a 240h period, as the decay constant measurement is not affected by the systematic errors and a base line stability of ±1μW will be readily achievable under more stable room temperature conditions.

ACKNOWLEDGEMENT

The authors wish to express their thanks to A. C. Bell for continuous support and encouragement.

REFERENCES

[1] H. Kapulla, R. Kraemer, R. Heine, Tritium Inventory Measurements Using Calorimetry, Fusion Technol. 21, 412 (1992).
[2] J. A. Mason, G. Vassallo, Tritium Measurement by Isothermal Calorimetry, Fusion Technol. 21, 425 (1992).
[3] C. R. Walthers, E. M. Jenkins, The Tritium Systems Test Assembly Self-Assaying Portable Uranium Bed, Proc 15th IEEE/NPSS Symposium on Fusion Engineering, Hyannis, Oct. 1993, Vol. I, p57.
[4] J. L. Hemmerich, L. Serio, P. Milverton, High Resolution Tritium Calorimetry Based on Inertial Temperature Control, Rev. Sci. Instr. 65(5), 1994, p1616.
[5] J. L. Hemmerich, P. Milverton, L. Serio, UK and international patents pending.
[6] J. L. Hemmerich et al, to be published.
[7] P. C. Souers, Hydrogen Properties for Fusion Energy (University of California, 1986).

Operation of the 3.7 GHz LHCD System in JET

M.Lennholm, Y.Baranov, J.A.Dobbing, A.Ekedahl, P.Finburg, B.Fischer, C.Gormezano, C.Gowers, A.Kaye, J.Plancoulaine, F.G.Rimini, J.Romero, P.Schild, A.Sips, F.Smits, F.X.Söldner
JET Joint Undertaking, Abingdon OXON OX14 3EA, United Kingdom

ABSTRACT

The Full Lower Hybrid Current Drive (LHCD) system has come into operation in JET during the 1994/95 experimental campaign. 7.3MW has been coupled to plasma, using 8.2MW of generator power. Long pulses with power in excess of 6MW have resulted in a maximum injected energy of 67MJ. Full current drive at plasma currents up to 3MA have been achieved with LHCD alone[1].

INTRODUCTION

The JET LHCD system is supplied by 24 klystrons operating at 3.7 GHz, capable of delivering 12MW for 20 seconds [2]. The launching structure (launcher) consists of 48 multijunctions, each dividing the power into eight 9mm by 72mm waveguides at the launcher-plasma interface [3]. The launcher can be moved radially during JET pulses with a stroke of 150mm, and with a typical response time of 0.3 seconds for a 10mm step [4]. An 80000 litres/second dedicated cryopump is situated on top of the launcher vacuum vessel, and the vessel can be baked at up to 350°C. The key elements determining the achievable coupled power are the conditioning state of the launcher and the reflection coefficient. Full current drive with LH only has been achieved at high power (>6MW) in the range 1-3MA. In conditions close to full LH current drive, sawtooth stabilisation followed in some cases by a strong increase in the central electron temperature has been achieved at 3MA [1].

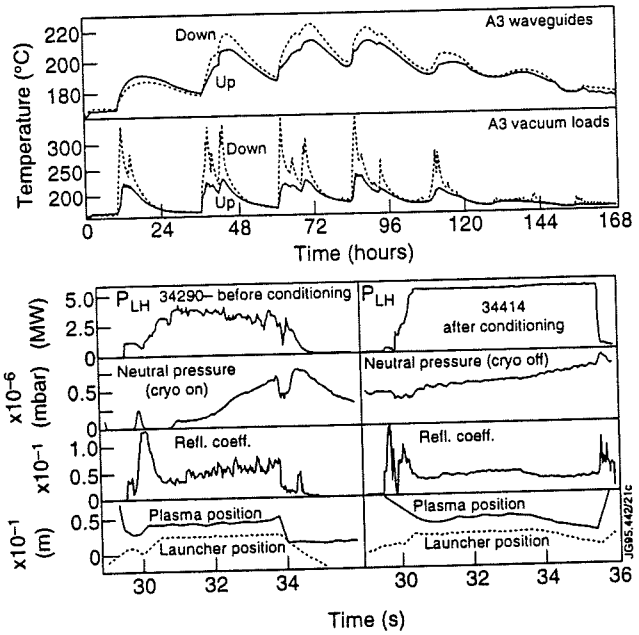

Fig. 1 Conditioning. Top: Temperatures of vacuum loads and multijunctions for 2 multijunctions situated above each other. Both multijunctions are powered by the same klystrons (A3) Bottom left: Shot 34290 (before conditioning). Bottom right: Shot 34414 (after conditioning).

CONDITIONING

In order to improve the power handling capability of the LH-antenna, an extensive programme of conditioning was carried out. The vacuum vessel around the launcher was heated to 350°, and then 3 second pulses of RF-power were applied to the antenna, radiating into vacuum, with a high repetition rate. During this RF-conditioning the temperature of the launcher increased significantly. Fig. 1. shows the result of several days of such conditioning. It is seen that the LH-power was unsteady due to arcs in the multijunctions and that the pressure in the LH vacuum vessel increased strongly during the first pulse, whereas no such problems were seen after the conditioning.

COUPLING

The LH coupling is quantified by the reflection coefficient at the input to the multijunctions. The measured reflection has been compared to the reflection R_c computed by the SWAN code [5]. The reflection coefficient calculated by the code can be approximated in the range from 1% to 30% with very good accuracy by:

$$R_c = \frac{a}{(n_{eL})^b} + c \qquad (1)$$

where a and b depend on the density decay length λ_{sol} in the scrape-off layer (SOL). c gives the minimum reflection that can be achieved. n_{eL} is the electron density immediately in front of the antenna. Introducing a vacuum layer of 0-5mm in front of the launcher in the calculations, results in values of c of 0.2-32%. The above approximation is valid only for plasma densities at the antenna $n_{eL}<1.5\,10^{18}$ m^{-3}. For higher values of n_{eL} the reflection increases for increasing density. In all relevant cases the density at the antenna is low enough for the above criteria to be satisfied and very high densities are required to introduce significant errors. The value of n_{eL} is determined from the following formula.

$$n_{eL} = n_{eLCFS} \cdot e^{-\frac{d_{LP}}{\lambda_{SOL}}} \qquad (2)$$

where: n_{eLCFS} is the density at the last closed flux surface (LCFS). In the experimental results this is taken as 0.4 times the central line average density. d_{LP} is the distance from the LCFS to the launcher, as found from the EFIT boundary reconstruction code and the position of the

launcher. λ_{sol} depends on the configuration and plasma current and on whether the plasma is in L-mode or in H-mode. The values of λ_{sol} given in this paper are chosen in order to fit the calculated R_c, using the above formulas, to the measured reflection coefficient. Fig. 2 shows the dependence of the reflection coefficient on the launcher-plasma distance, for 3 different series of experiments.

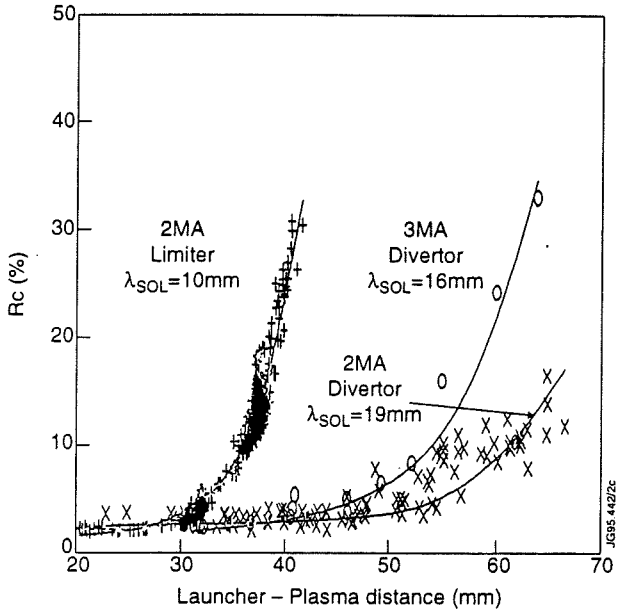

Fig. 2 Reflection coefficient versus plasma-launcher distance. + : 2MA Limiter Plasmas. : 3MA single null X-point plasmas. : 2MA single null x-point plasmas. The full lines are computed from (1)-(2), with = λ_{sol} =10mm, 16mm and 19mm respectively. All data are for L-mode.

All the points in Fig. 2 refer to the upper row of multi-junctions in the antenna. The observed reflection for all 3 series agrees well with (1)-(2), using c = 1% corresponding to a 1mm vacuum layer in front of the launcher. The variation in λ_{sol} is in qualitative agreement with the following very simple estimate :

$$\lambda_{sol} = (2D_{\perp} \cdot \frac{L_c}{C_s})^{\frac{1}{2}} \qquad (3)$$

where L_c is the connection length, $D_{\perp}$ the cross-field diffusion coefficient and C_S the speed of sound in the SOL [6]. The larger value of λ_{sol} for the divertor plasmas as compared to the limiter plasmas is caused by the difference in L_C for the 2 cases. The difference between the 3MA and 2MA plasmas on the other hand is caused by the increase in $D_{\perp}$ with decreasing plasma current. When the same comparison is carried out for the other rows of multijunctions in the antenna different values of c have to be used, corresponding to vacuum layer thicknesses between 1mm and 2 mm. The need to introduce a vacuum layer in the computations in order to achieve good agreement with the experimental results, can probably be explained by the existence of secondary limiting surfaces, behind which the density decay length is far steeper than λ_{sol}. The picture frame limiter, surrounding the launcher and protruding a few mm in front of it, is a good candidate. A slight variation in the alignment of this picture frame could explain the variation in vacuum layer thickness along the grill.

H-mode

The H-mode in JET is in general characterised by a succession of ELM-free and ELMy phases, with the period between ELMs varying from a few milliseconds up to seconds. LH-power has been coupled into a wide range of such plasmas, although H-modes with LH alone have not been observed. Fig. 3 shows the measured and calculated reflection coefficient for one such shot.

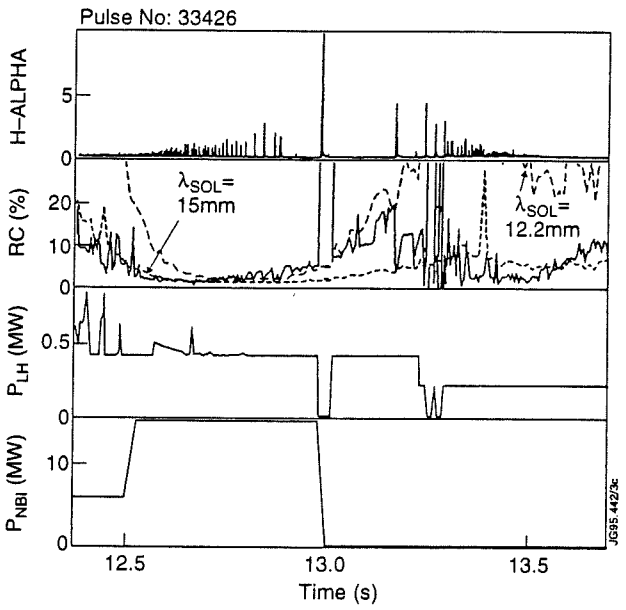

Fig. 3: LH-coupling into a long ELM-free period. 1: H . 2: LH-reflection coefficient, measured (full line), calculated assuming λ_{sol}= 15mm and 12.2mm respectively(dashed lines). 3: LH-power. 4:NBI-Power.

A 250 ms ELM-free phase starts when the NBI power is switched off. This period is terminated by an ELM, after which a series of ELMs occur at higher and higher frequency until the plasma has returned fully to the L-mode. The reflection coefficient follows the λ_{sol}=12.2 mm calculation very well during the long ELM-free period. When ELMs occur the reflection drops down to the level

corresponding to λ_{sol}=15 mm. The large ELM, terminating the longest ELM-free period, results in a decrease in reflection from 20% to less than 5%. During the following shorter ELM free periods the reflection does not increase fully up to the λ_{sol}=12.2 mm calculation.

During JET radiative divertor experiments the ELM frequency is very high (Grassy ELMs). The ELMs are clearly visible on the LH reflection coefficient. The reflection coefficient decreases to very low values of the order of 0.2%. In this case agreement with (1)-(2) is obtained by assuming that λ_{sol}=19mm and that no vacuum layer exists in front of the launcher. In almost all other cases the assumption of a vacuum gap is necessary to explain the data. A possible explanation is that, in this case large numbers of particles are ejected from the plasma during the ELMs resulting in high plasma density even behind the secondary limiting surfaces.

In summary: 1: During ELM-free H-modes the density decay length decreases by several mm (3mm for the case shown). This can cause the reflection coefficient to increase sharply. 2: As long as the plasma-antenna distance is kept sufficiently small good coupling can be achieved during ELM-free H-modes. 3: The expulsion of particles during an ELM increases the density strongly at the LH-antenna, reducing the reflection substantially. 4: During "grassy " very high frequency ELMs, which is an ITER relevant situation, exceptionally good coupling is achieved. Thus coupling of LH-power to H-modes is clearly possible, the main problem being the very fast variation in density at the antenna associated with ELMs. It has to be noted that breakdowns start appearing at the front of the antenna causing large impurity influxes into the plasma when high power is injected while the density at the antenna is large enough to achieve R_c<2%.

Gas Injection

In an attempt to improve the LH-coupling by injecting gas close to the LH-antenna, a special gas introduction pipe was installed 0.5m from the antenna. From this pipe it is possible to inject gas along the complete vertical extent of the antenna. To asses the improvement in coupling achieved using this LH gas pipe, the following experiment is carried out: In a pair of shots, gas is injected from the LH gas pipe in the first shot, and from a gas injection module, situated in the divertor region toroidally opposite the LH-launcher in the second shot. The gas flows and the central line average densities for the 2 shots are equal. The experiment is repeated for different antenna-plasma distances, for different LH power levels, and for different amounts of injected gas. No significant difference between the reflections in the 2 cases can be observed in any of the comparisons. On the other hand a clear improvement in the coupling is seen when the amount of injected gas is increased, independently of which injection module is used. The decrease in reflection coefficient when the gas flow is doubled corresponds to an increase in λ_{sol} from 11 mm to 14 mm.

Power Handling

Fig. 4. shows the coupled power from one klystron for all shots where this klystron is operated as a function of the reflection coefficient. It is seen that the maximum power which can be achieved depends critically on the reflection coefficient. Power above 400 kW can only be achieved for reflection coefficients below 3%, corresponding to a reflection at the front of the grill below 17%. The achievable power is clearly limited by the maximum field in the waveguides, with the limit being ~500V/mm [7].

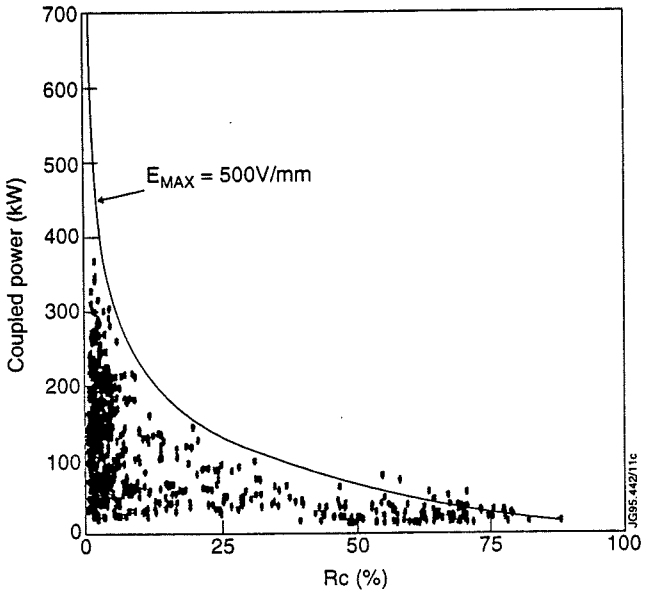

Fig. 4: Power handling versus reflection coefficient. The curve corresponds to a maximum electric field of 500V/mm.

Position Control

A low reflection coefficient is essential in order to achieve maximum power coupled to the plasma. On the other hand the density at the front of the antenna must not be too large since this induces breakdowns at the grill mouth, with large impurity influx into the plasma as a consequence. For coupling of more than 6MW to the plasma the reflection coefficient has to be kept between 2% and 4%. During JET pulses the reflection coefficient is kept constant at the desired value, by controlling the position of the launcher with a feedback loop. The non-linear reflection versus position curve (Fig. 2.), results in a loop gain in the feedback loop which is dependent upon the requested coupling. This in turn makes the loop unstable when too large reflection is requested, while the response becomes very slow when low reflection is requested. For the next campaign a more sophisticated controller will be employed in which the coupling curve is linearized, making the loop gain independent of the requested reflection. Fig. 5 shows how the feedback system has been instrumental in obtaining the highest coupled power achieved at JET till date.

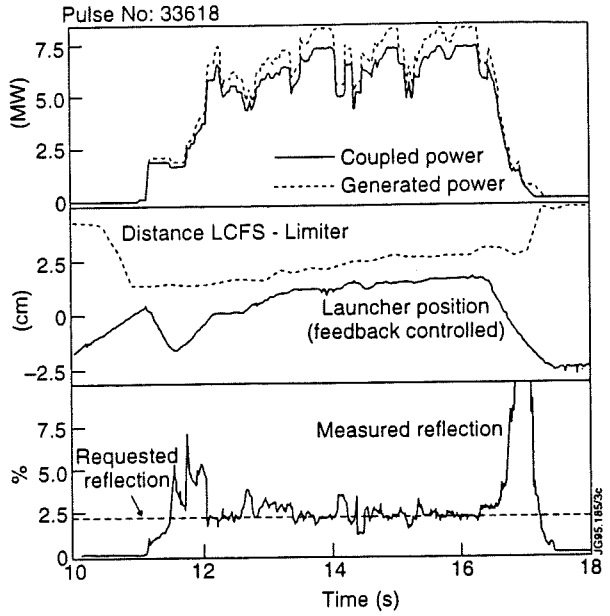

Fig. 5: 7.3 MW coupled power, with 8.2 MW Generator power.

Fig. 6 shows the feedback being used to keep the reflection constant for more than 5 seconds during an ELMy H-mode. The system reacts to the ELMs by retracting the launcher immediately when an ELM occurs and then moving it slowly forward as the H-mode develops. The power level is kept relatively low, to avoid breakdowns induced by the ELMs appearing before the launcher position system can react. Electronic systems aimed at overcoming this problem are under development.

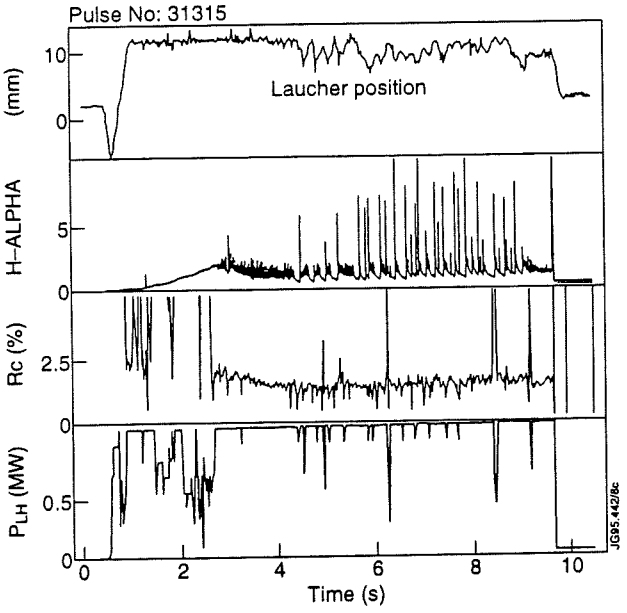

Fig. 6: Launcher moving under feedback control. 1: Launcher Position 2: H signal showing H-modes and ELMs. 3: Reflection coefficient.

REAL TIME POWER CONTROL

A new system has been implemented at JET to control the power from NBI, ICRH and LH in real time, using measurements from certain diagnostics as control quantities. Controlling the injected powers in this way is essential for JET and ITER type machines. This system has been tested for LH, attempting to control the surface loop voltage of the plasma. Fig. 7. shows such an experiment, where a loop-voltage of 0.075 V is requested. The loop is seen to be somewhat underdamped, with the loop-voltage oscillating around the requested value.

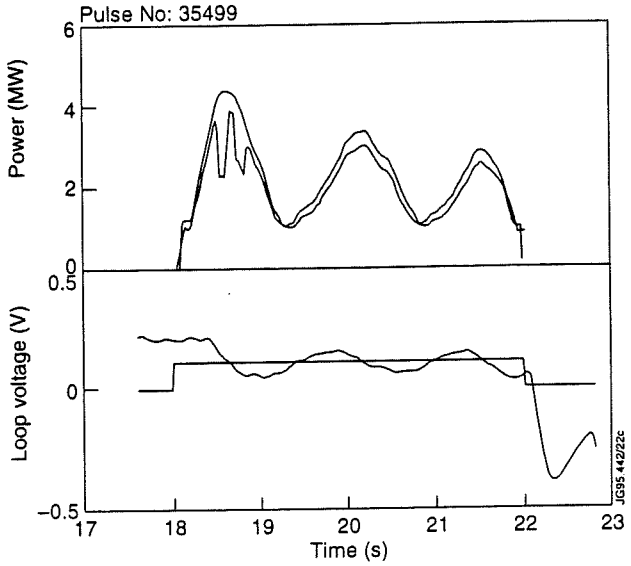

Fig. 7. Feedback control of the loop voltage. Top. Demanded and delivered LH-Power. Bottom: Requested and achieved loop voltage.

CONCLUSIONS.

In JET a maximum LH power of 7.3MW has been coupled to the plasma. This has been achieved by improving the conditioning state of the launcher, through electrical and RF baking and use of the dedicated cryopump, and by optimising the coupling of the LH waves to the plasma, by moving the LH-launcher under feedback control. The LH-coupling is seen to be in good agreement with the predictions of the SWAN code provided a vacuum layer of 1-2mm in front of the antenna is introduced in the computations. Coupling to both ELMy and ELM-free H-modes is feasible, although the large increase of density in front of the antenna associated with ELMs can cause problems at high power levels. Using a local gas introduction pipe near the LH-launcher has not shown any significant improvement in the coupling, as compared to using a remote gas introduction module, although the introduction of gas from either module is seen to improve the coupling significantly. The LH power can be varied in real time under feedback. This capability has been used preliminarily to control the plasma surface loop voltage.

References.
[1]F.G.Rimini et.al: 11th topical conference on RF power in plasmas, Palm Springs (1995)
[2]M.Pain et.al: 13th SOFE, Knoxville, (1989)
[3]F.X.Söldner et.al: IAEA meeting on RF launcher, Naka, (1993)
[4]C.Walker et.al: 17th SOFT, Rome, (1992)
[5]X.Litaudon, D.Moreau: Nuclear Fusion, Vol 30, no 7, (1990)
[6]P.C.Stangeby. Nuclear Fusion, Vol.30, No.7 (1990)
[7]A.Kaye et.al: EPS Topical Conference on Radiofrequency Heating and Current Drive of Fusion Devices, Bruxelles, (1992)

An In-Vessel Inspection System for the Next Step Fusion Machines

T V Businaro, L Consano
JET Joint Undertaking, Abingdon, OX14 3EA, UK

ABSTRACT

An In-Vessel Inspection Systems (IVIS) which uses linear arrays of optical fibres, is proposed for ITER. The system is based on long rotating line scanning viewing probes, which provide a quasi-spherical field of view and high resolution picture of 480,000,000 pixels completing the inspection in a few minutes, without the need for mechanical adjustments of the focus and the aperture of their lens optical systems. The illumination is provided by pulsed laser beams. The duplication of the optics in each probe has also been considered for tridimensional distance measurements.

INTRODUCTION

Frequent inspections of the interior of the ITER Tokamak vacuum vessel will be required not only to check for damage caused by plasma operations and to plan maintenance interventions, but also to increase confidence in the operation, particularly during its initial phase.
The time required to inspect several hundred square meters of ITER in-vessel surfaces using traditional methods (i.e. real time viewing) could become unacceptably long given the effects of the radiation dose on the viewing probe components. Since there are no moving parts inside the vessel, the use of 'non real time' image techniques, and in particular line scanning, has been investigated. As a result an in-vessel inspection system (IVIS) for ITER, based on line scan viewing probes is presented. This seems to offer advantages in terms of simplicity, picture resolution and inspection time.

1. SYSTEM LAYOUT

The proposed IVIS is made up of 4 identical units each of which includes a long viewing probe and its insertion guide (see Fig.1). The units are installed on top of the machine 90° apart. The probes are inserted into the vessel through the main vertical ports using long bellows as vacuum barrier and 'key-lock' mechanisms, which operate as neutron shields during plasma operation.
Each probe is connected to the insertion guide by a remote handling vacuum flange, so as to be easily removable for maintenance and upgrading. An alignment mechanism is installed in each viewing unit to comply with the vessel movement and to allow precise insertion of the probe through the port.

Two vacuum valves are used for connecting the insertion guide bellows to the key-lock mechanism. One is part of the 'key-lock', the second is part of the IVIS assembly to be used during the system maintenance and provides double protection of the primary vacuum during the plasma operation.

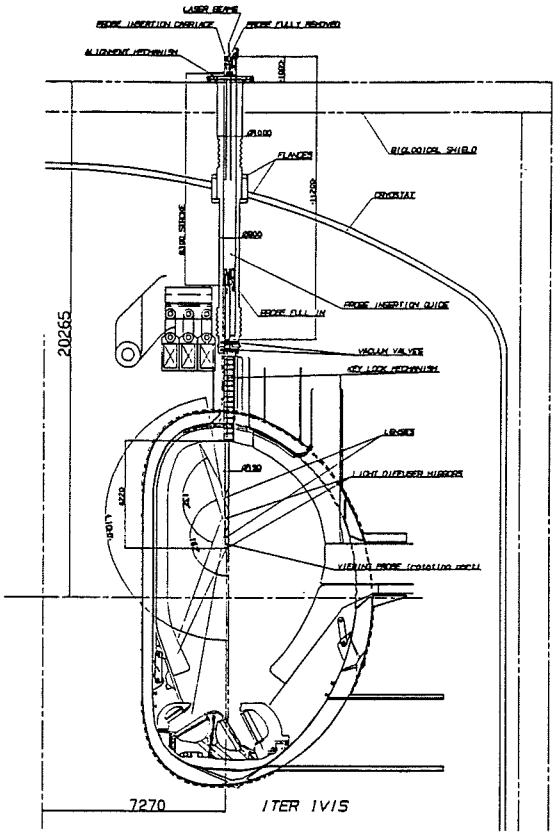

Fig.1

2. WORKING PRINCIPLE

A schematic optical layout of the proposed viewing probes is shown in Fig. 2a. A set of 16 small field of view (12°) lenses are positioned in a plane containing the axis of the probe, in such a way that their fields of view overlay by 1° on both sides (see Fig. 2b). As a result the lenses cover a viewing slot of 12° x 162° (16 x 10° +2°). Up to 10 linear arrays of 1024 coherent optical fibres are positioned in front of each lens vertically, one next to the other, at different distances so that there is always one image line in focus during the rotation (Fig. 2c).

Each linear array is an approx. 11m long flexible ribbon with a cross section of approx. 0.1 x 10 mm, in the middle of which lie the 1024 fibres, made with a synthetic silica (SiO_2) core of Ø <8μm and spaced 10μm apart, embedded in a fluorine doped cladding (SiO_2F) which also forms the array structure (see Fig. 2.d).

Maximum 160 linear arrays are required for 16 lenses, for a total of 160.000 optical fibres.

At the other end the linear arrays are packed together and directly coupled to CCD camera chips with 1024 x 1024 pixels of same size (10μm) in order to optimise the matching between each pixel and each individual fibre and to obtain the best possible picture resolution (see Fig. 2e).

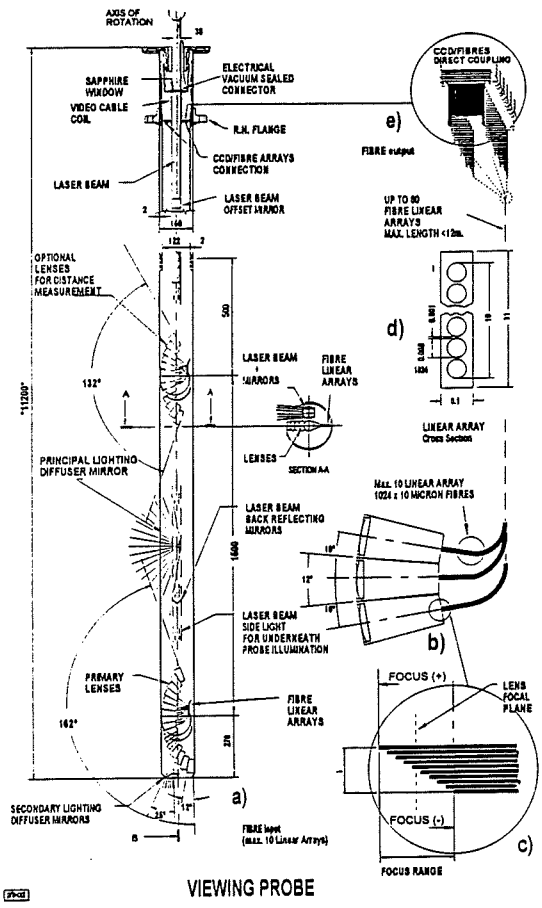

Fig.2

Given the dimension of the linear arrays, it is possible to pack together up to 100 arrays in front of the CCD bi-dimensional face plate so that the entire acquisition of all image lines should require only two CCD cameras.

Low divergence parallel 100 Hz pulsed laser beams are sent through the probe to pseudo cylindrical mirrors which diffuse the light in a fan shaped area illuminating only the viewing slot of the probe (see Fig 3). A constant low speed rotation (6minute/turn) of the probe around its vertical axis allows the lenses to scan a quasi spherical scene (160° x 360°) in one turn. During this rotation, at each laser pulse, the information relative to 10 x 16 image lines of 12° angle of view is collected by CCD cameras and sent to an image processor for storage and treatment.

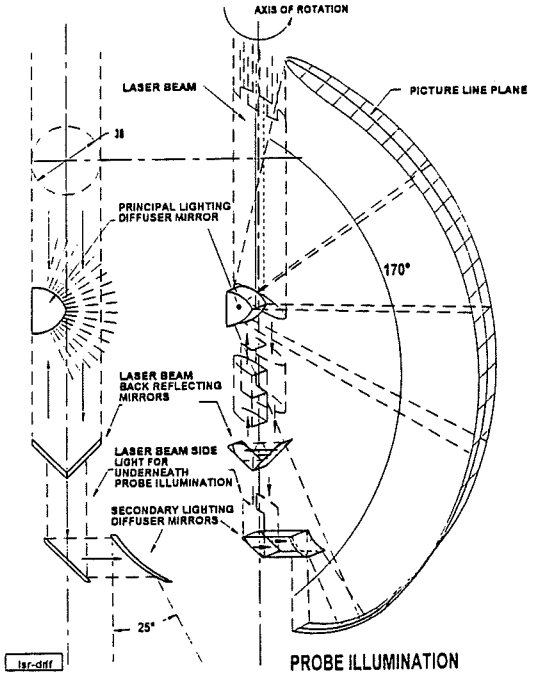

Fig. 3

A schematic functional diagram of the picture acquisition and image treatment is shown in Fig. 4. Once every 10 msec the output picture frames of two CCD cameras are grabbed inside the image processor. Because of the rigid coupling of the cameras and the fibre linear array output, the 160 image line information content will always be coherently stored in very well defined addresses of the frame grabber memories. After each grabbing cycle the image processor extracts this image line information from the frame grabbers and sends them in an organised manner to the image memory.

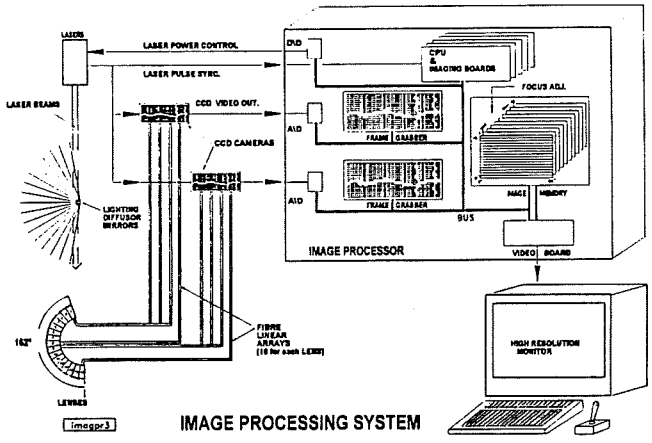

Fig.4

At the end of one turn of the probe, the image memory will contain 16 pictures of 12° x 360° field of view (for a total of 480 million pixels resolution) repeated up to 10 times with a different focusing.

The picture resolution is determined by the number of fibres per angle of view (approx. 83/°) and by the number of laser pulses during the 360° rotation time of the probe (83 pulses/°). This corresponds to a spatial resolution of approx. 2.5 mm at 10 m distance.

FIG.5

The picture analysis is carried out off line after the inspection is completed. The image processor will allow the operator to navigate inside the image memory to choose the best focused picture for each selected part of the vessel he needs to investigate.

Using real time analysis of all the line images at each laser pulse, it is also possible to control the light intensity. In fact, because of the physical dimension of the 10 fibre linear arrays, the line images cover a viewing slot of approx. 12° x 0.8°, and on average they will contain advance information about the level of light which will be reflected during the subsequent positions of the probe, so that optimal illumination control can be achieved, thereby regulating the power output of the laser beams at each pulse.

An optional set of lenses is also proposed for three-dimensional viewing which permits distance measurements. The rigid geometry of the optics setting and the possibility of using advanced functions of image processing make it possible to add this useful function to the more specific purpose of the inspection.

A simple experiment has been carried out to create a picture with the same line scanning technique proposed. The result, shown in fig. 5, represents a 270° x 60° view of the JET vessel mock-up , achieved by grabbing the central line of the TV frames of a rotating CCD camera with fixed focus and iris. The picture resolution is approx.6,000,000 pixels.

3. Main mechanical features of the system

a) Viewing probe

The viewing probe is an ≈11 m long 150 mm diameter flanged tube.

Its main mechanical feature is a vacuum tight straight rotary feedthrough (harmonic drive gear device) which facilitates the assembly of all components and the penetration (through a sapphire window) of the laser beams (see fig. 6).

Its working principle, reported in the technical literature, allows a high gear ratio and a constant slow motion which suit the viewing probe requirements.

The rotary part of the probe is all in vacuum and is supported and guided inside a protective tube by ball bearings. It contains the optical system (described in the previous paragraph) and the CCD cameras. Lead disks, of an average thickness of 200 mm, shield these sensitive devices from γ radiation during the inspection (estimated attenuation: $\approx 10^5$). Otherwise the camera parking position is above the machine neutron biological shield.

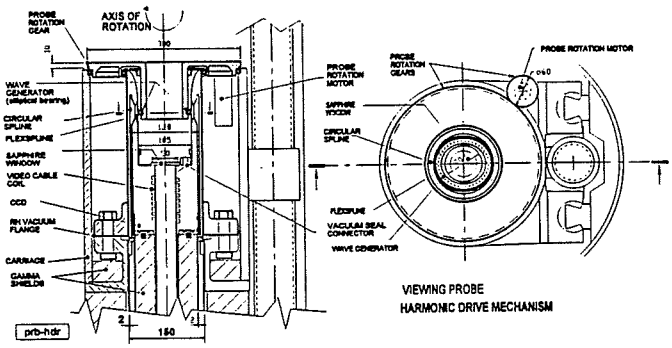

Fig. 6

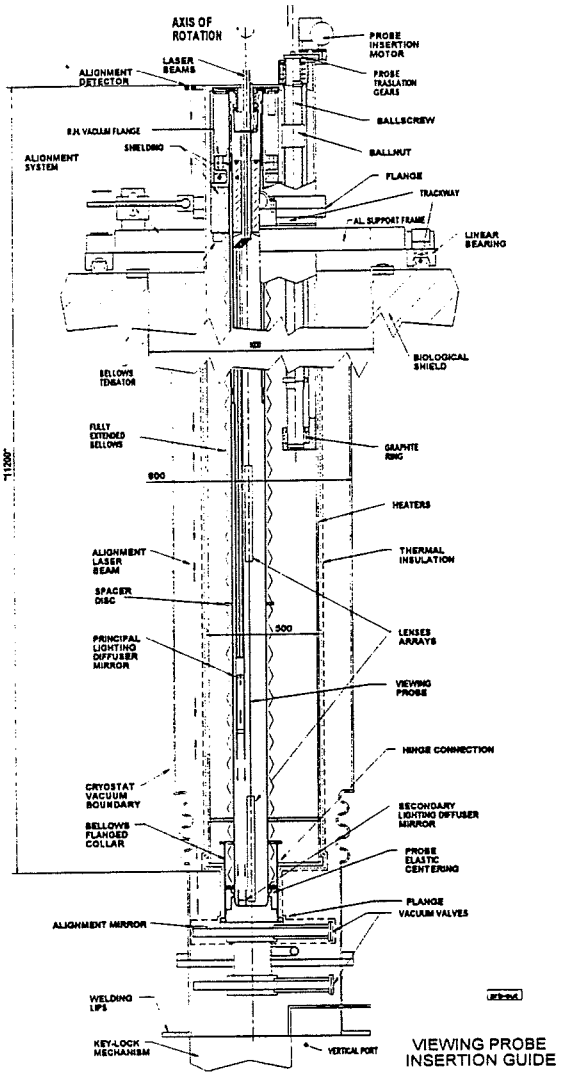

Fig 7

b)Insertion guide

The insertion guide is a ≈ 11m long, 500 mm diameter rigid stainless steel tube operating inside a second larger tube (Ø ≈1 m), which isolates IVIS from the cryostat vacuum.
The mechanical layout of the insertion guide is detailed in Fig. 7; its functional design is similar to that of the JET IVIS [1]. The insertion of the viewing probe is carried out by a vertical carriage sliding on two trackways driven by a long ball screw mechanism. The top of the guide is suspended with a gimbal arrangement from the alignment mechanism, installed across the biological shield penetration and is centred, at its bottom end, with the top of the port using a hinge connection. Combining the effect of the hinge connection with the movement of the alignment mechanism it is possible to adjust misalignments of approx. ± 1°.
A long lip welded bellows connects the RH vacuum flange installed on the vertical carriage to the hinge flanged collar. The bellows, made up of 8 sections with a 5:1 compression ratio, act as the vacuum barrier during the insertion of the probe in the vessel.

c) 'Key-lock' mechanism

A 'key-lock' mechanism is proposed as an easy and quick method to open a penetration channel for the insertion of the probe into the vessel and to shield it from the direct stream of neutrons during the plasma operation. The device is installed inside the vertical port, and its working principle is schematically represented in Fig. 8.

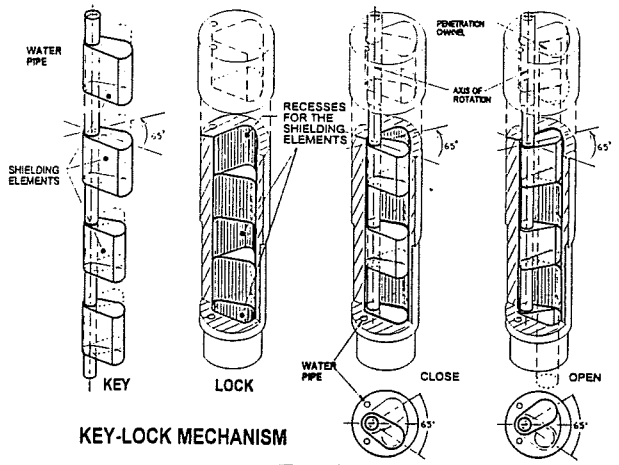

Fig. 8

The penetration channel is opened and closed by rotating the key by approx. 65° with a hydraulically driven mechanism. The system, when closed, ensures a minimum axial shielding factor of half its length. The transversal dimension of the key teeth is gradually increased in order to eliminate axial slits. As it is exposed to the plasma, the mechanism should be considered part of the blanket and should be designed and cooled according to the same specifications.

3. CONCLUSIONS

The feasibility of the system has been the main concern of this study. In particular the critical issue of the hostile ITER radiation environment has been tackled in four different directions:
- choosing suitable radiation resistant components
- providing shielding where possible and placing the most sensitive components (viz.: the CCD cameras) as far away as possible from the neutron radiation field
- to allow the baking of the entire probe optics to facilitate the recovery of the optics glasses affected by radiation
- designing the viewing probe, so that, if necessary, it can be easily removed by remote handling techniques.

The availability of such critical components as the fibre linear array has been investigated. At present SiO_2/SiO_2F linear arrays of up to 400 fibres can be found on the market, while the manufacturing process of the arrays of 1000 fibres is being experimented.
Calculations of the illumination level have been carried out based on the use of an existing laser Nd:Yag able to provide up to 100Hz pulses of 0.2 J in the visible (532 nm) or double the energy in the infrared (1064nm). The results show a significant average illumination at 10 m distance and with 532nm light of approx 4.5 W/m^2 (≈3000 lumen/m^2) using 4 laser units and considering 60% of efficiency.
Particular attention has also been paid in designing a system which should be able to be upgraded with the latest technologies. In fact the design of a complex system which will not be operational for several years, needs to take account of future developments in the different technological areas involved, so as not to produce something which could be become obsolete before it is in use. This is especially applicable to such areas as laser technology, image sensing and image processing.
Finally extensive experimental work is needed to complete in detail the feasibility analysis of the system.
The whole study of this IVIS proposal is reported in [2]

ACKNOWLEDGMENT

Important contributions are acknowledged from:
T Raimondi (JET) for his guidance and technical expertise, R B Huxford (optical design consultant) for the verification of the optics, G Benali and JF Junger (JET) for the realisation of the line scanning picture , H Panissie' (JET) for mechanical design

REFERENCES

[1] T Raimondi, R Cusack, L Galbiati
The JET In-Vessel Inspection System', 14th Symposium on Fusion Technology, Avignon, France 8-12th September 1986
[2] T V Businaro, L Consano
An In-Vessel Inspection System for ITER; JET Internal Report

Study of the Distribution System for the ITER Power Supplies Scheme

T. Bonicelli[1], I. Benfatto [2], D. Hrabal [3], M. Huart [1], A. Illescas [4], V. Macho[4], A. Roshal[2], G. Schlegel[3]

[1]JET Joint Undertaking, Abingdon, Oxon OX14 3EA, UK

[2]ITER JCT, 801-1 Mukouyama, Naka-Machi, Naka-Gun, Ibaraki-Ken, 311-01 Japan

[3]Siemens AG, Werner-von-Siemens Str., D-91052 Erlangen, Germany

[4]IBERTEF AIE, Magallanes 3, 28015 Madrid, Spain

ABSTRACT

The study analyses the distribution system for the ITER pulsed loads including HV switchyard, stepdown transformers, Intermediate Voltage (IV) switchyard, rectifier transformers and DC busbars. A comparative investigation amongst four different options for the IV system was carried out. Reactive power compensation and filtering requirements were defined in relation to the admissable voltage drops and distortion. A tentative layout for the complete system was also defined

INTRODUCTION

The pulsed loads of ITER (International Thermonuclear Experimental Reactor) will require an extensive power supply system capable of responding, during an ITER pulse lasting 2000 seconds, to a demand of active power varying from about -800MW to +400MW while the reactive power, in the absence of any compensation, can reach a peak value of approximately 800 MVAR (Fig. 1).

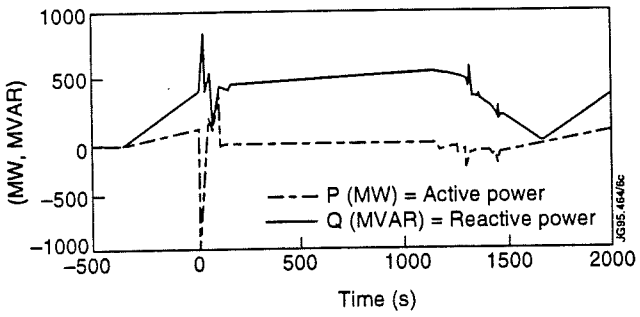

Fig. 1: Active and reactive power loading of the ITER pulsed loads

The experience gained in other large experiments [1] suggests that the supply of loads directly from the grid is, wherever the site conditions make it possible, the most convenient and cost effective solution. Ad hoc studies for the ITER case [2] show that the load can indeed be supplied in various European locations. The ITER pulsed loads are: seven superconductive poloidal field (PF) coils (P1 to P7), the set of twenty-four superconductive toroidal field (TF) coils and the additional heating (AH) loads. The total installed converter power is 3600 MVA [3]. The study (ITER Design Task 94/D51) was aimed at: identifying the schemes for the ITER pulsed supplies distribution system; defining the ratings of the main components and providing costs and delivery times.

The study was carried out taking into account the ITER design status described in [3] which was later substantially modified. An up-to-date description is in [4]. Standardised site conditions were also defined and agreed with the ITER Joint Central Team. The study involved several European manufacturers and included a wide survey of commercially available equipment.

AC DISTRIBUTION SYSTEM

The ITER pulsed loads were assumed to be supplied from an incoming HV grid double line via two circuit breakers X110 and X210 (Fig. 2). The assumed HV grid parameters, including the main limits to be complied with, are given in Table I.

Table I
Tentative HV Grid Main Parameters

Nominal voltage	380kV
Fault level	15-35 GVA
Frequency	50 Hz ±0.25Hz
Max. active pulsed power	1000 MW
Max. reactive power	500 MVAR
Max. allowed voltage harmonics (VMS)	1.5%
Max. allowed voltage variation	2.5%

Two HV busbar systems (BB1 and BB2) connect the two incoming circuits to four HV transformers (SGT1A, SGT1B, SGT2A and SGT2B). The two busbars can be connected together by means of the bus-coupler X013, in case one of the two incoming circuits is out of service.
The HV step-down transformers (400 MVA pulse power, 260 MVA continuous power) are provided with a tertiary winding (ca. 75 MVA) to reduce the zero-sequence impedance and with on-load tap-changers. The impedance voltage of 17.5% (400 MVA base) gives a fault level on the Intermediate Voltage (IV) busbars of 2.15 GVA and the three-phase short-circuit current, at 33kV, is 39.9kA, just within the capability of available vacuum circuit breakers. The primary star-point is solidly grounded; amongst the various methods of connection of the secondary star-point, eg. floating, low Ohmic, compensating (Petersen) coil and high Ohmic, the choice fell on the last option. This type of arrangement limits the fault current in case of single phase earth faults to a few tens of amperes and assures a good selectivity for the detection of earth faults even in

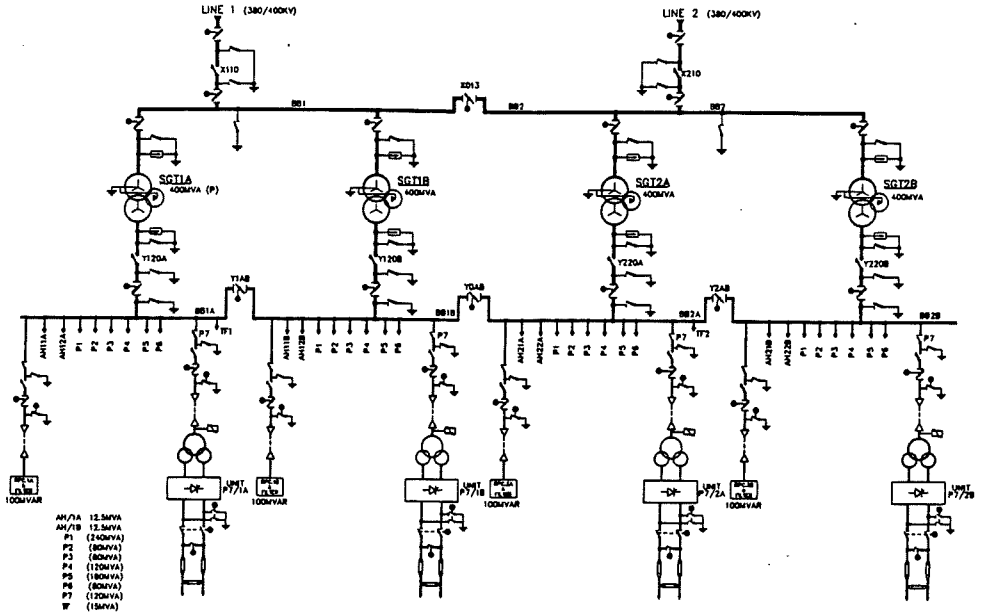

Fig. 2 Power Supply Scheme for the ITER Power Pulsed Loads

presence of imbalance of the system capacitances to earth. The supply can be maintained for up to 400s thus allowing an ordered termination of the ITER pulse.

The IV distribution system is based on four busbars (BB1A, BB1B, BB2A and BB2B), each of them normally fed from one HV transformer. Buscouplers (Y1AB, Y2AB and Y0AB) are available to connect the IV busbars in case one of the HV transformers is out of service. The loads are evenly distributed amongst the four busbars. Each PF power supply is composed of four units, series connected, one on each busbar. The units operate in sequential control with freewheeling action. The TF power supply is composed of two modules, series connected for redundancy. Two feeders on each busbar are dedicated to the AH loads (12.5 MVA each). A summary of the pulsed loads considered for the design is given in Table II.

Table II
Pulsed* loads on each IV busbar (MVA)

P1	P2	P3	P4	P5	P6	P7	TF**	AH
240	80	80	120	180	80	120	15	2x12.5

*Pulse factors: (ratio between pulsed and continuous power)
P1 to P7 = 1.5; TF = 1; AH = 2
**On busbars BB1A and BB2A only

Voltage drops during the execution of the ITER pulse (fig. 1) were calculated for a HV grid fault level of 15 GVA both in absence and with 400 MVAR of reactive power compensation (RPC). The most critical instants were found to be at t = 3s (plasma initiation) and t = 75s (X-point formation) (Table III).

Without RPC, the voltage drops on the HV grid exceeds by far the specified limits (Table I). On all the IV busbars, the voltage drop goes beyond 15% which was deemed to be the acceptable limit to ensure the proper functioning of the AC/DC converters. The situation improves when 400 MVAR of RPC are considered; though the voltage drops on the HV grid and BB1A are still not satisfactory, it would appear that additional 30 MVAR of RPC on each busbar would keep them within the desired limits. The

Table III
Voltage Drops on HV Grid and IV Busbars

	BB1A* (t=75s)	BB1B (t=3s)	BB2A (t=3s)	BB2B (t=3s)	HV grid (t=3s)
P(MW)	30	250	220	80	830
Q(MVAR)	305	230	230	150	820
V drop % (no RPC)	25.7	22	16.6	16.6	7.5
V drop % (with RPC)	16.8	11.4	6.2	6.2	3.6

*The voltage drop on BB1A is affected by the assumption that, when the required load voltage is low, all its AC/DC converters are still in operation (the AC/DC converters for the loads P2 to P7 on the other busbars being instead in freewheeling mode).

RPC system is sub-divided into four 100 MVAR units (one for each busbar) composed of two 50 MVAR modules. Two alternatives were considered: mechanically switched capacitors (point-on-wave switching of vacuum breakers) and static-var, the first one being less expensive but providing a more coarse and discontinuous compensation. For the 33kV scheme, the RPC units are directly connected to the IV busbars while, for the 66kV and 132kV schemes, a matching transformer is required. The voltage harmonic distortion, under some conservative assumptions and in the absence of filters and RPC, could reach (Table IV), at t=75s, 7.36% on the HV grid and 18.84% on BB1A. Filters are necessary to maintain the voltage harmonic distortion below 1.5% on the HV grid and below 5% on the IV busbars.

For each IV busbar, the filter arrangement is composed of two LC tuned branches (all the components values are

Table IV
Voltage harmonic distortion (%) on HV grid and IV busbars
(t=75s - X-point formation)

	No filters/ No RPC	With filters/ No RPC	With filters and RPC
HV grid	7.36	1.29	1.17
BB1A	18.84	3.10	2.70

given for the 66kV option) at 550 Hz (L=15.2 mH, C=5.5μF) and 650 Hz (L=16.4 mH, C=3.67μF). An additional high pass branch (L=32 mH, C=0.25μF, R=400Ω) is added to damp the high frequency oscillations generated by the resonance between the cable capacitance and the stepdown transformer reactance. The additional, filtering effect of the RPC units (L=4.74 mH, C=134μF for a 50 MVAR module) was also considered.

Four options for the IV distribution system were analysed and compared in detail (Table V):

a) 33kV indoor substation;
b) 66kV indoor Gas Insulated substation (GIS);
c) 66kV outdoor substation;
d) 132kV outdoor substation.

66kV appears to be the most convenient voltage level; the availability of components makes it preferable to the 33kV option, while cost (for the outdoor switchyard solution) and less difficulties for the construction of small rectifier transformers give it an advantage over the 132kV option. While the 66kV GIS alternative could be considered in case of particular site conditions, it is thought that the 66kV outdoor switchyard option is the most effective choice.

RECTIFIER TRANSFORMERS

The rectifier transformers are provided with two secondaries to supply 12-pulse AC/DC converters. Pulse factors were as in the note to Table II. Two main sizes were identified: 80 MVA (P2, P3 and P6 loads for a total of 12 units) and 60 MVA (P1, P4, P5 and P7 for a total of 44 units). Smaller transformers were in addition required for the AH, TF loads and for AC/DC converter boosters. For the smaller transformers and the higher primary voltages (66kV and 132kV), it was reported that the construction may be critical and that matching auto transformers in the same tanks were required. The impedance voltage for the main rectifier transformers was fixed at 12% (pulsed power basis). The connection between transformer secondaries and AC/DC converters is characterised by high currents and aluminium isolated phase busbars were adopted. The busbars account for an additional 3% impedance voltage.

DC SYSTEM

The DC system encompasses the DC busbars and limiting reactors at the output of the AC/DC converters, the main DC busbars connecting the power supplies to the Electrical Termination Building and all the associated switchgear. Each power supply is provided with a disconnector, an earthing switch and a by-pass switch (all motorised) to allow the unit to be isolated in case of faults. Each 12-pulse AC/DC converter is made up of two 6-pulse modules parallel connected; two air-cored water-cooled limiting reactors are required to reduce the 300 Hz circulating ripple current and the current imbalance, especially during transition to freewheeling mode and to limit the peak DC short-circuit current within 250kA. The design was standardised and two types of reactors were devised: the first one of 100μH for the PF power supplies and the second one of 10μH for the TF system. Each pole of the main DC busbars is constructed of four 500x30mm aluminium bars (Fig. 3) for a DC steady current of 50kA and a peak short-circuit current of 250kA. The busbars are cooled by natural circulation of air; the sections of busbars are welded.

LAYOUT AND DELIVERY TIME

For all the four options considered for the IV distribution system, a general layout was produced (Fig. 4), covering the HV switchyard and transformers, the IV distribution system including cable trenches, rectifier transformers bays and AC/DC converter buildings The layout includes enough space for additional feeders on each of the four busbars as well as bays for rectifier transformers for future

Table V
Comparison amongst the four options for the IV Distribution System

	33kV indoor	66kV GIS	66kV outdoor	132kV outdoor
Circuit Breaker Type	Vacuum	SF_6	SF_6	SF_6
Technical Feasibility	The 33kV scheme presents some difficulties: the rated current for the incomers (700 A) is beyond the capability of available circuit breakers and non-standard arrangements (eg. the use of one three-pole circuit breaker per phase) must be adopted. For the feeders a cabinet including the circuit breaker and two isolators should be developed. The other three options can be implemented with standard equipment. The higher voltages (66kV and 132kV) might entail some problems with the smaller rectifier transformers.			
Reliability	An assessment of the reliability was possible only in general terms in view of the particular operating regimes which are unlike standard applications. The number of connections for the 33kV scheme is about twice than for the 66kV and 132kV options, with consequently higher risk of failure.			
Maintainability	Indoor substations should result in less demanding maintenance requirements (easier access, no external insulators). Maintenance of GIS normally requires specialised teams from the Supplier with longer down-times. Vacuum breakers require less frequent maintenance than SF_6 breakers			
Performances	Performances are equivalent to a great extent. The 33kV option entails higher faults current with higher energy released. Switching overvoltages are in general higher for vacuum breakers than for SF_6 breakers			
Area required (m^2)	2450	2400	13760	23460
Cost IV switchyard only	1.18	2.13	1	1.44
Cost (AC syst. incl Rect. Tx)	0.96	1.19	1	1.18

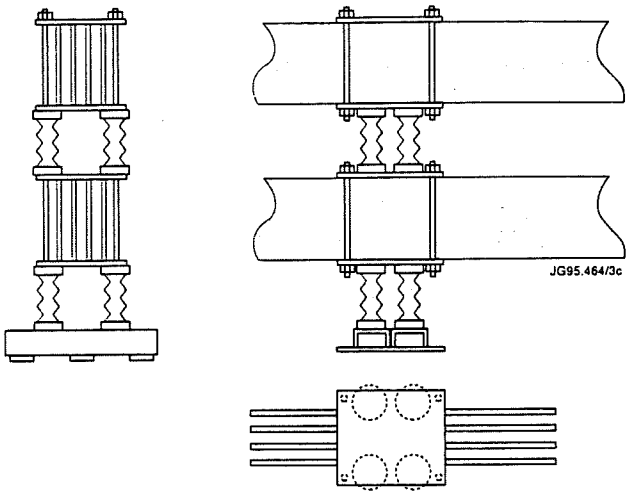

Fig. 3 Arrangement of the main DC busbar

loads and an area for the installation of further four 100 MVAR RPC units. The items with the longest delivery times are the rectifier transformers and the DC busbars (36 months) partly due to the large number of pieces.

CONCLUSIONS

The AC distribution system for the ITER pulsed loads does not require, with the exception of the 33kV option, any non-standard components. The study produced a large amount of data on the components and equipment including ratings, cost, sizes, delivery times which can be utilised as a data base for the investigation of new power supplies schemes. Outline specifications were produced which can be used as a basis for the procurement contracts. Some areas of further investigation were also identified. The reliability issue might require some additional scrutiny. The layout of the DC busbars system will also require an additional effort, especially for the study of the routing in the Switching Hall. A possible design for the DC busbar connections has been established though it should possibly be reviewed taking into account the later modifications at the coil connection circuits.

ACKNOWLEDGEMENTS

The authors would like to thank the various Manufacturers who contributed to the study by providing indispensable information and data on the equipment.

REFERENCES

[1] E. Bertolini et al, "Supplying JET from the UK 400kV Supergrid: A major engineering achievement relevant to the next step, *Proceedings of the 16th Symposium on Fusion Technology, London (UK)*, 3-7 September 1990

[2] E. Bertolini et al, "Assessment of the suitability of the European 400kV grid to supply the ITER load", *to be presented at 16th SOFE*, 30 Sept - 5 Oct 1995

[3] P.L. Mondino et al, "The ITER Poloidal Field System: Control and Power Supplies", *Proceedings of the 18th Symposium on Fusion Technology, Karlsruhe (Germany)*, 22-26 August 1994

[4] A. Roshal et al, "ITER Coil Power Supply", *to be presented at 16th SOFE, 30 Sept-5 Oct 1995*

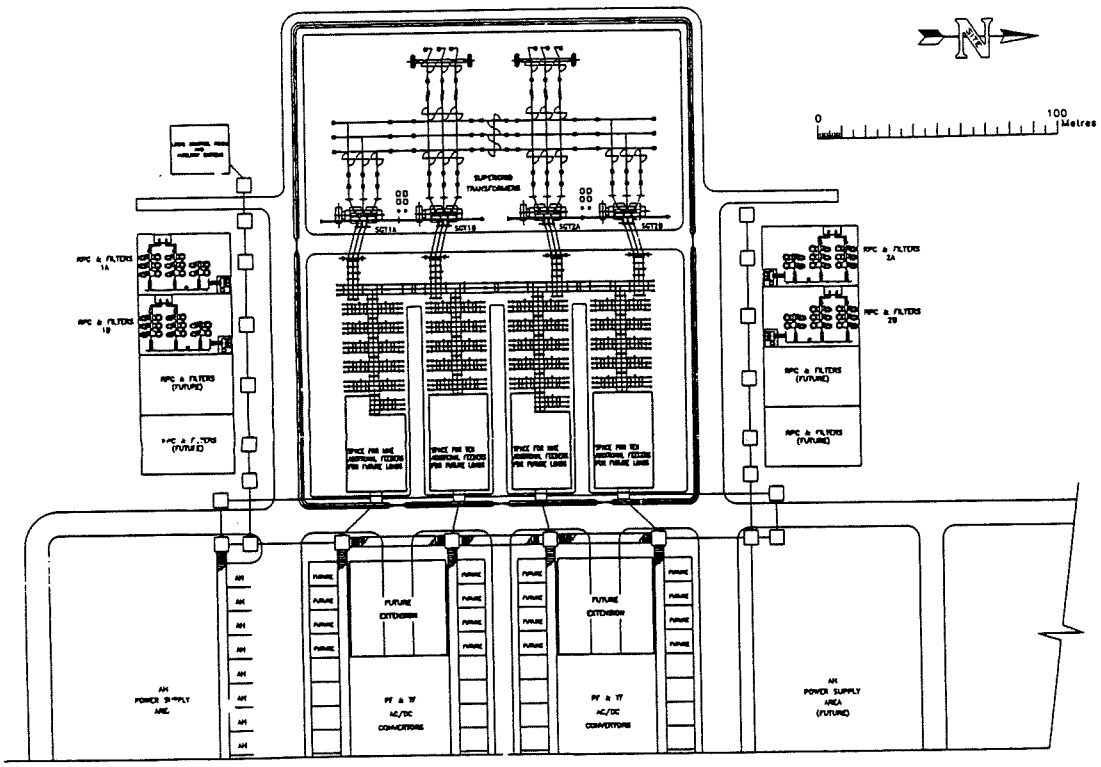

Fig. 4 General layout for the ITER Pulsed Power Supplies Distribution System (66kV outdoor IV substation)

The JET Programme on the Development of Beryllium Clad Components for ITER

C. Ibbott, D. Ćirić, E. Deksnis, H. Falter, A. Peacock, M. Watson
JET Joint Undertaking, Abingdon, Oxon, OX14 3EA, United Kingdom

ABSTRACT

JET under a contract with the European Home Team and in co-operation with industry, is carrying out a programme to support development of beryllium (Be) divertor components for ITER. The basis for this programme is the existing experience on the brazing of thin (1.5 to 3mm) Be cladding to CuCrZr hypervapotrons using a silver based alloy (Incusil 'ABA), which demonstrated critical heat fluxes of up to 18 MW/m^2, and good low power high cycle performance. This paper reports on the mechanical strength of thick (5, 7.5 and 10mm) Be/CuCrZr braze samples showing the feasibility of brazing thick clads. Also reported are the results of testing of 10mm thick tiles brazed to a hypervapotron. These tests resulted in melting of the tile surface at power levels of 20MW/m^2 without complete delamination of the joint. The results of these tests have allowed the European Home Team and European ITER JCT to benchmark their one and two dimensional models. Another important aspect of the JET investigations is the development of a silver free braze which is being developed in collaboration with industry and producing interesting results with shear strengths almost comparable with Incusil ('ABA') with failure occurring in the braze/CuCrZr interface.

I. INTRODUCTION

The ITER Be divertor component concept [1] is based on a thick Be Cladding (typically 10mm), brazed to a CuCrZr heat sink, in which heat fluxes up to 5MW/m^2 are cooled in steady state, and higher, off-normal heat fluxes are sustained inertially. The thickness of the cladding is dictated by the expected erosion rate. Critical issues are the manufacturability of components to this concept, and the experimental determination of the lifetimes under high cycle low power and low cycle high power testing. In addition, due of the high cross-section of silver for transmutation into cadmium under neutron irradiation, the ITER braze should contain no silver.

JET has now extended the silver based braze technique to 10mm Be Cladding. A number of 27mm square, 10mm thick tiles were brazed to a hypervapotron. Testing has been performed up to a maximum power flux of 20MW/m^2 for 1.5 sec, which brings the Be surface above melting temperature. At this level, after 22 cycles, structural deformation of the Be and delamination of the joint is observed. The tile however remained attached. In addition, results of mechanical testing for two Be grades and various material thicknesses have been obtained and will be reported.

Work is under way to develop a silver free braze. Two joining techniques are being developed based mostly on Copper systems with starting temperatures not significantly exceeding those with Incusil 'ABA'. The moderate temperatures are important to retain the strength of the CuCrZr. The brazes are being qualified and compared with the silver based braze using shear testing, X-ray testing, mechanical testing of CuCrZr and finally heat load testing. Results are reported below.

JET is also contributing brazed samples of Be to CuCrZr for a neutron irradiation programme, due to start in 1995 under the auspices of the European Home Team.

II. MECHANICAL STRENGTH OF THICK Be BRAZE SAMPLES

Mechanical testing of thick (5, 7.5 and 10mm) BeS65C induction brazed to 6 mm CuCrZr with Incusil 'ABA' alloy using the previously reported optimum braze cycle [2],[3] has been performed.

Fig. 1 shows the average shear strength of the braze samples for each thickness at as a function of temperature up to 400°C. The effect of the residual stresses due to braze cool down can be clearly seen.

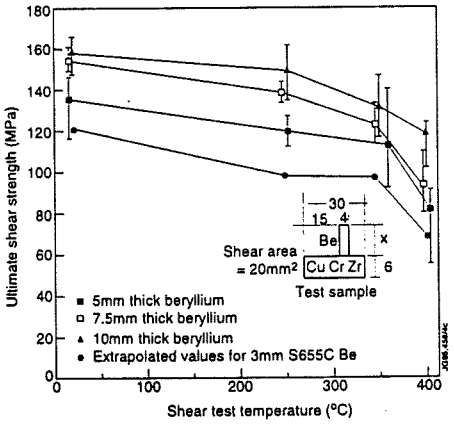

Fig. 1 Shear strength of 5, 7.5 and 10mm thick BeS65C brazed to CuCrZr

Fig. 2 shows the shear strength comparison of brazed 3mm BeS200FH and extrapolated values for 3mm BeS65C. Also plotted is the yield strength in shear of BeS200FH. Note that the yield strength of the solid BeS200FH follows closely the ultimate shear strength of the brazed BeS200FH samples.

By the consideration of materials data, it is clear that the ~26% increase in the ultimate shear strength of the brazed samples when changing from BeS65C to BeS200FH (120MPa to 163MPa at room temperature) is very similar to the difference (~30%) in yield stress of the two grades of

Be. The tensile yield strength of BeS200FH is 360MPa compared to 251MPa for BeS65C. It can be inferred from this that the high stiffness of the Be holds the joint intact until the yield stress of the Be adjacent to the braze is reached which then results in failure of the joint.

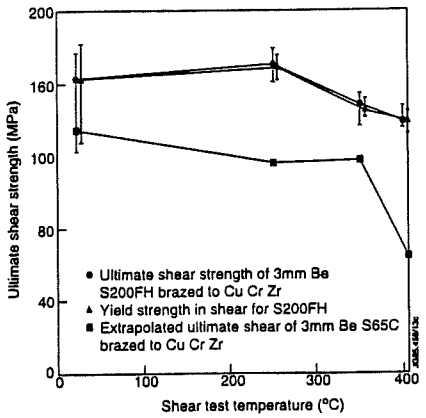

Fig. 2 Comparison of shear strength of brazed 3mm BeS200FH, 3mm BeS65C and yield strength of BeS200FH

This failure mechanism could be alleviated by the inclusion of a compliant layer, improved edge geometry and castellation design.

III. 10mm Be Clad Hypervapotron High Heat Flux Tests

A hypervapotron [10] was clad with 10mm thick, 27mm Square uncastellated BeS65C tiles. They were brazed using Incusil 'ABA' and the standard braze cycle [2], [3]. The hypervapotron was installed in the JET Neutral Beam Be test facility and subjected to high power beam pulses derived from a JET Positive Ion Neutral Injector (PINI). Detailed results and discussions can be found in [4]. Fig. 3 shows the test set-up, with the diagnostics used. These were:-.

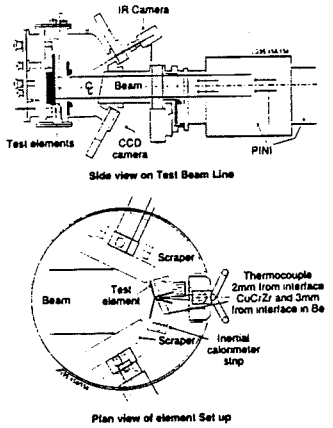

Fig. 3 Schematic of High Heat flux test set-up

- IR imaging system with either in frame repetition rate of 30 Hz or in line mode repetition rate of 2.5 KHz.
- Water calorimetry
- OFHC copper inertial calorimeter measuring average applied power
- CCD camera
- Thermocouples 2mm from the interface in the CuCrZr and the Be.

The test was divided into three stages.

1. 100 pulses of low power density (5-6MW/m^2) to confirm the integrity of the braze and predicted surface temperatures.

2. Several pulses of high power density (15 to 20MW/m^2) to establish surface melting temperature on the Be but not actually producing melting.

3. 22 pulses of 4.5MW/m^2 to equilibrium followed by 20MW/m^2 with gradually increasing duration to develop surface melting followed by several seconds of 7.5MW/m^2 to mimic the effect of vapour shielding.

The PINI output cannot be stepped as described in the 3rd stage so the results were achieved by setting the PINI parameters that yield a power density of 20MW/m^2 and then modulating this beam to give the required average power density. Fig. 4 shows a typical modulated pulse. Fig. 5 shows the exposure statistics for the whole test.

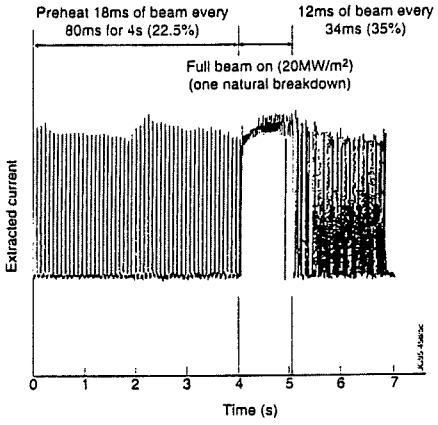

Fig. 4 Typical modulated pulse details

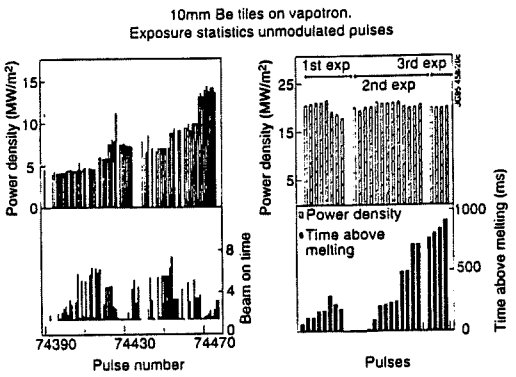

Fig. 5 Test exposure statistics

During the test, comparisons of calculated and measured surface temperatures showed that the IR camera gave erroneous measurements above temperatures of 1000°C. This is due to an irreversible change in emissivity of the Be when it reaches temperatures above 1000°C. The variation

in emissivity is from 0.3 to 0.8. Fig. 6 shows a contour plot of surface emissivity cross section with all tiles at equilibrium temperature of 470°C. (Note the definite transition line highlighting the area with changed emissivity.) After the test, the IR camera was calibrated by removing the cooling and slowly uniformly heating the hypervapotron. Comparisons of the measured temperature (thermocouples) and the emissivity then gives a emissivity correction curve.

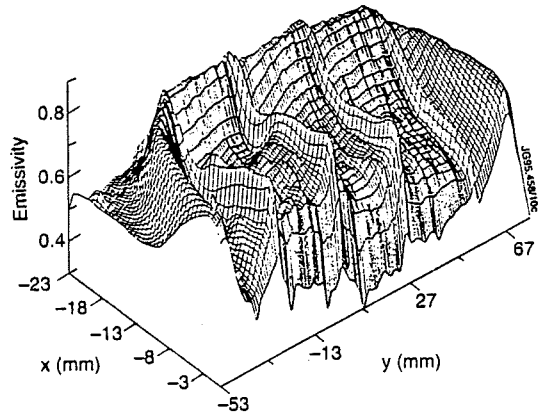

Fig. 6 Surface emissivity contour plot across tiles

The corrected surface temperatures and the measured Be I line emission are shown in Fig. 7. Also plotted, is the Be vapour pressure obtained from literature which agrees well with the measured results.

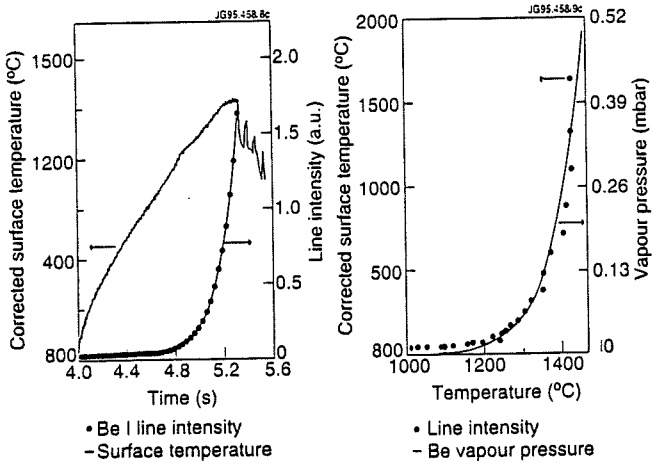

Fig. 7 Corrected surface temperatures of the Be tiles (10mm thick) clad to the hypervapotron during a pulse of 20MW/m^2, Be I line emission and vapour pressure

On completion of the third stage, the tile which had reached the highest temperature in the test was cut in half and sectioned to examine the melt depth. Three micro graph sections were taken to enable measurement of the average melt depth which is 0.53mm. The micrograph cross sections are shown in Fig. 8.

Note the cracks in the melt region that propagate down into the unmelted material. Cracks are observed in areas of the tile that did not show signs of surface melting.

Ultrasonic examination of the tiles that delamination of around 50% of the braze area has occurred but the tiles have remained attached to the hypervapotron.

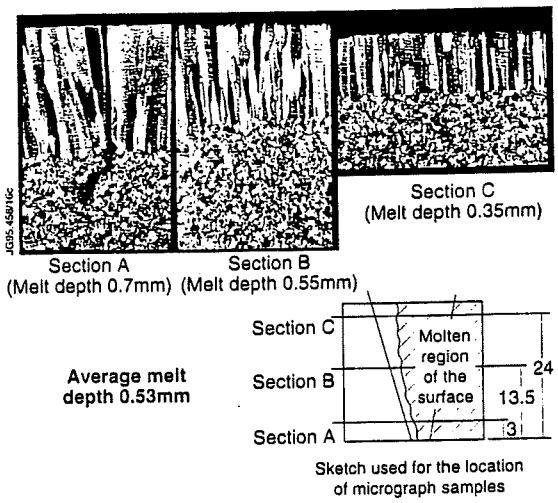

Fig. 8 Micrograph cross sections showing melt depth

IV. ONE AND TWO DIMENSIONAL FE MODEL COMPARISONS

One major benefit of this experiment is to benchmark FE codes to predict the melt depth and evaporation rate. For this work FE modelling is being carried out by members of the European Home Team and European ITER JCT.[5] [6].

Figs. 9 and 10 show the results of modelling with various power settings compared with the measured data. The sensitivity of the melting and re-solidification in the model to the power setting is clearly seen.

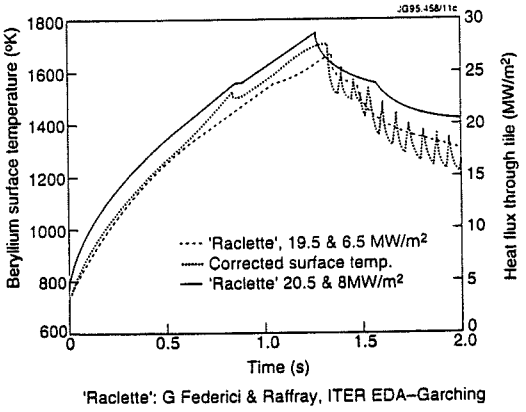

Fig. 9 One dimensional ITER 'RACLETTE' [5] model fits to measured data

V. SILVER FREE BRAZE DEVELOPMENT

Silver has been identified as a potentially damaging element in ITER because of its transmutation to cadmium, which having a high vapour pressure at the ITER operating temperatures would lead to fears of vacuum vessel, and hence plasma, contamination. Within the European Home Team contribution to the ITER task T1, part of the development of Be brazing activity has been to investigate Silver free alternatives to the successful InCuSil 'ABA'

braze. This development work, still in its early stages, has been based upon two joining methods identified by GEC-Marconi Materials Technology [8]. These methods are:-

- Vacuum Induction Brazing based upon a CuMnSnCe braze alloy
- Diffusion Soldering using copper and tin.

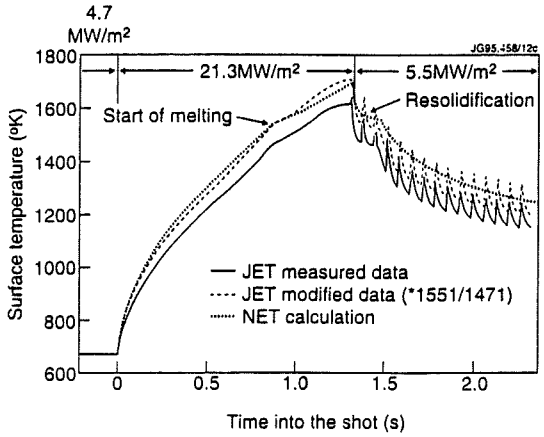

Fig. 10 Two dimensional NET model fit to measured data

In the work carried out in this development, 0.1mm thick foil of CuMnSnCe braze has been used to vacuum induction braze Be to CuCrZr under conditions similar to the InCuSil ABA braze mentioned previously.. Optical examination of the samples has shown good filling of the braze and good wetting of the Be. Scanning acoustic microscopy shows little detail in the assemblies. Metallography of the joints, Fig. 11 has revealed that the joints are well filled with no evidence of porosity associated with the evolution of gas during the brazing operation. The metallography also indicates the formation of an intermetallic layer between the Be and the braze similar to that seen for the Incusil 'ABA'. However, there does appear to be some damage between the braze and the CuCrZr. The reason for this damage is still being investigated. Shear test results on these brazed assemblies at room temperature have shown values of up to 75MPa, compared with values of 143MPa achieved using the same equipment for InCuSil 'ABA' brazed assemblies. However, the failure does appear to originate in the braze/CuCrZr interface. This holds out the prospect of an excellent braze for Be once the braze/CuCrZr interface problems have been overcome. This development was performed by J.H. Vincent, S.P. Sangha, D.R. Wallis and D.M. Jacobson at GEC Marconi, Hirst Division, Borehamwood, Herts, WD6 1RX, UK, under a contract to NET.

Diffusion soldering [9] is a hybrid of soldering and diffusion in which tin is used as a low temperature solder to produce a soldered joint, the tin then being allowed to diffuse in to the copper substrate to homogenise the joint which will consequently have a much higher remelt temperature. The technique relies upon bonding a copper layer onto Be and then joining the copper metallisation to the CuCrZr with the diffusion soldering technique. This technique (metallisation followed by diffusion soldering) produces excellent bonds between the copper layers and apparently seamless joints on Be/CuCrZr assemblies. Scanning Acoustic microscopy did not reveal any features in the joints. Strengths of up to 48 MPa were achieved in shear tests with failure occurring at the metallisation/Be interface. Further development of this solution relies upon improving the metallisation of the Be.

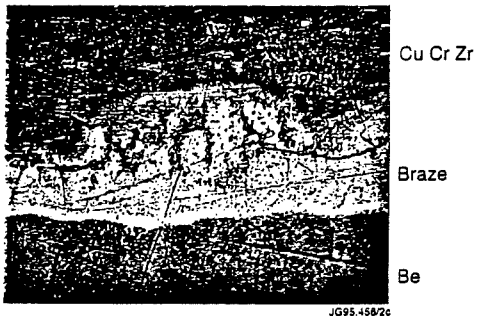

Cu Cr Zr brazed to Be using Cu Mu Sn Ce Braze x1000

Fig. 11 Micrograph section of CuMnSnCe brazed joint between BeS65C and CuCrZr

REFERENCES

[1] G. Janeschitz, et al, "The physics basis and design of the ITER divertor and of the pumping, fuelling System, *IAEA-CN-60*, Seville, Spain, Oct 1994.

[2] H. Altman, et al, "An analysis of induction brazed beryllium on Copper alloy substrates" *15th IEEE/NPSS Symposium on Fusion Engineering* Oct 11-15 1993; Hyannis, MA, USA.

[3] C. Ibbott, et al, "Further developments of brazing beryllium to CuCrZr" *18th Symposium on Fusion Technology (SOFT 18)* held in Karlsruhe 22-26 August 1994, also in JET P(94) 40 pp. 175-180.

[4] H.D. Falter, et al, "10mm thick Beryllium tiles brazed to a CuCrZr vapotron - Test Report", *Internal Report JET-C(94)* 128.

[5] G. Federici, A.R. Raffray, et al, "Analysis of heat transfer and erosion effects on ITER divertor plf's induced by slow high-power transients", *16th IEEE/NPSS, Symposium on Fusion Engineering*, Champaign, IL., Sept. 30/Oct 5, 1995.

[6] I. Smid, et al, "2D Finite Element Thermal Analyses of Plasma Excursions at 20MW/m^2, including Vapour Shielding, onto Be-, CFC- and W5 Re-Armoured ITER Divertor Plates", NET Internal Report N/I/3330/16/A.

[7] H.D. Falter, et al, "High Heat Flux exposure tests on 10 mm beryllium tiles brazed to an actively cooled vapotron made from CuCrZr." *Internal Report to be published.*

[8] The work of GEC-Marconi Materials Technology Ltd, Borehamwood Herts, WD6 1RX, UK is gratefully acknowledged.

[9] High Technology Joining, Sixth Int. Conf., British Association of Brazing and Soldering, Stratford upon Avon, UK 1991

[10] H Altman, et al, "A comparison between Hyper-vapotrons and Multitube High Heat Flux Beam Stapping Elements" IEEE 13th Symposium on Fusion Engineering, 2-6 Oct 1989, Knoxville,TN.